CERN, January 2007

RD50 Status Report 2006

Radiation hard semiconductor devices for very high luminosity colliders

Centro Nacional de Microelectrónica (IMB-CNM, CSIC), Barcelona, Spain
Pablo Balbuena, Francesca Campabadal, Sergio Díez, Manuel Lozano, Giulio Pellegrini, Joan Marc Rafí, Miguel Ullán

Dipartimento Interateneo di Fisica & INFN - Bari, Italy
Marianna Ambrico, Donato Creanza, Mauro De Palma, Teresa Ligonzo, Norman Manna, Valeria Radicci, Luigi Schiavulli

Brookhaven National Laboratory, Upton, NY, USA
Jim Kierstead, Zheng Li

Department of Physics, University of Bologna, Bologna, Italy
Anna Cavallini

National Institute for Materials Physics, Bucharest - Magurele, Romania
Manuela Buda, Sorina Lazanu, Lucian Pintilie, Ioana Pintilie, Andreia-Ioana Popa

University of Bucharest, Faculty of Physics, Romania
Ionel Lazanu

CERN, Geneva, Switzerland
Paula Collins, Karl Aaron Gill, Maurice Glaser, Herbert Hödlmoser, Christian Joram, Michael Moll[*]

Diamond Light Source, UK
Victoria Wright

Universitaet Dortmund, Lehrstuhl Experimentelle Physik IV, Dortmund, Germany
Claus Goessling, Reiner Klingenberg, Jens Weber, Renate Wunstorf

CiS Institut für Mikrosensorik gGmbH, Erfurt, Germany
Ralf Roeder, Dieter Stolze, Hartmut Uebersee

University of Exeter, Department of Physics, Exeter, EX4 4QL, United Kingdom
James Adey, A. Blumenau, J. Coutinho, T. Eberlein, C. Fall, J. Goss, B. Hourahine, Robert Jones, N. Pinho

[*] Co-spokesperson

Fermilab, USA
Rita Coluccia, Simon Kwan, Greg Sellberg

INFN Florence – Department of Energetics, University of Florence, Italy
Emilio Borchi, Mara Bruzz[†]i, Ettore Focardi, Stefano Lagomarsino, Anna Macchiolo, David Menichelli, Stefania Miglio, Monica Scaringella, Silvio Sciortino, Carlo Tosi

University of Freiburg
Simon Eckert, Thies Ehrich, Susanne Kuehn, Ulrich Parzefall

Dept. of Physics & Astronomy, Glasgow University, Glasgow, UK
Richard Bates, Andrew Blue, Peter Bussey, Craig Buttar, Wiliam Cunningham, Freddie Doherty, Lars Eklund, Celeste Fleta, Alison G Bates, Lina Haddad, Grant James, Keith Mathieson, J. Melone, Val OShea, Chris Parkes, David Pennicard, Aldo Saavedra

Institute for Experimental Physics, University of Hamburg, Germany
Peter Buhmann, Devis Contarato, Eckhart Fretwurst, Frank Hönniger, Gunnar Lindström, Uwe Pein, Jörg Stahl

Helsinki Institute of Physics, Helsinki, Finland
Jaakko Härkönen, Katri Lassila-Perini, Panja Luukka, Jukka Nysten, Eija Tuominen, Esa Tuovinen

Ioffe Phisico-Technical Institute of Russian Academy of Sciences, St. Petersburg, Russia
Vladimir Eremin, Igor Ilyashenko, Alexandr Ivanov, Evgenia Kalinina, Alexander Lebedev, Nikita Strokan, Elena Verbitskaya

Institute of Physics PAS and Institute of Electronics Technology, Warszawa, Poland
Adam Barcz

Institute of Electronic Materials Technology, Warszawa, Poland
Andrzej Brzozowski, Pawel Kaminski, Roman Kozlowski, Michal Kozubal, Zygmunt Luczynski, Elzbieta Nossarzewska-Orlowska, Barbara Surma, Piotr Zabierowski

University of Karlsruhe, Institut fuer Experimentelle Kernphysik, Karlsruhe, Germany
Wim de Boer, Alex Furgeri, Frank Hartmann, Valery Zhukov

Institute for Nuclear Research of the Academy of Sciences of Ukraine, Radiation PhysicDepartments
L. Barabash, A. Dolgolenko, A. Groza, A. Karpenko, V. Khivrich, V. Lastovetsky, P. Litovchenko, L. Polivtsev

Department of Physics, Lancaster University, Lancaster, United Kingdom
Timothy John Brodbeck, Duncan Campbell, Alexandre Chilingarov, Gareth Hughes, Brian Keith Jones, Terence Sloan

Lappeenranta University of Technology, Department of Electrical Engineering, Lappeenranta, Finland
Miia Koski, Kari Leinonen, Tanja Palviainen, Tuure Tuuva

Department of Physics, University of Liverpool, United Kingdom
Phillip Allport, Stephen Biagi, Themis Bowcock, Gianluigi Casse, Joost Vossebeld

[†] Co-spokesperson

Jožef Stefan Institute and Department of Physics, University of Ljubljana, Ljubljana, Slovenia
Vladimir Cindro, Irena Dolenc, Gregor Kramberger, Igor Mandic, Marko Mikuž, Marko Zavrtanik

Université catholique de Louvain, Institut de Physique Nucléaire, Louvain-la-Neuve, Belgium
Samia Assouak, Eric Forton, Ghislain Grégoire, Vincent Lemaitre, Otilia Militaru, Krzysztof Piotrzkowski, Pierre Rodeghiero

Belarusian State University, Minsk
Nikolai Kazuchits , Leonid Makarenko

Groupe de la Physique des Particules, Université de Montreal, Canada
Sébastien Charron, Marie-Helene Genest, Alain Houdayer, Celine Lebel, Claude Leroy

State Scientific Center of Russian Federation, Institute for Theoretical and Experimental Physics, Moscow, Russia
Victor Golovine, Eugene Grigoriev, Aleksey Karpov, Sergey Kazakov, Alxander Martemianov, Sergey Rogozhkin, Alexandre Zaluzhny

MPI Munich, Halbleiterlabor, Germany
Ladislav Andricek, Hans-Günther Moser, Rainer Richter, Qingyu Wei

Department of Physics and Astronomy, University of New Mexico, Albuquerque, NM, USA
Igor Gorelov, Martin Hoeferkamp, Jessica Metcalfe, Sally Seidel, Elena Vataga

The National Institute for Nuclear Physics and High Energy Physics (NIKHEF)
Fred Hartjes, Els Koffeman, Harry van der Graaf, Jan Visschers

University of Oslo, Physics Department/Physical Electronics, Oslo, Norway
Giovanni Alfieri, Klaus M H Johansen, Andrej Kuznetsov, Edouard Monakhov, Bengt G. Svensson

Dipartimento di Fisica and INFN Sezione di Padova, Padova, Italy
Dario Bisello, Andrea Candelori, Vladimir Khomenkov, Alexei Litovchenko, Devis Pantano, Riccardo Rando

I.N.F.N. and Università di Perugia - Italy
Gian Mario Bilei, Daniele Passeri, Marco Petasecca, Giorgio Umberto Pignatel

Universita` di Pisa and INFN sez. di Pisa, Italy
Laura Borrello, Suchandra Dutta, Alberto Messineo, Gabriele Segneri

Institute of Physics, Academy of Sciences of the Czech Republic, Praha, Czech Republic
Jiri Popule, Petr Sicho, Michal Tomasek, Vaclav Vrba

Charles University Prague, Czech Republic
Jan Broz, Zdenek Dolezal, Peter Kodys, Alexej Tsvetkov, Ivan Wilhelm

Czech Technical University in Prague, Czech Republic
Dominik Chren, Tomas Horazdovsky, Zdenek Kohout, Vladimir Linhart, Stanislav Pospisil, Michael Solar, Vít Sopko, Bruno Sopko, Josef Uher

Paul Scherrer Institut, Laboratory for Particle Physics, Villigen, Switzerland
Roland Horisberger, Tilman Rohe

Purdue University, USA
Gino Bolla, Daniela Bortoletto, Kim Giolo, Jun Miyamoto, Carsten Rott, Amitava Roy, Ian Shipsey, SeungHee Son

University of Rochester, USA
Veronique Boisvert, Regina Demina, Sergey Korjenevski, Paul Tipton

Santa Cruz Institute for Particle Physics, USA
Alexander Grillo, Hartmut Sadrozinski, Bruce Schumm, Abraham Seiden, Ned Spencer

Dept of Physics and Astronomy, University of Sheffield, Sheffield, U.K.
Ian Dawson, Paul Dervan

SINTEF ICT, Blindern, Oslo, Norway
Thor-Erik Hansen

Experimental Particle Physics Group, Syracuse University, Syracuse, USA
Marina Artuso

Tel Aviv University, Israel
J. Guskov, Sergey Marunko, Arie Ruzin, Tamir Tylchin

Experimental Physics Department, University of Torino, Italy
Franco Fizzotti, Yiuri Garino, Alessandro Lo Giudice, Claudio Manfredotti

ITC-IRST, Microsystems Division, Povo, Trento, Italy
Maurizio Boscardin, Gian - Franco Dalla Betta, Paolo Gregori, Claudio Piemonte, Alberto Pozza, Sabina Ronchin, Mario Zen, Nicola Zorzi

IFIC, joint research institute of CSIC and Universitat de Valencia-Estudi General, Valencia, Spain
Carmen Garcia, Sergio González Sevilla, Carlos Lacasta, Salvador Marti i Garcia, Mercedes Minano

Institute of Materials Science and Applied Research, Vilnius University, Vilnius, Lithuania
Eugenijus Gaubas, Arunas Kadys, Vaidotas Kazukauskas, Stanislavas Sakalauskas, Jurgis Storasta, Juozas Vidmantis Vaitkus

Contents

1. **Introduction**
2. **Executive Summary**
3. **Defect and Material Characterization**
4. **Defect Engineering**
5. **Pad Detector Characterization**
6. **New Structures**
7. **New Materials**
8. **Full Detector Systems**
9. **Resources**

1 Introduction

The objective of the CERN RD50 Collaboration is the development of radiation hard semiconductor detectors for very high luminosity colliders, particularly to face the requirements of a possible upgrade scenario of the LHC to a luminosity of $10^{35}cm^{-2}s^{-1}$, corresponding to expected total fluences of fast hadrons above $10^{16}cm^{-2}$ and reduced bunch-crossing interval of ~10 ns [1, 2]. This document reports the status of research and main results obtained after the fourth year of activity of the collaboration.

Presently, RD50 counts a total of 262 members with 52 participating institutes. This comprises 43 institutes from 16 different countries in West and East Europe, 8 from North America (USA, Canada) and one from middle east (Israel). During the fourth year of activity two workshops and collaboration board meetings have been held to discuss the recent results and co-ordinate the research activities of RD50: 25-28 June 2006, Prague, Czech Republic and October 16-18, 2006 at CERN. Each workshop has registered a quite high rate of participation, counting an average of 65 participants with about 28 talks. Additionally a dedicated "RD50 workshop on defect analysis in radiation damaged silicon detectors" was held at the University of Hamburg focussing on the investigation of microscopic defects in silicon and resulting in a new common program on defect analysis. More details including all electronic versions of the presentations can be found on the collaboration web-site [3].

Review papers describing the common research activities of the RD50 collaboration have been published in 2003 [4], 2004 [5,6], 2005 [7-9] and 2006 [10-12]. As in the previous years, the research activity of RD50 has been presented in form of oral contributions at several international conferences and workshops [13]:

- International Symposium on the Development of Detectors for Particle, Astroparticle and Synchrotron Radiation Experiments, April 3 - 6, 2006, Stanford Linear Accelerator Center (SLAC), USA [14].
- 4th CMS Workshop on Detectors and Electronics for the SLHC, April 3-4, 2006 Perugia, Italy [15-17]
- 5th International Forum on Advanced Material Science and Technology, June 11 to 14, 2006, Xiangtan, Hunan, China [18]
- RADECS 2006 international workshop, September 27-29, Athens, Greece [19]
- CMS Pixel Group Preparatory Workshop on Future Upgrade, October 9-12, Fermilab,USA [20]
- 6th International Conference on Radiation Effects on Semiconductor Materials, Detectors and Devices, Firenze, Italy, October 10 - 13, 2006 [21]
- 2006 Nuclear Science Symposium, Medical Imaging Conference and 15th International Room Temperature Semiconductor Detector Workshop, October 29 – Nov. 4, 2006 · San Diego, California [22]

The scientific organization of RD50 is organised in two major lines, Material Engineering and Device Engineering, each of the two lines are subdivided into three research lines as shown in Table 1-1. The management of the research lines is assigned to members of RD50 of proven relevant experience (conveners). In 2006 the convenership for the "Pad Detector Characterization" was handed over from Jaakko Haerkoenen (Helsinki) to Gregor Kramberger (Ljubljana). In the framework of the research activity of each research line, working groups are active with specific tasks. Each working group is composed of few institutes, which are directly involved in the research program and co-ordinated by an RD50 member. Table 1-1 lists working groups and common activities within each project, with the corresponding co-ordinator.

Besides working groups, common activities were continued or have been started on subjects of common interest. Some of these activities are partially supported with the RD50 common fund. Examples are the common purchase of MCZ silicon wafers that could only be purchased in big quantities or the expensive processing of a batch of detectors in a 6" processing line with a RD50 common mask.

	Line	Project Convener	Main Research Activity	Working groups and common acitivities
Spokespersons Mara Bruzzi (INFN and Uni. of Florence) and Michael Moll (CERN)	**Material Engineering**	**Defect/Material Characterisation** Bengt G. Svensson Univ. Oslo, Norway	Characterisation of the microscopic properties of standard-, defect engineered and new materials, pre- and post-irradiation.	(1) Common defect characterization of neutron irradiated silicon (G.Lindstroem)
		Defect Engineering Eckhart Fretwurst Univ. of Hamburg, Germany	Development and testing of defect engineered silicon: Oxygen enriched FZ (DOFZ), High res. Cz, Epitaxial, Si enriched with Oxygen dimmers	(1) RD50 wafer procurement (M.Moll)
		New Materials Elena Verbitskaya Ioffe, St.Petersburg, Russia	Development of new materials with promising radiation hard properties: bulk and epitaxial SiC, GaN	(1) SiC (I. Pintilie) (2) GaN (J. Vaitkus)
	Device Engineering	**Pad Detector Characterisation** Gregor Kramberger, Ljubljana Univ., Slovenia	Characterisation of macroscopic properties of heavily irradiated single pad detectors in different operational conditions.	(1) Standardisation of macroscopic measurements (A.Chilingarov) (2) Technotest (V.Eremin)
		New Structures Richard Bates Univ. of Glasgow, UK	Development of 3D, semi-3D and thin detectors and study of their pre- and post-irradiation performance.	(1) 3D (M.Boscardin) (2) Semi-3D (Z.Li)
		Full Detector Systems Gianluigi Casse Univ. of Liverpool, UK	- Systematic characterisation of segmented (microstrips, pixels) LHC-like detectors. - Links with LHC experiments	(1) Pixel detectors (D.Bortoletto- T.Rohe) (2) Radhard electronics (H.Sadrozinski, SCIPP)

Table 1-1.: Organisation structure of the research activity in RD50.

Taking into account the scientific results obtained over the last four years in the reseach line of "New Materials", it was decided in the end of 2006 to suppress this research line and reduce it to project level within the research line "Pad Detector Characterization". This change in the RD50 organization will put in place from 2007 onwards.

In the next section our scientific work is reviewed in an executive summary. This section is followed by six sections describing the status of the research activities of each individual research line. Finally a work plan, milestones and an overview about the needed resources for 2007 are given.

References for Chapter 1

[1] R&D Proposal - DEVELOPMENT OF RADIATION HARD SEMICONDUCTORDEVICES FOR VERY HIGH LUMINOSITY COLLIDERS, LHCC 2002-003 / P6, 15.2.2002.
[2] RD50 Status Report 2004 – Radiation hard semiconductor devices for very high luminosity colliders, CERN-LHCC-2004-031 and LHCC-RD-005, January 2005
[3] RD50 collaboration web site: http://www.cern.ch/rd50/.
[4] **Michael Moll** on behalf of the CERN RD50 collaboration, "Development of radiation hard sensors for very high luminosity colliders - CERN - RD50 project – "Nucl. Instr. & Meth. in Phys. Res. A 511 (2003) 97-105.
[5] **Mara Bruzzi** on behalf of the CERN RD50 Collaboration, "Material Engineering for the Development of Ultra-Radiation Hard Semiconductor Detectors", Nucl. Instrum. & Meth. A 518, 1-2, 2004, 336-337.
[6] **Panja Luukka** on behalf of the CERN RD50 Collaboratin "Status of Defect Engineering Activity of the RD50 Collaboration" Nucl. Instrum. & Meth. A 530, 1-2, 2004, 152-157.
[7] **Michael Moll et al. (RD50 Collaboration)**, "Development of radiation tolerant semiconductor detectors for the Super-LHC", NIMA 546 , 99-107 (2005).
[8] **M. Bruzzi et al. (RD50 Collaboration)**; "Radiation-hard semiconductor detectors for SuperLHC"; NIMA, 541, 189-201 (2005).
[9] **F.Fretwurst et al. (RD50 Collaboration)**, "Recent advancements in the development of radiation hard semiconductor detectors for S-LHC"; NIMA 552, 7-19 (2005).
[10] **Andrea Candelori** on behalf of the CERN RD50 collaboration, "Radiation-hard detectors for very high luminosity colliders"; NIMA, 560, 103-107, (2006).
[11] **Michael Moll** on behalf of the CERN RD50 collaboration, "Radiation tolerant semiconductor sensors for tracking detectors"; Michael Moll; NIMA, 565, 202-211, (2006).
[12] **Panja Luukka,** "Recent progress of CERN RD50 Collaboration";; Trans. Nonferrous Met. Soc. China, 16, s133-s136, (2006).
[13] Electronic versions of the talks are available on the RD50 www-page under http://www.cern.ch/rd50/doc/
[14] "Radiation Tolerant Tracking Detectors", Mara Bruzzi (Florence University) on behalf of the RD50 collaboration.
[15] "Recent RD50 Results on p-type and MCz n-type", Donato Creanza (Bari University) on behalf of the RD50 collaboration.
[16] "3d Detector studies by RD50", Maurizio Boscardin (Trento).
[17] "Epitaxial Silicon Detectors for Particle Tracking", Georg Steinbrück (Hamburg University).
[18] "Development of Radiation Hard Sensors for High Luminosity Colliders – CERN RD50 Collaboration - "Panja Luukka(Helsinki Institute of Physics) on behalf of RD50.
[19] "Radiation Tolerant Silicon Sensors for Tracking Detectors in the Super-LHC", Michael Moll (CERN) on behalf of RD50
[20] "The work of the CERN RD50 Collaboration", Mara Bruzzi (Florence)
[21] "Recent Results of the RD50 Collaboration", Gregor Kramberger, Ljubljana
[22] "Radiation hard semiconductor devices for very high luminosity colliders", Laura Borrello, Pisa

2 Executive Summary

2.1 Defect and Material Characterization (DMC)

- *Studies on the oxygen dimer and related defects:* It is believed that the beneficial effect of oxygen is not only due to the interstitial oxygen (O_i) concentration but is also connected to the oxygen dimer (O_{2i}) concentration. The latter may determine the generation of shallow donors (BDs) in the material that can compensate the build up of negative space charge by the deep acceptors. In order to better understand the role of the oxygen dimer, SIMS studies on the oxygen depths distribution in EPI and MCZ silicon have been performed and the annealing of the IO_2 defect was investigated in detail. Furthermore, a TSC study on the growth of the BD defect was conducted which suggests that the beneficial annealing could be directly linked to this defect.

- *Modeling of defect reactions in irradiated silicon:* In 2002 the existence of the Si_{FFCD} (fourfolded coordinated silicon defect) in hadron irradiated silicon was predicted. Simulations have now been conducted to understand what would be the impact of this defect on the macroscopic properties of silicon detectors after different kind of irradiations. The results are in contradiction to experimental data and thus ask for a change in the modeling or might even contradict the existence of the Si_{FFCD} defect.

- *Measurements of charge carrier trapping times* with the transient grating method have been conducted on standard and oxygenated silicon. The results are presently under comparison with data taken by other methods.

- The *depth dependence of defect interactions in FZ silicon* has been investigated using the depth distribution of the carbon interstitial defect as tracer. Crystals with <100> and <111> orientation have been compared.

- The *charge carrier removal in 4H- and 6H- Silicon Carbide* was studied arriving to the conclution that due to a strong radiation induced trapping the material is presently not suitable for particle detectors.

2.2 Defect Engineering (DE)

- *Standard and Oxygen enriched FZ silicon (DOFZ)*: Both material types have been studied mainly for comparison with the other type of materials under investigation by the RD50 collaboration as for example high resistivity Magnetic Czochralski silicon (MCz), epitaxial silicon (EPI) or pre-irradiated FZ and MCz silicon. In 2006 also intense work on p-type material has been performed, motivated by promising results of improved charge collection properties in structured detectors (strip detectors).

- *Thermal donor generation in MCZ silicon:* The very high oxygen content of MCZ silicon in the order of $\approx 4\text{-}6\cdot10^{17}$ cm^{-3} facilitates an efficient generation of Thermal donors in the material due to heat treatments. An effect which has been exploited to tailer the initial resistivity and the radiation response of the detector material. In 2006 p- and n-type MCZ silicon detectors have been enriched with Thermal donors via various heat treatments. Results on the radiation induced macroscopic changes of the detectors as well as the microscopic

formation of defects in these materials have been investigated and are presented in the DMC and PDC chapters of this report.

- *Oxygen dimers in epitaxial and MCZ silicon*: In 2005 RD50 had demonstrated that the space charge sign of n-type epi-layers with a thickness of 25, 50 and 75 μm and a resistivity of 50 Ω·cm stays positive after 24 GeV/c proton as well as neutron irradiatin up to fluences of 10^{16} cm^{-2}. This is a clear indication for the radiation induced creation of shallow donors in theses materials overcompensating the radiation induced acceptors. The present assumption is that the radiation induced donor is related to oxygen dimers O_{2i} and not interstitial oxygen O_i. Various investigations into the oxygen dimer production have been performed in 2006 on epi and MCZ silicon, which are particularly difficult as the oxygen dimer does not exhibit a level in the bandgap and can thus not be measured with the most common microscopic tools. In the line of this research the diffusion oxygenated epitaxial silicon EPI-DO was introduced as a new defect engineered material. The EPI and MCZ materials were characterized with the SIMS method for their oxygen depth profile and TCT and DLTS analyses were used to investigate the formation of the IO_{2i} defect in the materials. By measuring the IO_{2i} depth profile it was concluded that the IO_{2i} defect can be used as an indicator for the oxygen dimer depth profile.

- *Pre-irradiated detectors* are detectors produced from a silicon material that prior to processing has been exposed to an irradiation usually performed in a nuclear reactor. It is assumed that this pre-irradiation is forming gettering sites inside the material that are reducing the detector radiation damage. Neutron radiation responses of pre-irradiated n- and p-type FZ detectors have been compared to the response of standard and NTD (Neutron Transmutation Doped) detectors. Some indications have been found for a reduced negative space charge built up in the pre-irradiated detectors.

2.3 Pad Detector Characterization (PDC)

- A detailed study on the *electric field profile in irradiated detectors* was conducted using simulations and experimental data obtained with the TCT technique. The simulations could well reproduce the experimentally observed double junction effects. One result is that although the shape of the electric field is complex in most cases one of the junctions clearly dominates it. This dominating junction defines the sign of the space charge and the effective doping concentration obtained from the depletion voltage is approximately giving the correct value for the effective doping concentration in the electric field close to the dominating junction.

- *Studies on the effective doping concentration in different materials:* Test detectors made from n- and p-type MCZ, EPI (25 to 75μm) and DOFZ silicon have been irradiated with 23 GeV protons and reactor neutrons. The effective doping concentration extracted by CV measurements has been parameterized as function of fluence and annealing time for the various materials allowing now for a detailed comparison of the materials.

- The *effect of biasing* on the depletion voltage of irradiated MCZ detectors was investigated. A significant change in the depletion voltage was found after the detector was set under bias and confirmed in CCE measurements as function of voltage. No influence on the leakage current was observed.

- The radiation induced *leakage current increase* of 50 μm thick epitaxial silicon detectors was found to not scale linearly with the hadron fluence. A very surprising result taking into account that all other silicon detector materials exhibit a linear behavior.

- Further studies on the *effective trapping times* of irradiated detectors were conducted to improve the parameterization of this very important damage parameter.

- *Charge collection efficiency measurements* with radioactive sources were conducted in several institutes in 2006. One important outcome is that the charge loss at very high fluences is lower than would be expected from present effective trapping time measurements. A result that indicates that the trapping times at very high fluences are probably lower than the ones that were extrapolated from measurements obtained after irradiation fluences of below 10^{15} cm^{-2}.

2.4 New Materials (NM)

- *Silicon Carbide - Defects:* Schottky diodes and p^+-n junction diodes produced from n-type 4H-SiC epitaxial layers were studied in 2006. A detailed investigation on the microscopic radiation defects and the change of the I-V, I-T and CCE(V) characteristics after 1 MeV neutron irradiation was performed. The I-T measurements and the defect transient spectroscopies by DLTS and PICTS have shown that the trapping centers which play the key role in the decrease of the charge collection efficiency are related to deep levels with an activation energy above 1.04 eV. The deepest defects observed, SN6 and SN7, with a concentration of the order of 10^{15}-10^{16} cm^{-3} after a fluence of about $8x10^{15}$ cm^{-2}, have been identified as the main reason for the detector degradation. These defects can be tentatively assigned to a defect complex involving carbon-vacancy, carbon and silicon-vacancy defects.

- *Silicon Carbide – Annealing*: The experiments on annealing of SiC p^+-n diodes irradiated by 1 MeV neutrons have shown partial recovery of the reverse current and the collected charge. After annealing for 30 minutes at 200°C the collected charge generated by MIPs, for a diode irradiated with a fluence of 3×10^{14} n/cm^2, increased from 1800 e^- to 2200 e^-. By increasing the temperature up to 400°C, further improvement of characteristics occurred: the leakage current further decreased while the collected charges improvement reached 40%.

- *Silicon Carbide – Proton irradiation*: Irradiation of detectors with 8 MeV protons and operating tests in reverse bias and forward bias modes have been performed. The data on forward bias mode allowed separating the contribution of electrons and holes to the CCE of detectors and definition of $\mu\tau_{e,h}$ values. At a fluence of 3×10^{14} cm^{-2} polarization occurs at any polarity of the voltage, caused by carrier trapping to the deep levels of radiation induced defects. The degradation of the signal in time due to polarization prevents a proper detector application in the spectroscopy mode while operation in the counting mode remains possible.

- *Gallium Nitride:* It was shown that the substrate related defects play an important role and the detector properties were improved by increasing the epi-layer thickness. The maximal CCE for α-particles in the new series of the samples with a larger GaN layer thickness was ~ 23% after 10^{16} p/cm^2 and 17% after 10^{16} n/cm^2. A new type of GaN diode structure with a defined electric field region was processed and studied. The definition was achieved due to inductively coupled plasma etching of the epilayer to get the contact to the n* buffer layer that improved the CCE in non-irradiated detector.

2.5 New Structures (NS)

- *Thin detectors:* 50 μm thick FZ silicon detectors with various resistivities (3kΩcm to 150Ωcm) have been produced using the wafer bonding technique. In a first irradiation test with 23 GeV protons the high resistivity samples (3KΩcm) were tested and found to behave as expected.

- *3D detectors of single column type (3D-stc)* were characterized with the CV and IV methods and tested in a position sensitive TCT setup. The measurements were found to be in good agreement with simulations performed with ISE-TCAD simulations. Charge collection measurements with a radioactive source and fast LHC read out electronics were performed on 3D-stc strip detectors. In the used system an efficiency close to 100% was reached applying only 7V to the sample.

- The work towards a *full 3D* detector was continued. Detectors with two types of columes (p- and n-doped) reaching 250 μm into the detector volume from the opposide surfaces are under development and prototype production runs are under way. The devices have extensively been simulated to optimize the production.

2.6 Full detector Systems (FDS)

- *Non inverting silicon materials*: It is now fully established that reading-out finely segmented silicon detectors from the side were the high electric field is located after irradiation gives the major contribution to radiation hardness. This is due to the fact that charge trapping is the main cause of charge collection deficit, because it reduces the lifetime of charge carriers and therefore their collection distance. Short collection times are thus required to maximize the charge collection. Traditional p-in-n detectors suffer from the migration of the junction to the backplane after irradiation (the space charge type inversion), with the high electric field being located on the non-segmented side of the device. The development and test of non-inverting silicon materials, where the high electric field is always located on the segmented side of the detector, has been the main subject of the FDS project during the year 2006. The candidates as non-inverting silicon materials are p-type substrates (both FZ and MCZ) and n-type MCZ, although this latter has been shown to invert after high dose of neutron irradiation.

- *Gamma irradiation of p-type detectors:* When n-side read-out is used on segmented detectors, as for example in n-in-p geometries, a method for interstrip isolation has to be used. Possible interstrip isolation methods are p-spray, p-stops or a combination of the two (moderated p-spray). Since the p-type detectors are the most promising candidate for non-inverting detectors, it is very important to study the effects of ionizing irradiation on the electrical properties of the silicon detectors, like the interstrip capacitance, the interstrip isolation, break-down voltage and leakage current. A dedicated study was performed with a ^{60}Co irradiation on p-type detectors originating from the SMART project. The investigation of surface effects showed no dependence on the p-type wafer type (FZ vs. MCz), but large dependence on the surface treatment (high vs, low p-spray dose). Saturation was observed for the interstrip capacitance at about 100 kRad, with very little annealing. The flatband voltage and the oxide charge showed also saturation at about 150 kRad, but in addition a very large annealing by a factor 3. The breakdown voltage was increased by the gamma irradiation, but also showed very strong annealing. The strips showed good isolation before and after irradiation and annealing.

- *p-spray isolation studies:* A dedicated simulation with the ISE-TCAD package on the breakdown behavior of different types of p-spray isolation was performed and compared to devices produced with different p-spray isolations. A good agreement between simulation and measurement was found. The breakdown voltage of the non-irradiated n-in-p microstrip detectors decreases as the total implanted charge increases. On the other hand, high doses of p-spray are needed to avoid the inversion of the silicon surface in heavily irradiated devices. A compromise solution is necessary. This could be critical for devices fabricated in substrates with low resistivities, such as Czochralski silicon. However, strip isolation is not the major concern in irradiated detectors, and more complete simulations are needed. The electrical

measurements of detectors fabricated with a medium dose p-spray confirm the simulation results. Even if the resulting p-spray profile is lower than the profile predicted by simulation, the devices show good electrical behaviour and the microstrips are properly isolated.

- *Laser test systems:* Testing the CCE of detectors with a laser system offers many advantages over the use of a radioactive source, has however the drawback that the estimation of the total charge injected into the detector is very difficult and might easily change in the course of an experiment. A step towards a higher accuracy was taken by the Prague University by developing a dedicated laser head that monitors the incoming and reflected laser light.

3 Defect and Material Characterization

3.1 Oxygen dimer and the evolution of radiation-induced defects

3.1.1 Introduction

Previous investigations suggested that the beneficial effect of oxygen may not only be connected with the concentration of oxygen interstitial O_i, which influence the generation of deep acceptors (like the I defect [1]), but also with the concentration of oxygen dimers O_{2i}, which may determine the generation of shallow donors (BDs) in the material [2,3] that can compensate the build up of negative space charge by the deep acceptors. These considerations have been the main motivation to conduct systematic studies regarding the involvement of oxygen dimers in the formation of radiation induced defects.

3.1.2 Samples and detectors studied

Silicon diodes manufactured on different kinds of epitaxial layers as well as on high resistivity magnetic Czochralski (MCz) material were investigated in this work. The n-type epitaxial layers with thicknesses of 25 μm and 72 μm were grown on highly Sb doped Cz substrates by ITME [4]. The resistivity of the 25 μm layer was 50 Ωcm, while that of the 72 μm thick layer was 150 Ωcm. The 300 μm MCz wafers with a nominal resitivity of > 600 Ωcm were provided by Okmetic [5]. The processing of the diodes was performed by CiS [6]. For one batch of the 72 μm thick epi layers a special heat treatment for 24 hour at 1100°C preceding the standard processing was implemented in order to increase the oxygen concentration in the epi layer. Diodes produced this way are denoted as EPI-DO while the standard ones are indicated as EPI-ST. Oxygen concentration-versus-depth profiles have been measured by SIMS [7] and are displayed in Fig. 3-1 for all the three different detector materials used after full device processing (the carbon content in the epi-materials was ~$3x10^{15}$ cm^{-3}, which is close to the detection limit of the instrument used). The depth profiles of the EPI-DO and the MCz sample are quite similar with respect to the absolute values as well as shape, showing in both cases a homogenous distribution throughout the bulk material and a decrease near to the surface, most likely caused by out-diffusion. On the other hand the oxygen concentration of the EPI-ST sample exhibits a strong non-homogeneous profile typically observed for samples of fully processed epi-layers without the DO option [8].

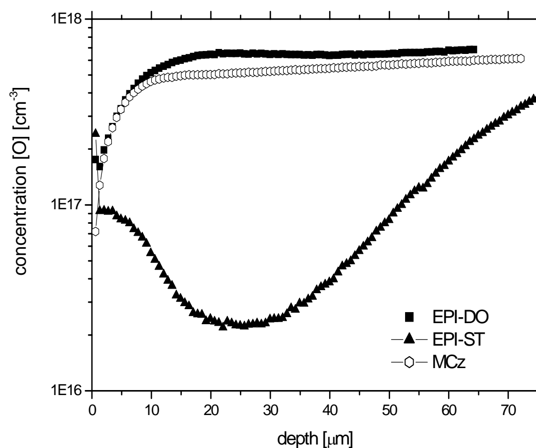

Fig. 3-1. *Oxygen concentration profiles measured with SIMS for EPI-ST, EPI-DO and MCz diodes.*

3.1.3 Results – annealing kinetics for the IO_2 complex

The IO_2 complex was first detected by DLTS in low dose electron-irradiated Cz silicon [9]. Recently, using TSC, the IO_2-defect was detected also in other types of silicon material (DOFZ and Epi/Cz) after exposure to high γ-doses or 24 GeV/c proton fluences (the E(50K) TSC peak in ref. [2,3]).

Isothermal annealing studies of the IO_2 defect complex at different temperatures have been performed for the first time. For this annealing experiment EPI-ST diodes with a thickness of 25 µm were irradiated with neutrons up to $1x10^{12}$ cm^{-2} and annealed at 80°C, 100°C and 120°C. The annealing data for the mentioned three temperatures are displayed in Fig. 3-2 together with their fits. The Arrhenius plot in Fig.3-3 of the extracted time constants reveals a frequency factor of about k_0 = $3.5x10^{-12}$ s^{-1} and an activation energy of E_A =1.29 eV. Thus, with a first order kinetics and the frequency factor k_0 close to the most abundant phonon frequency, it is very likely that the annealing of the IO_2 defect is due to dissociation.

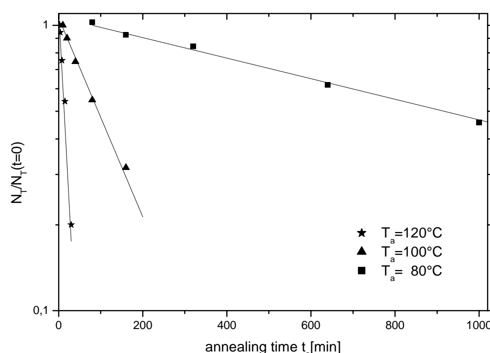

Fig. 3-2. *Isothermal annealing of the IO_{2i} defect at different temperatures T_a. Measurement performed on a 25 µm EPI-ST detector irradiated with $\Phi eq=1x10^{12}$ cm^{-2} reactor neutrons.*

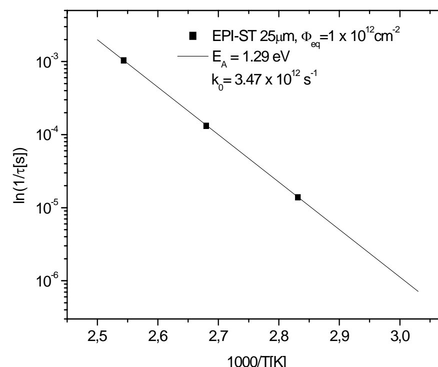

Fig. 3-3. *Arrhenius plot for the thermal activation of the IO_{2i} defect after irradiation with $\Phi_{eq}=1x10^{12}$ cm^{-2} reactor neutrons. EPI-ST samples with 25µm thick layer.*

3.1.4 Results – bistable donor (BD) center

As previously reported [2,3], the BD is generated in material with high concentration of oxygen. The irradiation induced BDs are able to even overcompensate the negative space charge introduced by deep acceptors such that no “type inversion” appears in DOFZ material or 50 µm epitaxial silicon even after very high doses [2,10]. The BD center was detected in high resistivity material via two TSC signals – BD (98K) and BD tail - indicating that the BD center can exist in two configurations, labelled in the following as A and B, respectively. A strong similarity of the BD complex to thermal double donors TDD2 and the well known fact that oxygen dimers O_{2i} are precursors for the formation of thermal donors (see [9]) leads to the assumption that dimers are also involved in the formation of BDs. Similar to the earlier stage TDD, structural transformations between the two possible BD configurations (A and B) may be achieved by different illumination or bias conditions during the cooling procedure before the TSC measurement [2]. However, in previous TSC studies on high resistivity samples or lightly doped epitaxial layers subjected to high irradiation levels ($2\text{-}4x10^{14}cm^{-2}$) only the configuration A could be directly analysed. Present investigations on lightly doped samples exposed to 1MeV neutron fluences of $5x10^{13}$ cm^{-2} reveal the direct detection of both A and B, as shown in Fig. 3-4.

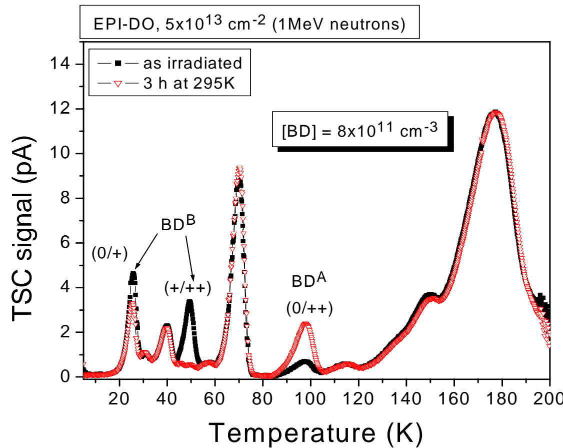

Fig. 3-4 *TSC spectra recorded on a EPI-DO diode as irradiated to $5x10^{13}$ n/cm^2 and after storage for 3 hours at 295 K.*

In the TSC spectrum measured directly after irradiation a peak at 49 K (attributed to $BD^{+/++}$) is recorded. It vanishes after a short storage time of 3 hours at room temperature, but during a second measurement a strong increase of the (0/++) transition of the BD center is observed. The donor activity of both BD transitions is proven by the temperature shift of their peak position as function of the applied bias voltage (i.e., Poole-Frenkel effect on the rate of electron emission). For the EPI-DO diode the BD introduction rate could be accurately evaluated resulting in a value of $g(BD^{0/++})$ = $1.7x10^{-2}$ cm^{-1} which represents the rate of positive charge introduced by the BD in the space charge region. TSC measurements on all investigated materials (MCz, EPI-ST, EPI-DO) demonstrate that shallow donors (monitored via the BD^A configuration) are generated in both the epi-materials but in a much lower concentration in the MCz material possibly suggesting a higher concentration of competing 'reaction channels' for migrating defects in the latter diodes.

An important issue concerns the annealing behaviour of the BD centers. In Fig. 3-5, the BD concentrations measured after different annealing times at 80 ^{0}C are presented. It can be observed that for all materials the concentration of BDs increases during the first 80 minutes at 80 ^{0}C. This behaviour relates the growth of BD centers with the so called "beneficial annealing".

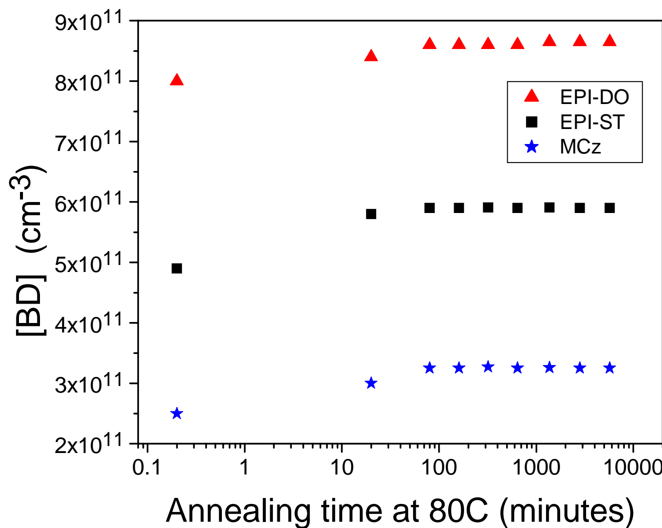

Fig. 3-5 *The concentration of BD centers in EPI-DO, EPI-ST and MCz samples*

3.2 Modeling of defect reactions in irradiated silicon

In 2002, using state of the art plane wave density functional theory, Goedecker et al.[11] predicted the existence of a new type of primary defect: Si_{FFCD} (**F**our**f**olded **C**oordinated silicon **D**efect) that is a pseudo-vacancy. It is obtained by moving atoms from the initial positions, but this displacement does not break the bonds with the neighbours. The bond lengths are between 2.25÷2.47 Å and angles vary in the 97÷116° range. So, the bond length and angle do not deviate significantly from their bulk values. The formation energy is 2.45 eV (for p-type silicon), 2.42 eV (intrinsic), 2.39 eV (n-type), i.e. *lower than the energy of formation of both vacancies and interstitials.*

Assuming the following characteristics for the Si_{FFCD} defect

- It represents about 10% from all vacancies generated per act of interaction,
- Has an energy level in the band gap between E_c – (0.46 ÷ 0.48) eV,
- Has a capture cross section between $(5\cdot\div 10)\times 10^{-15}$ cm^2
- Ratio $\sigma_p/\sigma_n = 1 \div 5$.

the experimentally observed evolution as a function of dose and post-irradiation time of the leakage current and effective carrier concentration can be reproduced by simulations employing rate equations and 'ordinary' defect reactions. This holds, in particular, for hadron irradiation, which is, indeed, a new and encouraging accomplishment [12], as illustrated in Fig.3-6 for the leakage current vs. time evolution after different kinds of irradiation. On the other hand, the assumed properties for the Si_{FFCD} defect are in direct contradiction to experimental results, reported by numerous groups, regarding defect generation in irradiated silicon, i.e., there is scarce experimental evidence for the existence of a defect with such prominent characteristics as those assigned to Si_{FFCD}. Further work is being pursued to resolve this intriguing issue, including high resolution electron microscopy studies [13].

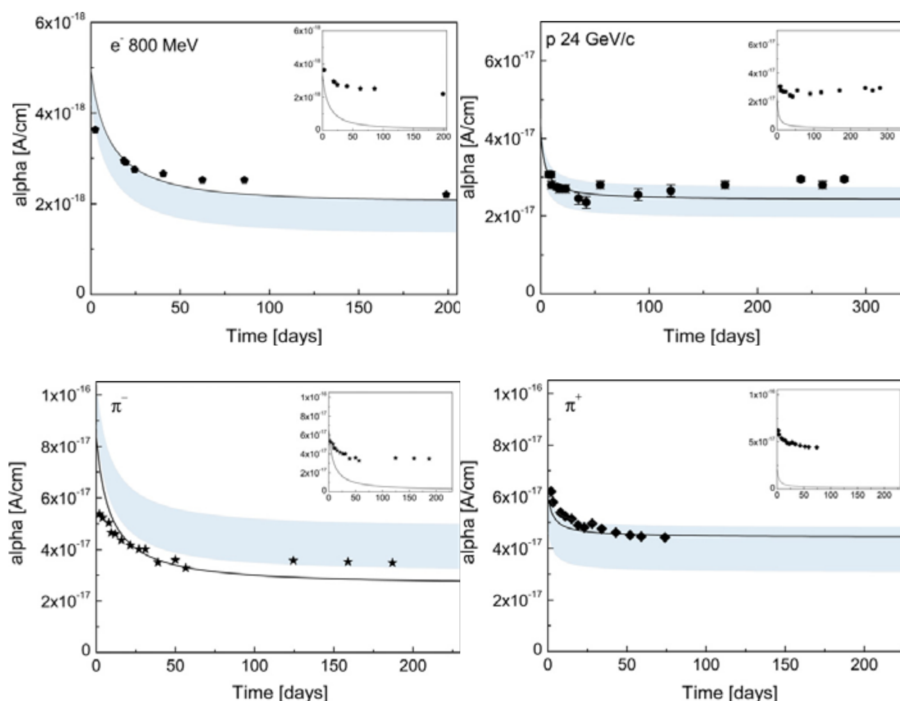

Fig. 3-6 *(a)–(d) The damage constant of the leakage current as a function of time after irradiation at room temperature, with: (a) electrons of 800MeV kinetic energy; (b) protons of 24 GeV/c momentum; (c) and (d) negative and positive pions at 350MeV/c. Inset: comparison between experimental data (points) and model calculations without the contribution of the Si_{FFCD} defect (continuous line).*

3.3 Measured charge carrier trapping times in irradiated silicon

Direct measurements of the charge carrier trapping time in Si diodes irradiated by 24 GeV/c proton up to a fluence of $1x10^{15}$ cm^{-2} has been conducted employing the transient grating technique [14]. The measurements were performed at room temperature and the results for a number of different fluences are depicted in Fig.3-7 for standard diodes (CE) and diffusion-oxygenated (CH) ones, processed by CiS [6]. The inverse trapping time, which is proportional to the trap concentration, is displayed in Fig.3-8 as a function of the proton fluence. Despite a limited amount of data, the trap generation rate appears to be higher in the CH-diodes by ~30 % relative to CE-diodes, which is possibly related to a higher generation of vacancy-oxygen centers in the former ones. At high fluences, deviations from a linear relationship occur indicating a different type of dominating trapping center than at the low fluences or a change of the capture coefficient of the trap [15].

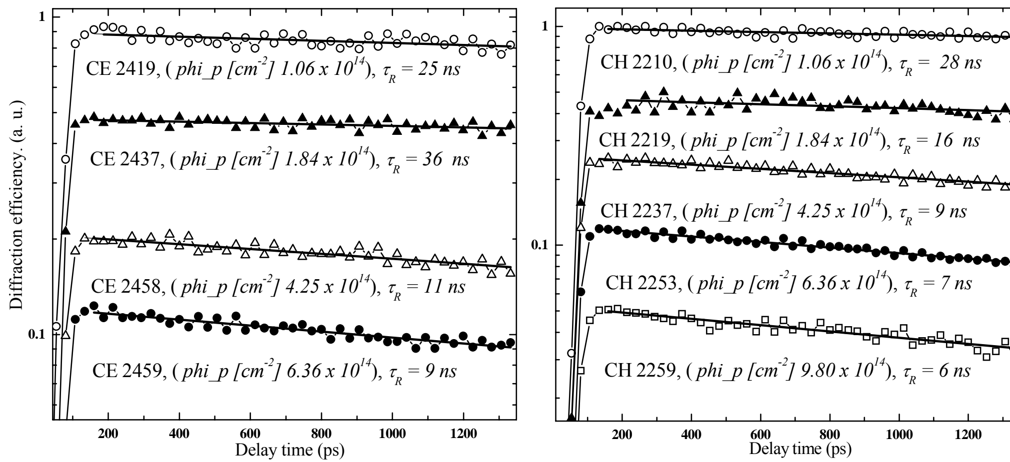

Fig.3-7 *Diffraction efficiency (proportional to the square of the free carrier concentration) versus time for standard (CE) and oxygenated (CH) diodes irradiated with different proton fluences.*

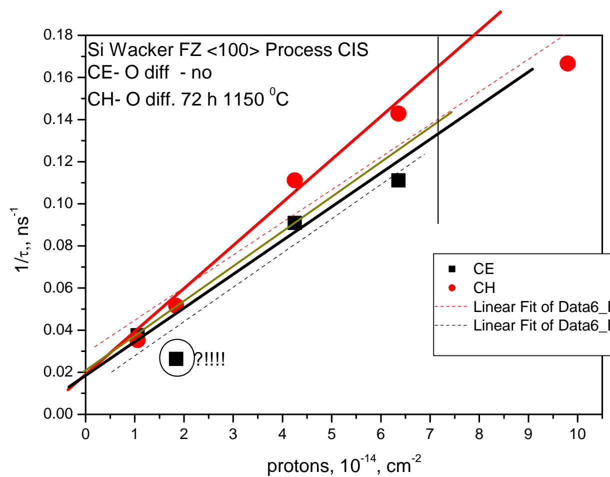

Fig.3-8 *Inverse trapping time (proportional to the trap concentration) versus proton fluence for the CE and CH diodes.*

3.4 Depth dependence of defect interactions in standard FZ-Si detectors

Detailed DLTS measurements have been undertaken on standard FZ-Si detectors irradiated with 6 MeV electrons at room temperature. In particular, the time evolution of the carbon interstitial concentration as a function of depth has been studied and found to be hinge strongly on the depth distributions of interstitial oxygen and substitutional carbon. This is illustrated in Fig. 3-9 showing the remaining fraction of interstitial carbon (C_i) as function of depth after annealing at 60 ºC for 400 minutes in two diodes with different crystal orientation. In the near surface region (<30 μm) the remaining fraction of C_i decreases rapidly which presumably reflects a high concentration of O_i-traps formed by in-diffusion of oxygen during the device processing. Hence, a non-homogenous depth distribution of impurities/traps has a profound influence on the defect formation/annealing kinetics and needs to be accounted for when evaluating the radiation hardness of standard FZ-Si detectors.

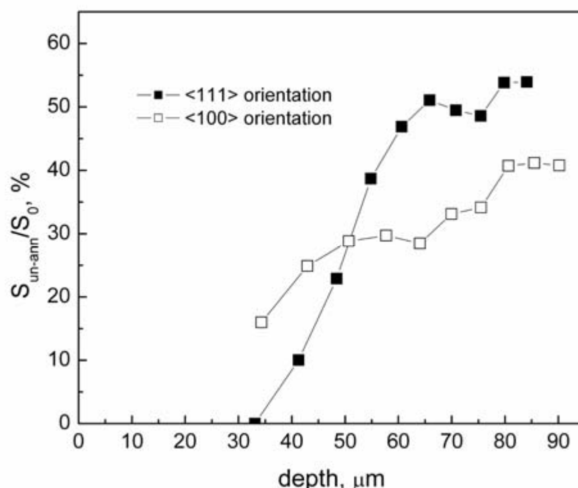

Fig. 3-9 *Depth dependence of remaining fraction of interstitial carbon in <111> (filled symbols) and <100> (empty symbols) detectors after annealing at 60 °C during 400 minutes.*

3.5 Charge carrier removal in irradiated n-type Silicon Carbide

Silicon carbide (SiC) is frequently claimed to be radiation-hard but the amount of real evidence for such a claim is scarce. In fact, studies on low-fluence ion-implanted epitaxial layers of 4H-SiC showed a reduction in the free carrier concentration about 10 times larger than that in n-type silicon for identical implant conditions [16]. In this effort we have investigated the charge carrier removal in epitaxial layers of n-type (nitrogen-doped) 4H-SiC and 6H-SiC grown by chemical vapour deposition and irradiated with 6 MeV electrons at room temperature. The main analysis techniques used are CV (1 kHz to 1 MHz probe frequency), DLTS and Admittance spectroscopy. The results are summarized in Table 3-1 and the loss of responding carriers (compensation) with fluence is about one order of magnitude higher than in Si. No evidence for inversion from n-type to p-type conductivity is found

Isochronal annealing studies reveal gradual recovery of the charge carriers over a wide temperature interval ranging from 200 to 1350 ºC depending on fluence and polytype. In general, the 6H polytype exhibits a lower loss of responding carriers than 4H for a given fluence, and the major features of the results can be quantitatively explained by trapping of free electrons at deep-acceptor type defects. The main deep levels responsible for the trapping are attributed to the so-called $Z_{1/2}$ and $EH_{6/7}$ defects in 4H-SiC with positions at about 0.7 and 1.5 eV below the conduction band edge, respectively. In 6H-SiC, the corresponding centers are the so-called $E_{1/2}$ and R defects with positions at about 0.4 eV and 1.3 eV below the conduction band edge, respectively. The more shallow level

positions in 6H than in 4H is found to be dominant reason for the lower loss of responding carriers at a given probing frequency during CV measurements.

In conclusion, these data do not favor the use of 4H- or 6H-SiC as a material for particle detectors because of the strong charge carrier trapping, unless the material can be engineered during growth to suppress the formation of these deep acceptor-type defects [17].

TABLE 3-1. Survey of the samples used and carrier response before and after irradiation.

Polytype	Electron dose (cm^{-2})	Initial net carrier concentration (cm^{-3}) (CV, 1 MHz)	Carrier concentration after irradiation (From CV, 1 MHz) (cm^{-3})
4H	2×10^{15}	4.3×10^{15}	Compensated
4H	4×10^{15}	4.7×10^{15}	Compensated
4H	8×10^{15}	4.8×10^{15}	Compensated
4H	1.6×10^{16}	5.0×10^{15}	Compensated
6H	2×10^{15}	6.3×10^{16}	4.1×10^{15}
6H	4×10^{15}	5.4×10^{15}	Compensated
6H	8×10^{15}	7.0×10^{16}	Compensated
6H	1.6×10^{16}	4.8×10^{15}	Compensated

References

1. I. Pintilie, E. Fretwurst, G. Lindstroem and J. Stahl, Appl. Phys. Lett. **82**, 2169 (2003)
2. I. Pintilie et al., Nucl. Instr. & Meth. A **514** 18 (2003)
3. I. Pintilie, M. Buda, E. Fretwurst, G. Lindström, J. Stahl, Nucl. Instr. & Meth. A **556**, 197-208 (2006)
4. ITME, Institute for Electronics Materials Technology, Warsaw, Poland
5. Okmetic Oyj, Vantaa, Finland
6. CiS Institut für Mikrosensorik gGmbH, Erfurt, Germany
7. A. Barcz SIMS laboratory, Institute of Physics, Warsaw, Poland
8. G. Lindström, I. Dolenc, E. Fretwurst, F. Hönniger, G. Kramberger et al., Nucl.Instr. & Meth. A **568**, 66-71 (2006)
9. J.L. Lindström, T. Hallberg, J. Hermansson, L.I. Murin, B.A. Komarov, V.P.Markevich, M. Kleverman, B.G. Svensson, Physica B **308-310**, 284-289 (2001)
10. G. Kramberger, D. Contarato, E. Fretwurst, F. Hönniger, G. Lindström, I.Pintilie, R. Röder, A. Schramm, J. Stahl, Nucl. Instr. & Meth A **515** 665-670 (2003)
11. S. Goedecker, Th. Deutsch, L. Billard, Phys. Rev. Lett. **88**, 235501 (2002)

12. I. Lazanu and S. Lazanu, Phys.Scr. **74**, 201 (2006)
13. L. Fedina , A Chuvilin,. A Gutakovskii, Microscopy & Microanalysis 10, Supplement 2 (2004), (Proceedings of Microscopy Conference MC 2004); www.uni-ulm.de/elektronenmikroskopie/mattem/docs/2004.html
14. J. Vaitkus, K. Jarasiunas, E. Gaubas, L. Jonikas, R. Pranaitis, L. Subacius. IEEE J. Quant. Electronics **QE-22**, 1298-1305 (1986); R. Aleksiejunas, M. Sudzius, T. Malinauskas, J. Vaitkus, K. Jarasiunas, S. Sakai, Appl. Phys. Lett. **83**, 1157-1159 (2003)
15. E.Gaubas, A.Kadys J.Vaitkus and E.Fretwurst, Nucl. Instr. & Meth, to be published.
16. A. Hallén, A. Henry, P. Pellerino, B.G. Svensson, and D. Åberg, Mater. Sci. Eng. B **61-62**, 378 (1999)
17. I. Pintilie, U. Grossner, B.G. Svensson, K. Irmscher and B. Thomas, Appl. Phys. Lett., accepted (2007).

4 Defect Engineering

4.1 Standard and DOFZ silicon

Both standard and oxygenated FZ (DOFZ) silicon is mainly investigated for comparison with high resistivity Magnetic Czochralski silicon (MCz), epitaxial silicon (EPI) or pre-irradiated FZ and MCz silicon. In 2006 intense work had been performed on p-type material, motivated by promising results of improved charge collection properties in structured detectors (strip detectors). In heavily damaged detectors the degradation of the charge collection efficiency by charge carrier trapping is one of the limiting factors for the innermost layers of the tracking detectors in SLHC experiments. In case of strong trapping segmented n^+-p-p^+ structures present the advantage that the signal is dominated by electron collection and, therefore, less trapping is expected due to the higher mobility of electrons (shorter collection time) compared to holes.

4.2 Thermal donor generation in p-tye MCz silicon

Silicon crystals grown by the Magnetic Czochralski (MCz) method have a much higher oxygen concentration ([O] ≈ 4-6·10^{17} cm^{-3}) compared to any oxygen enriched DOFZ material ([O] ≈ 1-3·10^{17} cm^{-3}) due to the growth technology itself.

It has been demonstrated that such high concentration of oxygen will strongly influence the radiation induced creation of oxygen related defects and the defect kinetics resulting in an improved radiation hardness beyond the level observed so far in DOFZ silicon. Furthermore, it is well known that in MCz material different thermal donors can be formed or annihilated by specific heat treatments. This also leads to a further possibility to influence the radiation tolerance of this material. The radiation hardness of n- and p-type MCz devices has been studied by different groups and recent results on the radiation induced change of the macroscopic properties will be presented in section 5 (PDC). Microscopic studies are included in section 3 (DMC). In particular, TSC measurements on irradiated samples have evidenced the introduction of shallow donors.

4.3 Oxygen dimers in epitaxial and MCz silicon

It had been shown that the space charge sign of n-type epi-layers with a thickness of 25, 50 and 75 µm and a resistivity of 50 Ω·cm stays positive after 24 GeV/c proton as well as neutron damage up to fluences of 10^{16} cm^{-2}. For large fluences in epi-diodes the creation of acceptors is obviously always overcompensated by an introduction of shallow donors. The formation of these shallow donors was investigated by the Thermally Stimulated Current (TSC) method and it was demonstrated that the TSC signal due to the shallow donor had a very similar dependence on the material as the average oxygen concentration and the stable damage generation [1, 2]. It is believed that this radiation induced donor is related to oxygen dimers O_{2i} and not interstitial oxygen O_i.

4.3.1 Material properties

In continuation of the research plan new n-type epitaxial layers with a thickness of 72 µm and a resitivity of 150 Ω·cm were grown by ITME. The pad-diodes were manufactured by CiS using different process technologies, either the standard process technology (denoted as EPI-ST) or performing an oxygen enrichment of the epi layer by a heat treatment for 24 hours at 1100 °C (denoted as EPI-DO) preceding the standard process steps. This way not only the oxygen concentration should be manipulated in the epi-layer but also the concentration of oxygen dimers.

The depth profile of the resistivity is displayed in Fig. 4-3-1. The mean value in the range between 1 µm and 65 µm in the epi-layer is (148 ± 4) Ω·cm and in the Sb doped Cz substrate a value of ρ = (9.5 ± 0.3)·10^{-3} Ω·cm is observed.

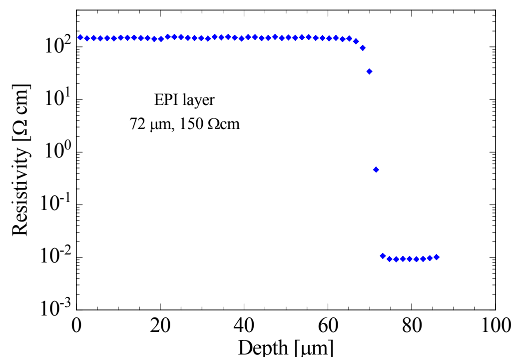

Fig. 4-3-1 Resistivity depth profiles as measured by spreading resistance for 72 μm n-type epi layer.

The oxygen and carbon concentrations had been measured by Secondary Ion Mass Spectroscopy (SIMS) for the epi-layers at different stages of the processing [3]. In Fig. 4-3-2 the depth profiles are displayed for an as grown epi-sample, an EPI-ST sample after being fully processed and for an EPI-DO sample after oxygen enrichment, as mentioned above, followed by the standard process steps.

As can be seen from Fig. 4-3-2 for the as grown sample oxygen is out-diffusing from the Cz substrate into the epi-layer already during the epitaxial growth up to a depth from the epi-layer substrate interface of about 30 μm. For the EPI-ST sample, due to the high temperature treatments during the standard processing procedures (thermal oxidation, activation of implants), the out-diffusion from the Cz substrate continues, and an in-diffusion from the SiO_2-Si interface leads to an error function like depth profile of the oxygen concentration in this surface region. In total a O-depth profile is achieved, which starts at the front side of the epi-layer with a concentration of about $1 \cdot 10^{17}$ cm^{-3}, decreases to a value of $2.2 \cdot 10^{16}$ cm^{-3} in a depth of 25 μm and followed by an increase up to $3.4 \cdot 10^{17}$ cm^{-3} at the epi-layer substrate interface. Similar strong non-homogeneous profiles are typically observed for samples of fully processed epi-layers without the oxygenation treatment [1].

The oxygen enrichment at 1100 °C promotes further the out-diffusion from the substrate resulting in a very homogeneous distribution throughout the main part of the epi bulk ([O] = $6.5 \cdot 10^{17}$ cm^{-3}) excluding the surface region of 10 μm, where a decrease of the oxygen concentration is observed, most likely caused by an out-diffusion of oxygen.

The carbon concentration in the epi-layer varies between $9 \cdot 10^{14}$ cm^{-3} and $1.9 \cdot 10^{15}$ cm^{-3} for the different processing procedures but these values are supposed to be already below the detection limit of the SIMS-method.

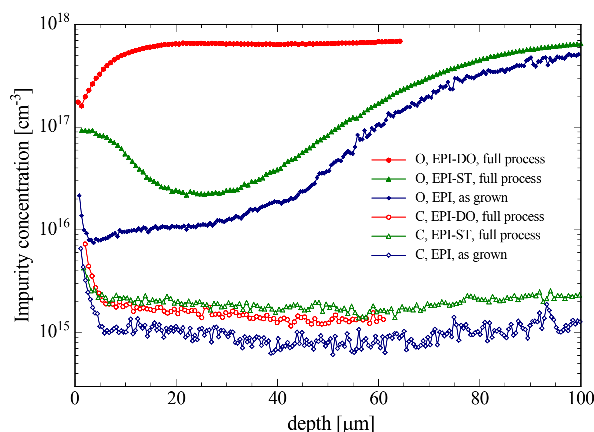

Fig. 4-3-2 Oxygen and carbon concentration profiles measured with SIMS in 72 μm n-type epi-silicon: after oxygen enrichment and full processing (EPI-DO, —●—), after standard processing (EPI-ST, —▲—) and as grown layer (—◆—).

For the MCz sample a SIMS profile of the oxygen concentration is measured ([O] = $5.6 \cdot 10^{17}$ cm^{-2}, see Fig. 4-3-3), quite similar to the EPI-DO result. Also in this case an out-diffusion of oxygen at the

surface can be seen. As the carbon concentration is concerned, a slightly larger value is observed ([C] = $2.5\cdot10^{15}$ cm^{-3}) in comparison to the epi-layer but as mentioned before such a small concentrations is expected to be below the detection limit.

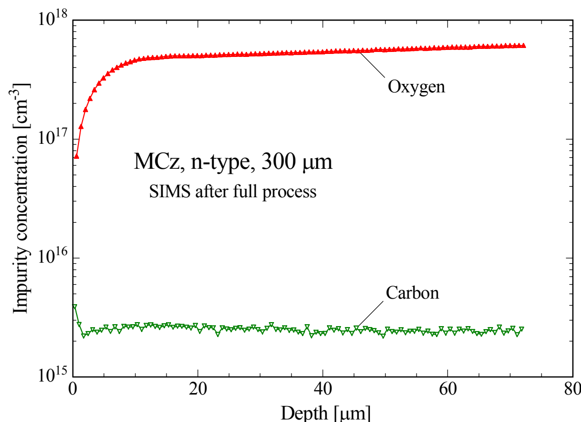

Fig. 4-3-3 Oxygen and carbon concentration profiles measured with SIMS in 300 µm thick n-type MCz silicon after full processing.

4.3.2 The IO_{2i} complex as an indicator for O_{2i} in epi- and MCz-silicon

The IO_{2i} complex had first been detected by DLTS in low dose γ-irradiated Cz silicon [4]. The identification was achieved by comparing its annealing behavior after low γ-doses, resulting from DLTS measurements, with those deduced from IR absorption spectra measured after very high γ-doses. Recently, using the TSC method, the IO_{2i}-defect was detected also in other types of silicon (DOFZ and Epi/Cz) after exposure to high γ-doses or 24 GeV/c proton fluences (the E(50K) TSC peak in ref. [2,5]).

The DLTS spectra of a 72 µm EPI-ST and an EPI-DO diode, as irradiated with 26 MeV protons up to an equivalent fluence of $8.1\cdot10^{11}cm^{-2}$, are presented in Fig. 4-3-4. The most obvious difference between both spectra is the fact that the interstial-dimer complex (IO_{2i}) is only seen in the EPI-DO material while the carbon-interstitial defect (C_i) is only detected in the EPI-ST sample. The formation of the IO_{2i} defect evidences the presence of O_{2i} in the epi material with a high oxygen concentration. The fact that C_i is not seen in EPI-DO does not indicate that the carbon content of this material is much smaller than in the EPI-ST material (see Fig. 4-3-2), it is only an effect of the higher probability for the formation of C_iO_i in the EPI-DO material due to its higher oxygen concentration compared to the standard material [6].

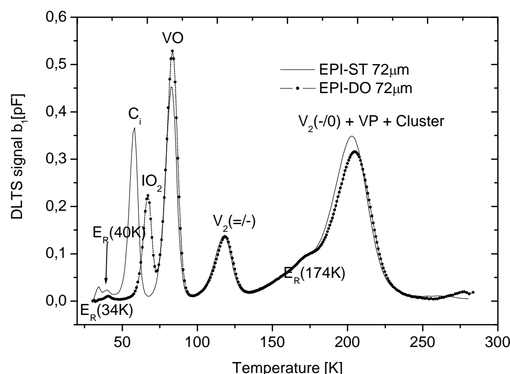

Fig. 4-3-4 DLTS spectra for EPI-ST and EPI-DO diodes irradiated with 26 MeV protons with a fluence of $\Phi_{eq} = 8.1\cdot10^{11}cm^{-2}$. $U_R = -20$ *V* , $U_P = -0.1$ *V* , t_p*=100 ms*, $T_W = 200$ *ms.*

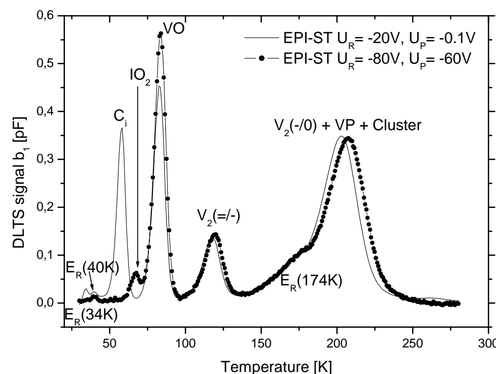

Fig. 4-3-5 Comparison of DLTS spectra of the EPI-ST diode close to the substrate (*UR* = -80*V* , *UP* = -60*V*) and in the region of low oxygen concentration (*UR=-20 V, UP* = -0.1 *V*), t_p*=100 ms*, $T_W = 200$ *ms.*

On the other hand from the absence of the IO_{2i} signal in the EPI-ST diode it cannot be concluded that oxygen-dimers are not present in this material. The IO_{2i} is not visible due to the filling conditions for the traps (U_R = -20 V, Up = -0.1 V) chosen for recording the spectra shown in Fig. 4-3-4. This way, only defects in a depth between about 5 µm and 33 µm from the p^+ contact are detected. In this region the O_{2i} concentration in the EPI-ST material is expected to be very small since the oxygen concentration is low. But near to the interface between the epi-layer and the Cz substrate the oxygen concentration is much higher (see Fig. 4-3-2). Therefore, it is expected that the O_{2i} concentration in this region is also higher compared to the front region and the IO_{2i} should become visible. In fact, this is demonstrated in Fig. 4-3-5 where the spectrum of the EPI-ST diode shown in Fig. 4-3-4 (front region) is compared with a spectrum recorded under filling conditions which corresponds to a depletion region near to the interface. It is also obvious that in this region with its high oxygen concentration the C_i defect is not visible anymore pointing to the argument given above for the absence of a C_i signal in EPI-DO. In order to get more insight into the formation of the IO_{2i} and its dependence on the oxygen concentration, depth profiles were measured not only for the EPI-ST material but also for the EPI-DO and the MCz material which exhibit an almost homogenous oxygen distribution throughout the bulk.

Before presenting the measured IO_{2i} depth profiles it is noted that the DLTS spectrum of a MCz diode after irradiation with 26 MeV protons is very similar to that recorded for the EPI-DO sample (see Fig. 4-3-6). Especially a clear IO_{2i} signal is seen and no C_i signal. In Fig. 4-3-6 a spectrum before irradiation is included which shows two small peaks located at about 112 K and 62 K. While the 112 K peak cannot be attributed to a known defect, the signal at 62 K is most likely related to a thermal double donor TDD. This assignment is based on a direct capture cross section measurement resulting in a very large value of $\sigma_n = 1\cdot10^{-12}$ cm^2 which is expected for a shallow double donor.

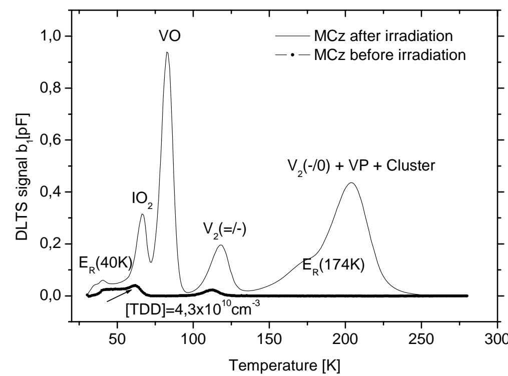

Fig. 4-3-6 DLTS spectra for MCz material before and after irradiation with 26 MeV protons with a fluence $\Phi_{eq} = 4.6 \cdot 10^{11}$ cm^{-2}. U_R = -20 *V* , U_P = -5 *V* ,t_p=100 *ms*, T_W = 200 *ms*.

The IO_{2i} depth profiles were extracted from transient measurements, recorded at a constant temperature of 67 K, varying the reverse bias and the pulse bias accordingly and using a time window T_W of 200 ms. In Fig. 4-3-7 the depth profiles of the IO_{2i} concentration are plotted for all three materials. As expected, the profiles of the MCz and the EPI-DO material are nearly flat in the measured region while the profile of the IO_{2i} center of the EPI-ST material reflects the non-homogeneity of the oxygen profile as measured by SIMS.

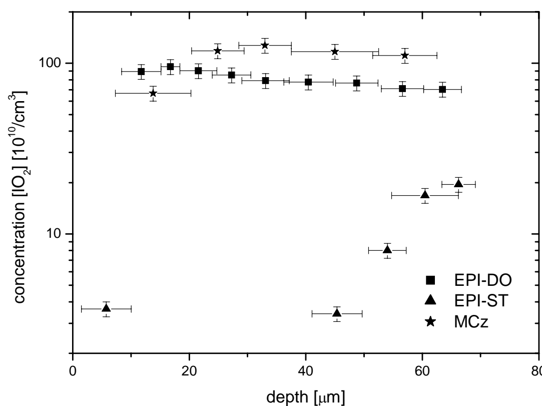

Fig. 4-3-7 Depth profiles of the IO_{2i} defect concentration in EPI-ST, EPI-DO and MCz after irradiation with 26 MeV protons with fluences of $\Phi_{eq} = 8.1\cdot10^{11}$ cm^{-2}, $\Phi_{eq} = 4.8\cdot10^{11}$ cm^{-2} and $\Phi_{eq} = 4.6\cdot10^{11}$ cm^{-2} accordingly. All concentrations are scaled to $\Phi_{eq} = 8.1\cdot10^{11}$ cm^{-2}.

This correlation between the respective IO_{2i} and O_i concentration has led to the question whether the measured IO_{2i} concentration can be taken as a relative measure of the oxygen-dimer concentration itself in this material. If we assume that the formation of IO_{2i} via I +

$O_{2i} \rightarrow IO_{2i}$ is not disturbed by the competing reaction $I + C_s \rightarrow Si_s + C_i$ or other interstitial related defect reactions like the formation of I_2O_{2i} [4] the IO_{2i} concentration should reflect the oxygen-dimer content in the material.

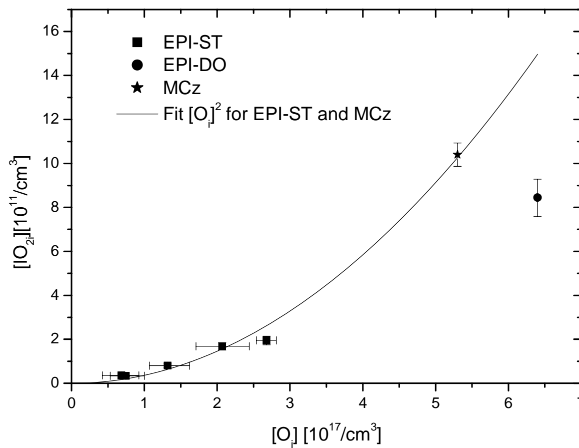

Fig. 4-3-8 Concentration of the IO_{2i} defect in EPI-ST, EPI-DO and MCz detectors as function of the oxygen concentration. The solid line represents a fit with a quadratic function.

IR absorption measurements by L.I. Murin et al. [7] showed a quadratic dependence of the oxygen dimer concentration on the O_i content in oxygen rich Cz silicon. In Fig. 4-3-8 the IO_{2i} concentration for all measured samples (EPI-ST, EPI-DO, MCz) is plotted as function of the oxygen concentration, showing an almost ideal quadratic dependence as suggested by the Murin result [7]. However this curve does not reproduce the value observed for EPI-DO, which is only about 50% of the expected concentration. This finding is so far not understood.

In addition to the non-homogeneous IO_{2i} depth profile we found also a strong variation of the C_i concentration as function of the depleted depth in the EPI-ST material, as demonstrated in Fig. 4-3-9. The $[C_i]$ profile has a maximum at a depth where the oxygen concentration has its minimum. Towards the regions with a higher oxygen concentration $[C_i]$ drops down rapidly. This rapid decrease is due to the high capture rate of C_i by O_i forming the C_iO_i complex, when the O_i concentration is sufficiently large. The competing reaction $C_i + C_s \rightarrow C_iC_s$ plays a minor role, since the concentration of C_s is much smaller than the oxygen concentration as mentioned before. It should also be reminded that the C_i is mobile at room temperature (RT) and cannot be detected anymore, if the sample is stored for a prolonged period at RT (the annealing time constant at RT is about 4 days for carbon and oxygen lean material).

In conclusion, the IO_{2i} defect complex can be regarded as a very sensitive indicator for the presence of O_{2i} in silicon and under some prerequisites its concentration may be taken as a relative measure for the O_{2i} concentration in the material. The importance of O_{2i} for the radiation tolerance of silicon detectors had been outlined in several papers and reports [1, 2, 8, 9]

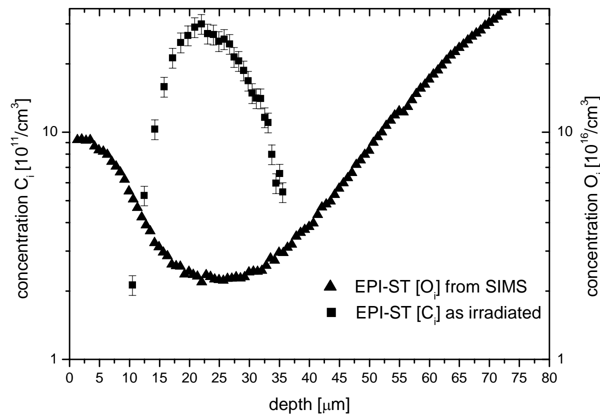

Fig. 4-3-9. Depth profile of the C_i concentration in a EPI-ST detector irradiated with 26 MeV protons with a fluence of $\Phi_{eq} = 8.1 \cdot 10^{11}$ cm^{-2} and correlated with the oxygen concentration.

4.4 Defect engineering by pre-irradiation treatments

In the frame of the RD50 research project, the INFN in Padova, the Institute of Nuclear Research (KINR) in Kiev, ITC IRST in Trento and CNM in Barcelona have investigated radiation hardening by preliminary neutron irradiation of silicon, which is expected to create gettering sites in the silicon bulk. Preliminary irradiation of silicon by fast neutrons and the subsequent annealing lead to the formation of sinks for primary radiation defects. These sinks are complexes of radiation-induced defects with neutral impurities, such as C and O, always present in the silicon wafers. The optimal value of annealing temperature was found experimentally (see Ref. [10]). It was shown that after pre-irradiation and annealing procedures the changes in the electrical characteristics with respect to un-irradiated samples are negligibly small.

The investigated materials are summarized in the following Table 4-4-1:

Producer	Type	ρ [kΩ·cm]	τ [μs]	d [μm]	Processing
N-type silicon:					
TOPSIL	FZ	~ 43 ~ 46 after pre-irrad.	~ 1000	310	ITC IRST
TOPSIL	FZ NTD	3	~ 600	280	ITC IRST
P-type silicon:					
Ukrainian prov.	FZ	~ 10 ~ 10 after pre-irrad.	~ 1000	290, 360, 480	CNM

In addition p-type standard FZ and DOFZ diodes with a resitivity of about 25 kΩ·cm as well as p-type MCz diodes with a resitivity of about 10 kΩ·cm had been provided by CNM.

The irradiation of the different devices were performed at the research reactor of the Jozef Stefan Institute in Ljubljana. In Fig. 4-4-1 the development of the effective doping concentration as function of fluence is shown for the different n-type materials and in Fig. 4-4-2 for the different p-type materials, respectively. The extracted β-values are listed in Table 4-4-2:

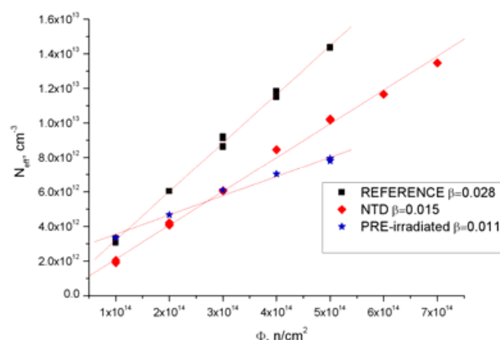

Fig. 4-4-1 Effective doping concentration as function of fluence for the n-type reference, NTD and pre-irradiated devices. The lines are linear fits of the experimental data.

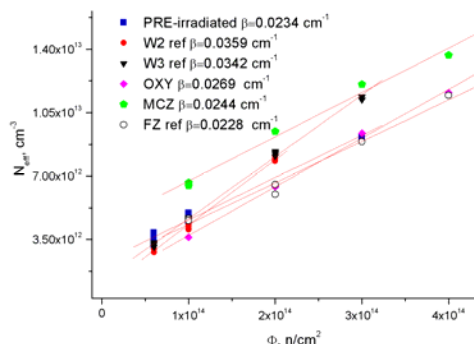

Fig. 4-4-2 Effective doping concentration as function of fluence for the different p-type devices. The lines are linear fits of the experimental data.

N-type, β-values in cm^{-1}

Reference	NTD	Pre-irradiated
0.028	0.015	0.011

P-type, β-values in cm^{-1}

Reference W2	Reference W3	Pre-irradiated	MCz	DOFZ	FZ
0.036	0.034	0.023	0.024	0.027	0.023

The reverse current per unit volume as function of fluence is plotted in Fig. 4-4-3 for the n-type diodes and in Fig. 4-4-4 for the p-type ones. All values are taken after irradiation without any annealing.

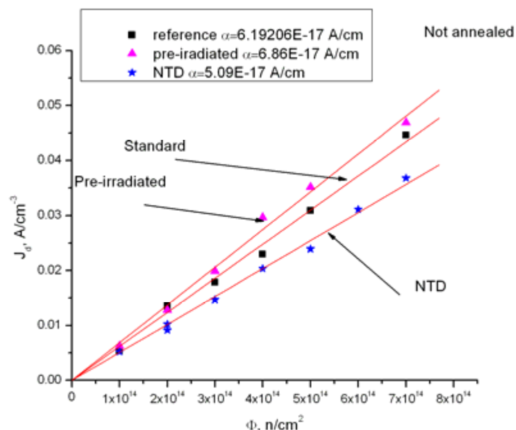

Fig. 4-4-3 Reverse current per unit volume as function of fluence for the n-type diodes.

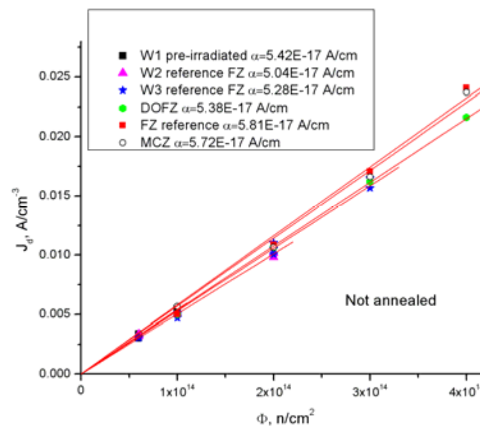

Fig. 4-4-4 Reverse current per unit volume as function of fluence for the p-type diodes.

The variation of the corresponding α-values is sufficiently larger for the n-type diodes than those observed for the p-type ones. This might be due to some differences in the irradiation history or storage conditions after irradiation. Annealing experiments would clarify whether there are real differences or not.

4.5 References of Chapter 4

[1] G. Lindström, I. Dolenc, E. Fretwurst, F. Hönniger, G. Kramberger et al., Nucl. Instr. and Meth. A 568 (2006) 66-71

[2] I. Pintilie, M. Buda, E. Fretwurst, G. Lindström, J. Stahl, Nucl. Instr. and Meth. A 556 (2006) 197-208

[3] A. Barcz, SIMS laboratory, Physics Institute of the Polish Academy of Science, Warsaw, Poland

[4] J.L Lindström, T. Hallberg, J. Herrmansson, L.I. Murin, B.A. Komarov et al., Physica B 3008-310 (2001) 284-289

[5] I. Pintilie, E. Fretwurst, G. Lindström, J. Stahl, Nucl. Instr. and Meth. A 514 (2003) 18-24

[6] M. Kuhnke, PhD thesis, University of Hamburg, DESY-THESIS-2001-009

[7] L.I. Murin, T. Hallberg, V.P. Markevich and J.L. Lindström, Phys.Rev.Letters Vol. 80 Number 1 (1998) 93-96

[8] RD50 Status Report CERN-LHCC-2004-031 and LHCC-RD-005

[9] V. Boisvert, J.L. Lindström, M. Moll, L.I. Murin, I. Pintilie, Nucl. Instr. and Meth. A 552 (2005) 49-55

[10] P.G. Litovchenko, D. Bisello, A. Candelori, A.P. Litovchenko, A.A. Groza, et al., Radiation hardening of silicon for detectors by preliminary irradiation, Solid State Phen., vol.95-96 (2004), pp. 399-404

5 Pad Detector Characterization (PDC)

The research of the PDC research line in 2006 has been focused to oxygen rich materials, which are most likely candidates for the SLHC tracker material. The damage at SLHC will be dominated by fast charged hadrons for $r<20$ cm and neutrons of similar spectra as reactor neutrons at $r>20$ cm [1]. The limited access to CERN-PS in the last year resulted in more irradiations performed with reactor neutrons at research reactor of Jožef Stefan Institute in Ljubljana and low energy protons (26 MeV) at the cyclotron of the Forschungszentrum in Karlsruhe. The two most studied materials were MCz and epitaxial silicon detectors, but also p-type FZ detectors were considered. The properties of investigated materials are gathered in the Table 5-1. The detectors were produced by IRST, CiS and CNM Barcelona within RD50 collaboration.

Table 5-1. Properties of investigated materials.

Material type:	MCz, FZ	Epi-Si
Producer:	Okmetic Ltd (Vantaa, Finland)	ITME (Warsaw, Poland)
Details:	n type (0.5-6 kΩcm), 300 μm thick p type (1.8kΩcm), 300 μm thick	n type (150 Ωcm, 75 μm thick) n type DO (150 Ωcm, 75 μm thick) n type (500 Ωcm, 150 μm thick)

The SMART collaboration produced the largest number of the samples this year. The uniform p-spray technique has been used to increase n^+ implants isolation with two different implantation doses, namely $3\cdot10^{12}$ cm^{-2} (low p-spray) or $5\cdot10^{12}$ cm^{-2} (high p-spray) for n^+-p detectors. The processing of n- and p-type MCz silicon detectors was carefully modified to avoid the thermal steps at temperatures between 400 and 600^{0}C in order to minimize the activation of Thermal Donors [2].

5.1 Electric field profile

The electric field profile in irradiated silicon detectors is different from the linear one typical for homogeneous effective doping concentration (N_{eff}=const.) [3]. How much the electric field differs from the linear depends on type of irradiations, material and time after the irradiations [4]. The non-uniform effective doping concentration changes also the interpretation of the results and damage modeling (e.g. Hamburg model [5]), so it is a necessity to understand it. The shape of the electric field is important particularly in the range of the fluences around 10^{15} cm^{-2} where the bias voltages are around the full depletion voltage [6,7]. At smaller fluences detectors are likely to be over-depleted and at higher the trapping of the drifting charge renders the electric field at the non-collecting electrodes unimportant. The simplest model of electric field profile which explains so called “double peak” (DP) observed in the TCT measurements is proposed in [3]. The origin of the DP is explained by trapping of equilibrium carriers on the mid-gap energy levels of radiation induced defects, which leads to a non-uniform distribution of space charge concentration $N_{eff}(x)$ with positively and negatively charged regions adjacent to the p^+ and n^+ contacts, respectively (Fig. 5-1).

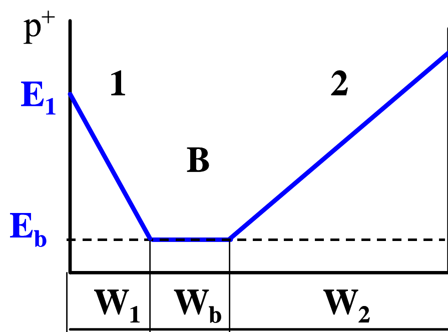

Fig. 5-1. Structure of a heavily irradiated Si detector with a consideration of the electric field in the base region.

The DP model considers two space charge regions and the non-depleted base region *in-between.* Due to the high resistivity of the non-depleted bulk a non-negligible electric field is also present [8] allowing the drift of the carriers through it. The model describes the data (TCT and pixel test beam measurements [9]) well already when assuming two radiation induced defects with mid-gap energy levels. These levels are deep donors (DD) and deep acceptors (DA) with the activation energies of E_v + 0.48 eV and E_c – 0.52 eV, respectively [3,8]. This allows the simulation of $N_{eff}(x)$ and $E(x)$ distributions. The main variable parameter that controls the $N_{eff}(x)$ and $E(x)$ profiles is the ratio of the concentration $k = N_{DA}/N_{DD}$.

The measurements of the induced current pulses are performed using the Transient Current Technique (TCT) [10]. In TCT measurements, a laser with a wavelength of 670-870 nm was used for non-equilibrium carrier generation. The measurements were done with a laser illuminating the p^+ side of the detector. In this case the current pulse response results from electron drift which transverse the detector bulk and change the drift velocity in accordance with the electric field profile. To determine the parameters of the model the measured induced current pulses were fit with the corresponding equation $i(t) = Q_o\mu(E)\, E\,/d\, \exp(-t/\tau_{eff})$ where τ_{eff} is the effective trapping times of the injected carriers, μ the mobility, d thickness and Q_0 number of injected carriers (used for normalization). The extracted electric field is then verified by simulation of the induced current pulse and is used to determine the parameters that allow the calculation of $N_{eff}(x)$ and $E(x)$. An example of such reconstruction is shown in Fig. 5-2.

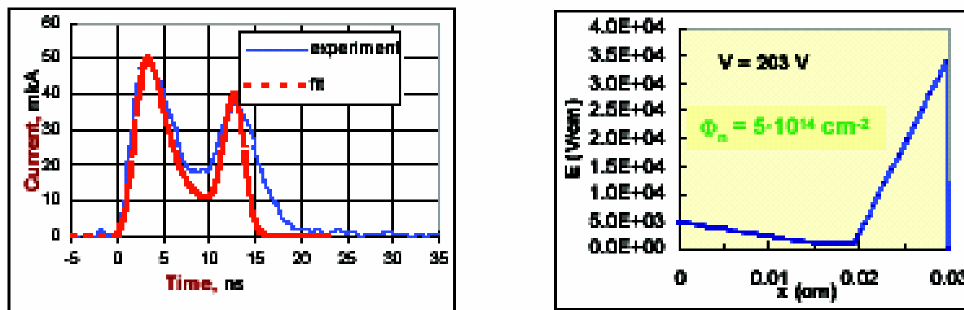

Figure 5-2: Measured TCT response after electron injection and calculated signal using the extracted electric field profile (Left). The reconstructed electric field profile (Right) in a MCz-n diode produced by SMART collaboration irradiated with neutrons to the fluence of $5{\cdot}10^{14}$ 1MeV n/cm^2. Measurements are performed at V_{fd}=203V.

As an example, successive changes of the reconstructed $E(x)$ profile in SMART detector from n-type MCZ Si irradiated by $5{\cdot}10^{14}$ n/cm^2 and operated in the range 184 V to 402 V are shown in Fig. 5-3.

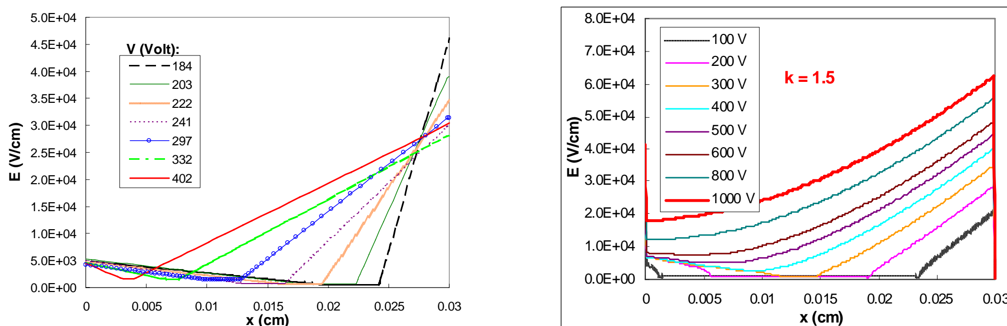

Figure 5-3: Extracted electric field profiles for n-type MCZ Si detector irradiated by a fluence of $5{\cdot}10^{14}$ n_{eq}/cm^2 (left) and simulations of electric field distributions with a consideration of carrier trapping at k=1.5 (right).

The changes correlate well to the simulation of electric field. The electric field near the p^+ contact (in region 1) is practically constant. The increase of the bias affects mainly $E(x)$ distribution in the

region 2 extending from the n^+ contact. At high voltages the main junction (i.e. the junction with a larger electric field amplitude and width) is near the n^+ contact. Starting from 400 V, negatively charged space charge region 2 extends over the entire detector thickness. Thus, SCSI occurs in MCz Si neutron irradiated detector, however at higher fluences than in FZ Si detector. The discrepancy with simulated profiles is that the electric field near the n^+ contact decreases with respect of increasing voltage.

In contrast to neutron irradiated detector the proton irradiated detector show the larger electric field at the p^+ contact as can be seen in Fig. 5-4. The agreement of simulated and electric field extracted from measurements is achieved for k=0.5. The parameters of the model extracted from measurements and used in simulations are gathered in Table 5-2.

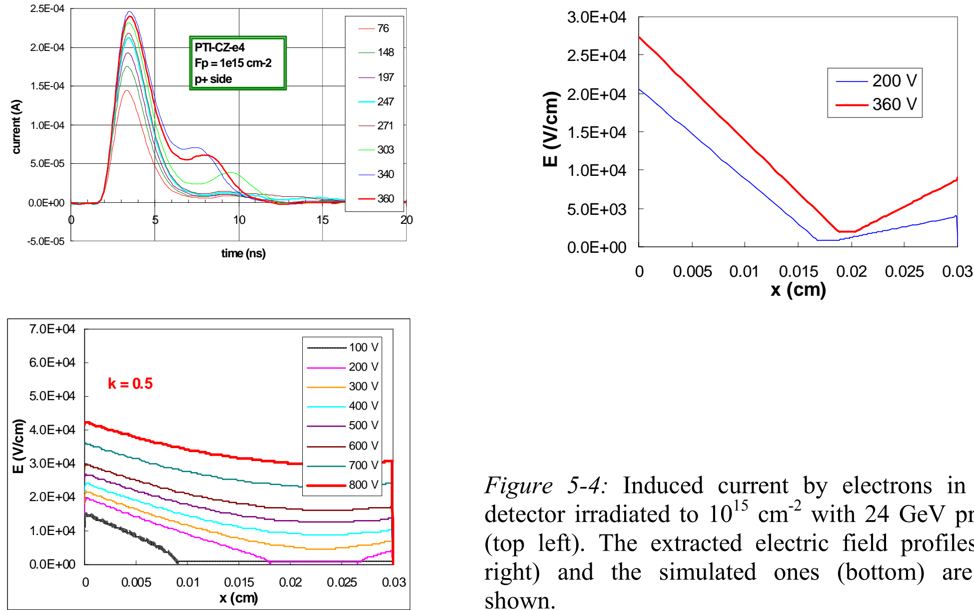

Figure 5-4: Induced current by electrons in MCz detector irradiated to 10^{15} cm^{-2} with 24 GeV protons (top left). The extracted electric field profiles (top right) and the simulated ones (bottom) are also shown.

Table 5-2 Parameters derived by adjustment of simulated E(x) profile to the profile reconstructed from current pulse response

	Neutrons	Protons
m_j (cm^{-1})	0.7	0.7
$k = N_{DA}/N_{DD}$	1.35	0.45
N_{DA} (cm^{-3})	$6.75{\cdot}10^{14}$	$3{\cdot}10^{14}$
N_{DD} (cm^{-3})	$5{\cdot}10^{14}$	$6.6{\cdot}10^{14}$

m_j - introduction rate of generation centers

Although in irradiated silicon detectors the shape of electric field is complex in most cases one of the junctions dominates. The dominating junction defines the sign of the space charge. The calculation of N_{eff} in the dominating junction in the form of V_{fd} is also approximately correct, which explains why the damage models still work well even if based on the assumption N_{eff}=const.

5.2 Studies of effective doping concentration in different materials

The evolution of effective doping concentration after irradiation can be described by three terms ("Hamburg model" [5]): the decay of effective acceptors immediately after irradiation ("beneficial annealing"), stable part and creation of the effective acceptors at late annealing stages ("reverse annealing"). The stable part in FZ silicon which was the only detector grade material up to recently was always of negative sign [11]. As the reverse annealing and stable damage represent the introduction of effective acceptors the increase of $|N_{eff}|$ and consequently V_{fd}, were kept as low as possible by keeping the detectors cold for most of the time. The RD48 collaboration has proven the

positive role of oxygen for detectors irradiated with fast charged hadrons [11]. The introduction rate of stable acceptors was reduced by around factor of 3 when compared to STFZ detectors. In addition it was shown that reverse annealing time constants are prolonged for high [O].

The oxygen concentration in DOFZ is around $2\mathrm{x}10^{17}$ cm^{-3}, which is an order of magnitude lower than the [O] in MCz/Cz materials [12,13]. The latter materials don't undergo SCSI ("movement of the main junction") after irradiation with 24 GeV/c protons [12,13]. The N_{eff} of MCz-n or Cz-n type detectors first decreases, due to initial donor removal, and than starts to rise as the stable donors are introduced (see Fig. 5-5). The positive sign of the space charge was confirmed by TCT (see previous section) and also by the evolution of N_{eff} during long term annealing (see Fig. 5-6). The $|N_{eff}|$ increases during beneficial annealing and then decreases reaching the minimum. After that detectors undergo SCSI which is followed by further increase of $|N_{eff}|$ with time. However, this happens at much prolonged times which are comparable or even exceeding those of detectors being at room temperature during the entire SLHC beam-off period.

A natural assumption would be that also MCz-p type detectors beyond certain fluence become n-type after the initial shallow acceptors are compensated by radiation induced stable donors. However, MCz-p type detectors after initial decrease remain p-type at all fluences. The $[O_{2i}]$ and $[O_i]$ are the same as in MCz-n and there is no explanation so far in what way shallow acceptors could influence the formation of bistable donors. It is remarkable that after the end of beneficial annealing $|g_{eff}|=0.007$ cm^{-1} ($|N_{eff}|=g_{eff}*\Phi_{eq}$) is approximately the same for all materials.

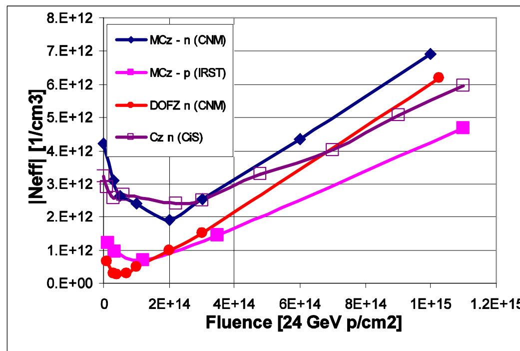

Figure 5-5: The dependence of $|N_{eff}|$ on fluence for different oxygen rich materials [14-16] after completed beneficial annealing. The processing company is given in the brackets.

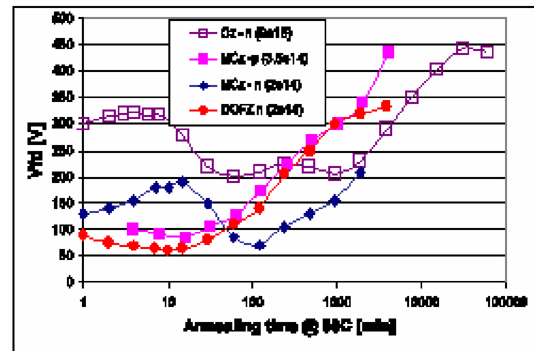

Figure 5-6: The evolution of full depletion voltage with time for the same materials as in Fig. 5-5.

The epitaxial silicon detectors have much lower [O] concentration of order 10^{17} cm^{-3} [17] than MCz/Cz, but positive stable donors are introduced nevertheless (see Fig. 5-7). The introduction of shallow donors is assumed to be related to the $[O_{2i}]$, which is assumed to be the precursor [18,19]. The fraction $[O_{2i}]/[O]$ in epi-Si detectors is much larger than in MCz [20]. The most probable reason is out-diffusion of O_{2i} from Cz substrate to epitaxial Si during the thermal treatments involved in device processing. That also explains different introduction rate of bistable donors for different detector thicknesses as can be seen in Fig. 5-7 [17,21].

After neutron irradiation Cz/MCz-n,p , DOFZ–p,n and STFZ-p,n exhibit similar dependence of $|N_{eff}|$ on the fluence as can be seen in Fig. 8 [22–24]. The stable acceptors are generated with introduction rate $g_c \sim 2$ cm^{-1}, also found in STFZ [11]. The difference between different detectors in the Fig. 8 is due to the different initial doping concentration and the doping type (MCz-n undergo SCSI at around 10^{14} cm^{-2}). On the other hand the epi-Si detectors exhibit the smallest stable damage after neutron irradiations (see Fig. 5-9). It seems that for low resistivity (50 Ωcm) detectors the stable donors are generated and for higher resistivities the acceptors. Again, it is not clear how the shallow dopants can influence formation of bistable donors. It is however interesting that stable donors or acceptors are generated at about the same rate $g_{eff} \sim 5 \cdot 10^{-3}$ cm^{-2} [21,23,25,27], which is nevertheless three times smaller than in any other material.

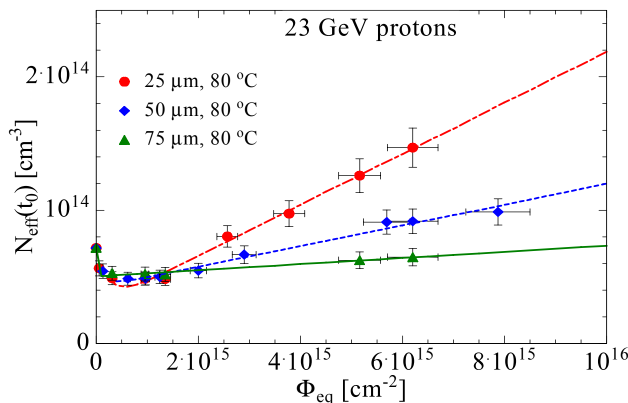

Figure 5-7: The dependence of N_{eff} after the end of beneficial annealing (t_0) for epitaxial silicon detectors of different thicknesses.

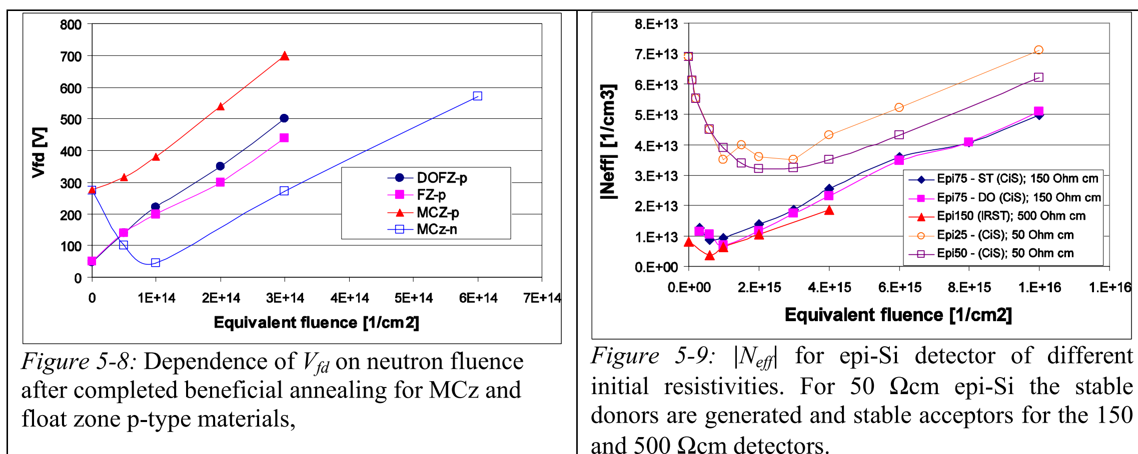

Figure 5-8: Dependence of V_{fd} on neutron fluence after completed beneficial annealing for MCz and float zone p-type materials,

Figure 5-9: $|N_{eff}|$ for epi-Si detector of different initial resistivities. For 50 Ωcm epi-Si the stable donors are generated and stable acceptors for the 150 and 500 Ωcm detectors.

The reason for different behavior of detectors with high [O] after neutron and fast charged hadron irradiation is due to different fraction of point defects/clusters for the same NIEL [11]. The 24 GeV protons create more point defects than the neutrons where the damage is dominated by the cluster formation [26]. As the damage is independent on the bulk material for neutron irradiated detectors, the formation of bistable donors should be related to point defects. The fraction of NIEL going to formation of point defects is even larger for low energy protons (around 20 MeV) [26], hence the formation of bistable donors and suppressing of deep acceptors was expected to be even larger than for 24 GeV/c protons. These reasoning was confirmed by ^{60}Co irradiation where only point defects are created and the positive space charge is introduced also for DOFZ and not only for MCz/Cz materials.

The MCz detectors irradiated with 26 MeV protons show contrary to expectation SCSI after few 10^{14} cm^{-2} as shown in Figs. 5-10,11. The main junction moved from p^+ to the n^+ [28]. The dependence of long term annealing of N_{eff} confirms that conclusion (see Fig. 5-12). Unlike the MCz material the epi-Si detectors don't undergo SCSI after irradiation as can be seen in Fig. 5-13 [29]. The SCSI however occurs during long term annealing at around 50 min at 80°C, which was confirmed also with TCT measurements.

In the first approximation the short term and long term annealing on the time scales of interest for SLHC is independent on the material [11,14-17,21]. The acceptor activation is governed by the first order process with the introduction rate g_Y varying between 2.6 and 4.8 cm^{-1} and the time constant of around 100 min at 80°C, depending on [O]. Significantly lower $g_Y = 1.6\cdot10^{-2}$ cm^{-1} was observed only in neutron irradiated epi-Si detectors [21]. In epi-Si detectors at much longer times of few 1000 min at 80C (not so relevant for SLHC) more acceptors are created with a second order process [17].

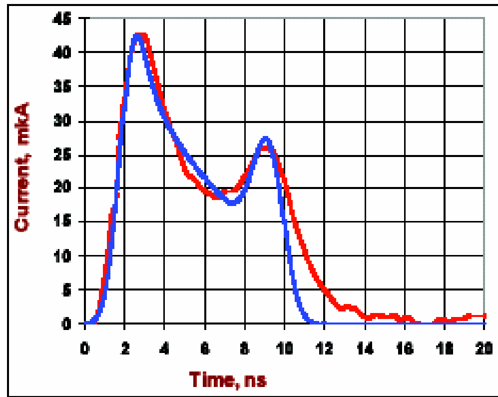

Figure 5-10: Induced current by electrons (red) in n-type MCz diode irradiated with 26 MeV protons at a fluence of $4.1 \cdot 10^{14}$ 1MeV n/cm^2 and bias voltage 180V. The experimental data fit is superimposed on the measurements**.**

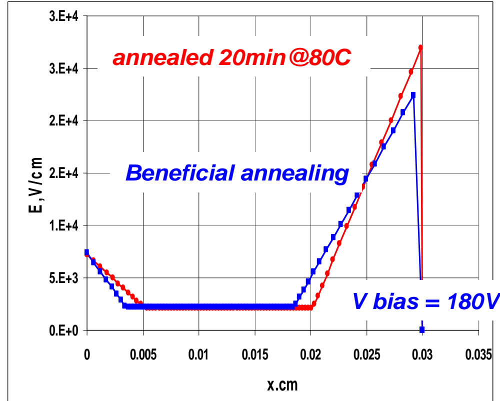

Figure 5-11: Electric field extracted at different annealing times for the sample in the Fig. 10. The blue line corresponds to a sample that has undergone an annealing time of 8 min at 80°C and the red line to a sample after an annealing of 20 min at 80°C.

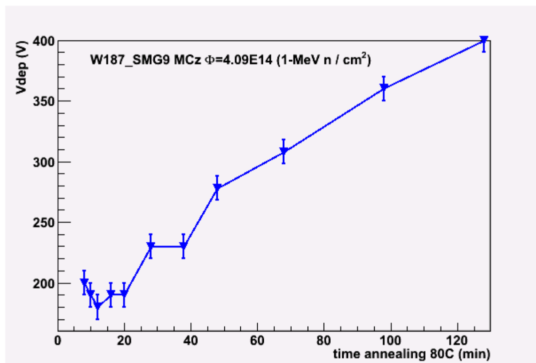

Figure 5-12: Dependence of V_{fd} on annealing time for n-type MCz diode (same samples shown in Figs. 10,11) irradiated with 26 MeV protons to a fluence of $4.1 \cdot 10^{14}$ 1MeV n/cm^2. The annealing temperature is 80°C

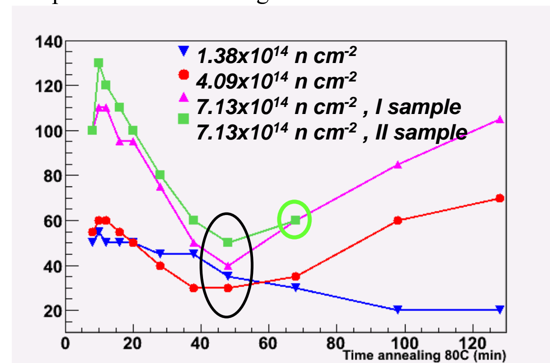

Figure 5-13: Dependence of V_{fd} on annealing time for 150 µm thick epitaxial diodes irradiated with 26 MeV protons. For the diodes in the fluence range 4.1-$7.1 \cdot 10^{14}$ 1MeV n/cm2 a type-inversion takes place around an annealing time of 50 minutes at 80°C.

The key parameters governing the radiation tolerance for different materials are gathered in the Table 5-3. The opposite sign of g_{eff} and g_y can be exploited for compensation of the space charge. In case of properly chosen scenario the V_{fd} of such detectors can controlled and detectors of few hundred microns could be depleted at fluences well above 10^{15} cm^{-2}.

	g_{eff}, g_c, β_{eq} [10^{-3} cm^{-1}]	g_Y [10^{-3} cm^{-1}]	τ_{ra} [min at 80°C]
DOFZ-n [11]	~6	50 (a)	~200
STFZ-n,p [11,16]	~20 (b)	45 to 65	>80
MCz-n [2,16,30,33]	-4 to -6.5	28 to 45	80 to 200
MCz-p [15,30]	~7	~28	100 to 500 (d)
Cz-n [14]	~-5	~30	~80
Epi-n [17,32]	-3 to -10 (c)	~30	~130

Table 5-2: Survey of damage parameters in different silicon materials after irradiation with 24 GeV/c protons. (a) g_Y tends to saturate for DOFZ-n material at high fluences and may do so also in MCz. (b) The β_{eq} for STFZ-p type measured by [16] was found around 5 times lower than expected. Large variations between different STFZ materials were observed in the past also for STFZ-n type. (c) The introduction rate depends on thickness of the detector. Smaller absolute values are for thicker detectors. (d) The huge difference in time constant reported in [15] is assumed to be related to thermal donors.

5.3 Bias effect

The damage in silicon detectors depends on the applied bias during the irradiation[34-36]. It anneals out after the bias is switched off for few days at 20°C [35,36]. After the bias is switched on again, part of the damage reappears. This is called the bistable damage and was observed in STFZ detectors. It was assumed that effective acceptors get activated after the bias is applied. The recent measurements performed on MCz and epi-Si detectors revealed that, contrary to expectation, V_{fd} and by that $|N_{eff}|$ always increase after applying the bias regardless on space charge sign. In n-type material that doesn't undergo SCSI the effective donors are activated [37].

For example the increase of V_{fd} , due to applied bias, is shown in Fig. 5-14 for MCz-n type detector irradiated with 24 GeV protons. An additional increase of $|N_{eff}|$ and consequently V_{fd} can be calculated as $|\Delta N_{eff}|=g\ \Phi$ with g~0.004 cm^{-1} and seem to be independent on irradiation particle type and material [37]. After the bias is switched off the V_{fd} decreases to the level before the bias was switched on. The time constant of "activation" and "deactivation" of damage is around a few hours at T=20°C.

To verify that the effect is present also in charge collection measurements the signals of minimum ionizing electrons from ^{90}Sr source were recorded for the same sample as shown in Fig.5-14. As can be seen in Fig. 5-15 the increase of voltage needed for efficient operation after 140 h with bias applied is clearly seen and coincides with the difference in V_{fd} as measured with C-V. The diode was kept under bias larger than V_{fd} at T=20°C and measurements were than at T=-10°C.

Since g is approximately equal to stable damage the effect can be very important. It is still an open questing what the activation times are at temperatures around -10°C. Only after these measurements it will be possible to predict the impact of the bias effect on detector operation at LHC. The leakage current is not affected by the applied bias as was already seen in STFZ material.

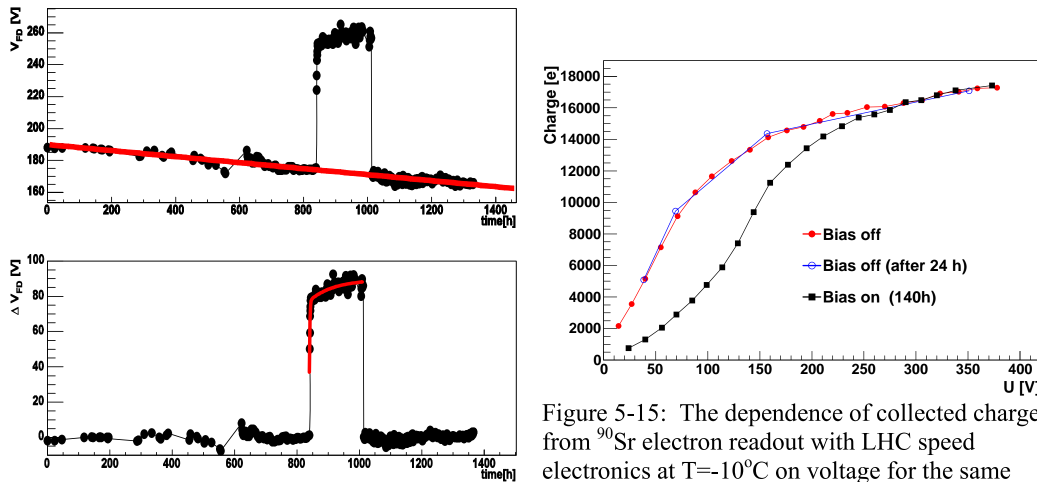

Figure 5-14: The evolution of V_{fd} with time before the bias was applied, during the applied bias of 300 V and after it was switched off for an MCz-n type detector irradiated with protons to $5\cdot10^{14}$ cm^{-2}. In the bottom plot the reverse annealing was subtracted.

Figure 5-15: The dependence of collected charge from ^{90}Sr electron readout with LHC speed electronics at T=-10°C on voltage for the same detector as in Fig. 14. The Q/V plot before the bias was switched on is denoted by red and after 140 h with bias on by black. The reproducibility was checked before switching the bias on and is in blue.

5.4 Leakage current measurements

The current damage parameter α has been measured for the epitaxial and the MCz samples irradiated with neutrons, 24 GeV/c and 26 MeV protons. It was confirmed that leakage current damage constant α(t) is independent on material [2,23,24,27,28-33] and irradiation particles. It has been shown in [6,7] that for 24 GeV protons and neutrons α is the same in epi-Si, MCz, Cz as in FZ material. This holds also for 26 MeV protons as shown in Fig. 5-16a. The only deviation from the expectations was observed in thin low resistivity (50 Ωcm) epi-Si detectors irradiated with neutrons [27,38,39] . There the saturation tendency for α was observed at very high fluences (see Fig. 5-16b).

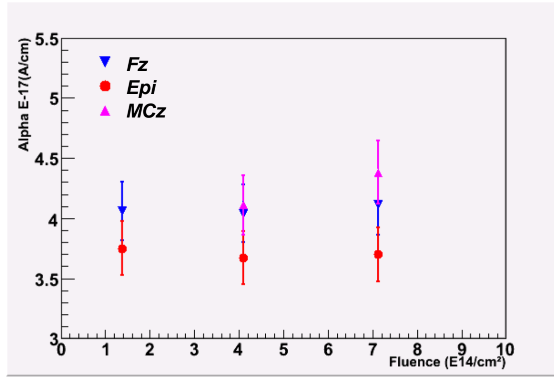

Figure 5-16a: Leakage current damage constant for Fz, MCz and epitaxial silicon samples as a function of the received fluence after an annealing time of 8 minutes at 80°C.

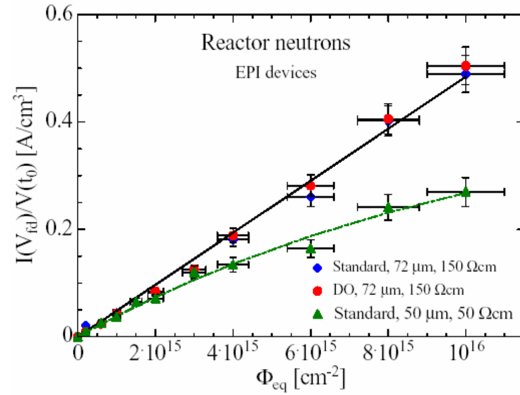

Figure 5-16b: The leakage current normalized to thickness at the end of beneficial annealing for different epi-Si detectors.

5.5 Effective trapping times

Trapping of the drifting charge in the irradiated silicon detectors represents the limiting factor for their efficient use at highest SLHC fluences. The effective trapping probabilities are calculated as $1/\tau_{effe,h} = \beta_{e,h}(t, T)\ \Phi_{eq}$, where $\beta_{e,h}$ depends on time after irradiation and measurement temperature [40]. Measurements of β in p-type silicon and for neutron irradiated silicon detectors were intensively studied this year. The measurement of effective trapping times in different p-type materials irradiated with neutrons is shown in Figs. 18,19 [22]. Although they agree with previous measurements (see Table 5-3) it seems that β decreases slightly with fluence. The measurements performed by Dortmund group on STFZ and DOFZ irradiated with neutrons (β_e=3.0·10^{-16} cm^2/ns and β_h=3.6·10^{-16} cm^2/ns at RT) [41] also agree within error margin with previous measurements.

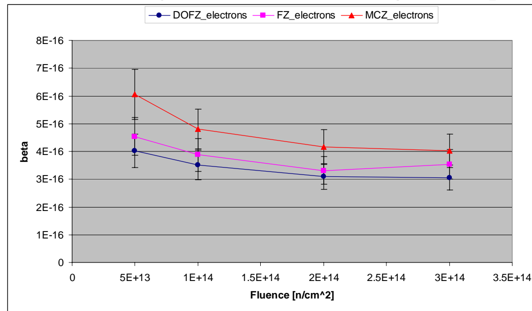

Figure 5-17: Trapping parameter β measured for electrons, measured at different fluences at T=20°C.

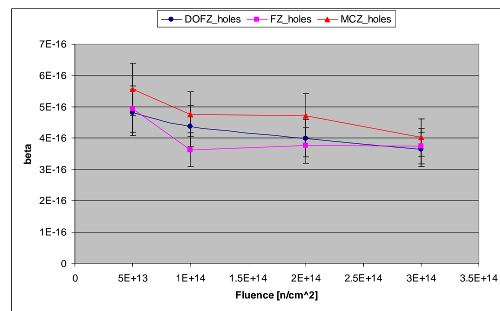

Figure 5-18: Trapping parameter β measured for holes, measured at different fluences at T=20°C.

The values of effective trapping times damage constant from different groups [14,31,22,40-42] are gathered in the Table 5-3. The effective trapping times within the error margins don't depend on resistivity, [O], [C], wafer production (Cz, FZ, epi-Si) and type of silicon (p or n).

t_{min} , T = -10°C	β_h [10^{-16}cm^{-2}/ns]	β_e [10^{-16}cm^{-2}/ns]
Reactor neutrons	5.7 ± 1	3.7 ± 0.6
fast charged hadrons	6.6 ±0.9	5.4 ± 0.4

Table 5-3: Trapping time damage constants for neutron and fast charged hadron irradiated silicon detectors.

The evolution of trapping probabilities with time after irradiation is described in the simplest model by the decay of the dominant trap to another dominant trap which is described by the following equation [40] $\beta = \beta_0 \exp(-\frac{t}{\tau_{ta}}) + \beta_\infty \left[1 - \exp(-\frac{t}{\tau_{ta}})\right] = (\beta_0 - \beta_\infty)\exp(-\frac{t}{\tau_{ta}}) + \beta_\infty$, with β_0 and β_∞

measured immediately after irradiation and at very long times respectively. For the annealing temperatures of interest the β_0 is very close to β measured at the end of beneficial annealing. The same equation is also valid for two traps model where one is constant in time and the other decays. An example of effective trapping times annealing for STFZ diodes irradiated within neutrons is shown in Fig. 5-19. [44]. The β_h increases with annealing time and β_e decreases with annealing time. Again, the same behavior was found also for other materials and irradiation particles [22,31,40,42,44]. The parameters describing annealing of effective trapping probabilities are gathered in the Table 3. The amplitude $(\beta_0-\beta_\infty)/\beta_0$ is an average from different groups [31,40,41,42,44]. Here it was assumed that the amplitude doesn't depend on the material, which is not clear yet.

Scaling of time constants to other annealing temperatures can be done by using the using Arrhenius relation ($\tau_{ta}=\tau0\cdot\exp(E_{ta}/k_BT)$). Although the time constant for reverse annealing of N_{eff} and τ_{ta} are comparable at T=60°C the difference in activation energy points to different underlying defects.

	τ_{ta} [min at 60°C]	$(\beta_0-\beta_\infty)/\beta_0$	E_{ta} [eV]
Electrons	650±250	0.35±0.15	1.06±0.1
Holes	530±250	-0.4±0.2	0.98±0.1

Table5- 4: Parameters used to model annealing of effective trapping times.

The annealing of $\beta_{e,h}$ is important for choosing optimum operation scenario for segmented detector operation. The charge collection of detectors with n$^+$ readout can in fact improve with time after irradiation. This has been confirmed for irradiated ATLAS pixel detectors in test beam [43].

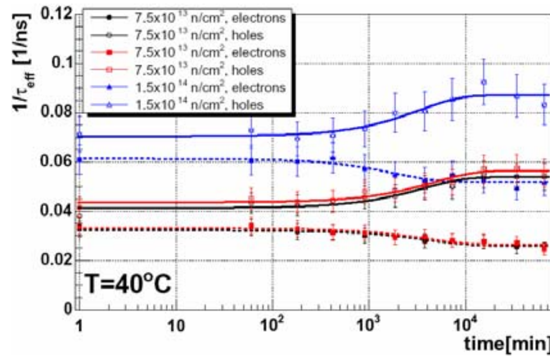

Figure 5-19: Dependence of effective trapping times of holes and electrons on accumulated time at 40°C after irradiation for STFZ 15 kΩcm detectors irradiated with neutrons.

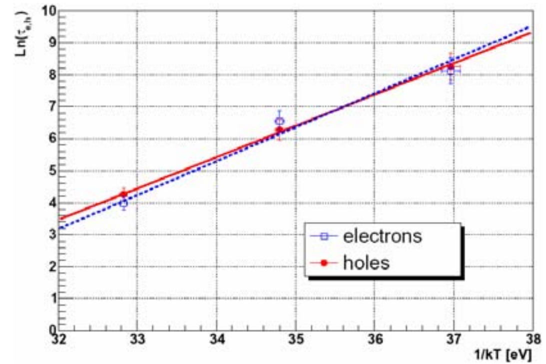

Figure 5-20: Arrhenius plot for annealing of the effective trapping times at different temperatures. The same detectors as in Fig. 5-19 were used.

The dependence of $\beta_{e,h}$ on temperature can be found in [31,40]. The trapping probabilities for both holes and electrons decrease with temperature.

5.6 Charge collection

The measurement of charge collection measurements were performed by using electrons from the ^{90}Sr source. The signal in 24 GeV/c proton irradiated MCz-p diodes is shown in Fig. 5-21. [15]. It is clear that for not fully depleted diodes (>1.1·10^{15} p cm^{-2}) the collected charge decreases dramatically. Around 15000 electrons were collected at 500 V at 1.1·10^{15} p cm^{-2}. Somewhat larger signals were obtained after 26 MeV proton irradiations with the similar setup as can be seen in Fig. 5-22. [45] The measurements of collected charge was performed also in heavily irradiated epitaxial silicon detectors (see Fig. 5-23), which could be fully depleted [25]. The dependence of collected charge on voltage shows that full depletion voltage determined by CV (denoted by a thick vertical line), is still a relevant parameter also at very high fluences. The voltage at which the collected charge starts to saturate coincides roughly with V_{fd}. At Φ_{eq}=8·10^{15} cm^{-2} the most probable signal of around 3200e was measured in 75 μm thick epi-Si detector. Approximately the same signal is expected also in thick detector as the $\tau_{eff,eh}\cdot v_{sat,e,h}$ = few 10 μm. The measured values are larger than predicted by the

simulation [46]. The reason is most likely in smaller trapping probabilities at such high fluences than extrapolated from measurements at $\Phi<10^{15}$ cm^{-2}. There are also some other measurements pointing to the same observation [47].

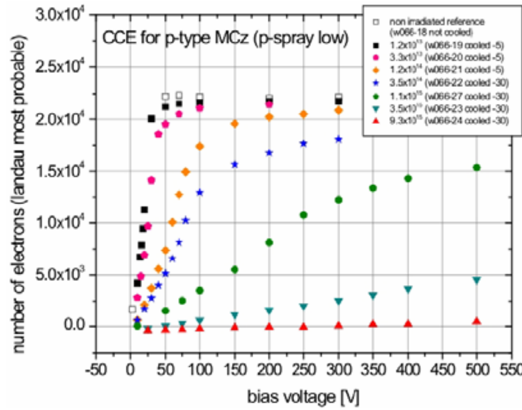

Figure 5-22: Measured signal in MCz-p type pad detectors irradiated with 24 GeV protons to 10^{16} p cm^{-2}. The measurements were performed at T=-30°C with 2 µs shaping electronics.

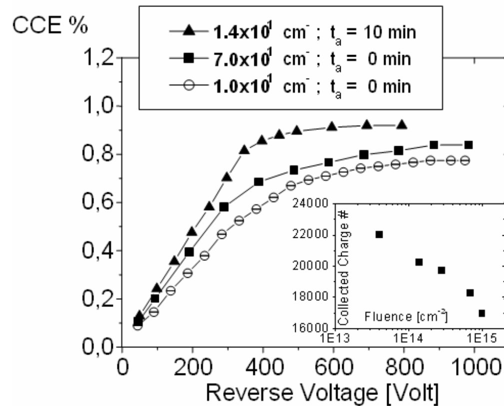

Figure 5-23: Charge collection vs. applied voltage of a set of p-type MCz Si diodes irradiated with 26MeV proton up to the fluence of 1.0×10^{15}cm^{-2} (1 MeV n equivalent) In the inset: maximum collected charge (measured in the range 600-900V) as a function of the fluence of irradiation. The measurements were performed at T=-30°C with 200 ns shaping electronics.

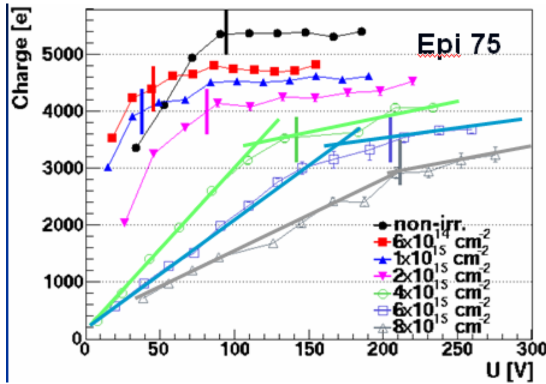

Figure 5-24: Dependence of collected charge on reverse voltage for a set of 75 µm epi-Si detectors irradiated up to $\Phi_{eq}=8\cdot10^{15}$ cm^{-2}. The intersection of the two lines fit to the measured points denote the V_{fd} as determined from charge collection measurements and the vertical bar the one from the CV.

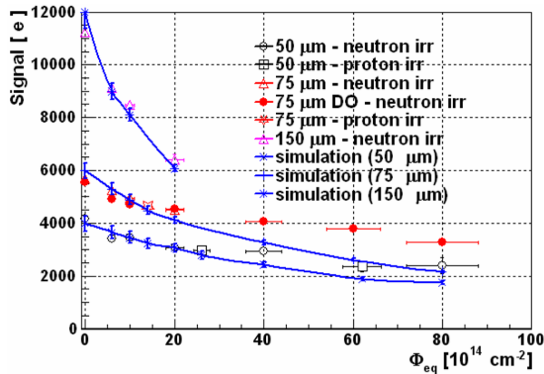

Figure 5-25: The collected charge (at bias voltage $>V_{fd}$) vs. Φ_{eq}, for a set of epi-Si detectors irradiated with 24 GeV protons and neutrons. The diodes were of different thicknesses. The simulated-predicted signals are also given for each thickness.

5.7 References for Chapter 5

[1] F. Gianotti et al., hep-ph/0204087, 2002.
[2] J. Harkönen et al., Nucl. Instr. and Meth. A552 (2005) 43.
[3] V. Eremin. E. Verbitskaya, Z. Li, Nucl. Instr. and Meth. A 476 (2002) 556-564.
[4] E. Verbitskaya et al., Concept of Double Peak electric field distribution in the development of radiation hard silicon detectors", presented at the 6th RESMDD conference, Florence 2006.
[5] M. Moll, Ph.D. Thesis, Hamburg University, 1999, DESY THESIS 1999-040, ISSN-1435-8085.
[6] CERN-LHCC-2004-031 and LHCC-RD-005, RD50 Status Report 2004.
[7] CERN-LHCC-2005-037 and LHCC-RD-009, RD50 Status Report 2005.
[8] E. Verbitskaya et al., Nucl. Instr. and Meth. A 557 (2006) 528-539.

[9] M. Swartz et al., Nucl. Instr. and Meth. A 565 (2006) 212.
[10] V. Eremin et al., Nucl. Instr. and Meth. A 372 (1996) 188.
[11] G. Lindström et al., Nucl. Instr. and Meth. A466 (2001) 308.
[12] CERN-LHCC-2004-031 and LHCC-RD-005, RD50 Status Report 2004.
[13] CERN-LHCC-2005-037 and LHCC-RD-009, RD50 Status Report 2005.
[14] E. Fretwurst et al., "Survey of radiation damage studies at Hamburg ", presented at 3*rd* CERN-RD50 Workshop, CERN, Geneve, 2004.
[15] H. Hödelmoser et al., "Charge collection efficiency of proton and neutron irradiated p-type MCz diodes", presented at the 6th RESMDD conference, Florence 2006.
[16] G. Pellegrini et al., Meth. Instr. and Meth. A552 (2005) 27.
[17] G. Lindstr¨om et al., Nucl. Instr. and Meth. A556 (2006) 451.
[18] E. Fretwurst et al., Nucl. Instr. and Meth. A514 (2003) 1.
[19] Y.J. Lee et al., Phys. Rev. B 65 (2002) 085205-1-12.
[20] I. Pintilie et al., Meth. Instr. and Meth. A556 (2006) 197.
[21] E. Fretwurst et al.,"Radiation tolerant epitaxial silicon detectors", presented at 6th RD50 Workshop, Helsinki, June, 2005.
[22] V. Cindro et al.,"Trapping of Electrons and Holes in p type Silicon Irradiated with Neutrons", presented at IEEE NSS-MIC Symposium, San Diego, October, 2006.
[23] E. Fretwurst et al.,"Radiation damage studies on MCz and standard and oxygen enriched epitaxial silicon devices", , presented at the 6th RESMDD conference, Florence 2006.
[24] N. Manna et al., "Study of radiation damage induced by protons and neutrons on heavily irradiated Magnetic Czochralski and Epitaxial silicon detectors", presented at 8th RD50 Workshop, Prague, June 2006.
[25] G. Kramberger et al., "Recent CCE measurements with neutron irradiated epi-Si pad detectors", presented at 8th RD50 Workshop, Prague, June 2006.
[26] M. Huhtinen, , Nucl. Instr. and Meth. A491 (2002) 194.
[27] V. Khomenkov et al., "Neutron irradiation effects in epitaxial silicon detectors", presented at the 6th RESMDD conference, Florence 2006.
[28] N.Manna et al., "SMART Detector Project: recent results from the SMART experiment", presented at the 6th RESMDD conference, Florence 2006.
[29] A.Macchiolo et al., "", presented at IEEE NSS-MIC Symposium, San Diego, October, 2006.
[30] G. Segneri, et al., Radiation hardness of high resistivity n- and p-type magnetic Czochralski silicon, Nucl. Instr. and Meth. A (2006), doi:10.1016/j.nima.2006.10.262
[31] A.G. Bates and M. Moll, Nucl. Instr. and Meth. A555 (2005) 113.
[32] V. Khomenkov et al., SOLID STATE PHENOMENA 108-109 (2005) 315.
[33] N. Manna et al., "Characterization of n and p-type diodes processed on Fz and MCz silicon after irradiation with 24 GeV/c and 26 MeV protons and with reactor neutrons", presented at 6th RD50 Workshop, Helsinki, June 2005.
[34] V. Cindro et al., , Nucl. Instr. and Meth. A419 (1998) 132.
[35] V. Cindro et al., , Nucl. Instr. and Meth. A450 (2000) 288.
[36] V. Cindro et al., , Nucl. Instr. and Meth. A476 (2002) 565.
[37] G. Kramberger et al., "***Effect of bias voltage on full depletion voltage measured for different materials*** ", presented at 9th RD50 Workshop, CERN, October 2006.
[38] I. Dolenc et al., "Room temperature annealing of Epi-Si detectors", presented at 7th RD50 Workshop, CERN, November, 2005.
[39] E. Fretwurst et al.," Status report on new epi-devices", presented at 8th RD50 Workshop, Prague, June, 2006.
[40] G. Kramberger et al., , Nucl. Instr. and Meth. A481 (2002) 297.
[41] J. Weber et al., ""Measurement of the Trapping Time Constant in Neutron-Irradiated Silicon Pad Detectors", presented at IEEE NSS-MIC Symposium, San Diego, October, 2006.
[42] O. Krasel et al., IEEE Trans. NS 51(1) (2004) 3055.
[43] T. Lari et al., Nucl. Instr. and Meth. A 518 (2004) 349.
[44] G. Kramberger et al., , Nucl. Instr. and Meth. A 571 (2007) 608.
[45] M. Bruzzi et al., presented at 6th Hiroshima Conference, Carmel USA, September 2006.
[46] G. Kramberger et al., , Nucl. Instr. and Meth. A 554 (2005) 212.
[47] P.P. Allport et al., IEEE Trans. NS 52(5) (2005) 1903.

6 New Materials

6.1 Silicon Carbide detectors

The most recent results on SiC concern the use of epitaxial and semi-insulating materials, e.g. [1-4]. Considerable effort should be concentrated on better understanding the detection performance of SiC detectors after heavy irradiation. Degradation of the detectors with irradiation is caused by lattice defects. Understanding of the defect generation and kinetics would make it possible to purposely modify the material in order to reduce the degradation of the electrical properties of the detectors [5, 6].

In 2006 the new results on radiation hardness of SiC detectors included three aspects:

- study of radiation induced defects and correlation with degradation of detector properties;
- recovery of irradiated detector properties via annealing;
- radiation hardness of SiC detectors irradiated by 8 MeV protons.

6.1.1 Deep levels in 4H SiC epilayers induced by neutron irradiation up to 10^{16} n/cm2 and correlation to detector characteristics degradation

Schottky diodes were manufactured by Selex Integrated Systems (Roma, Italy) on epitaxial 4H-SiC layer grown by CREE Research (USA). The details of the processes are reported in [7, 8]. The epilayer thickness and its net doping concentration (N_D-N_A) before irradiation were found to be 39 μm and 6.5 x 10^{14} cm^{-3}, respectively. The samples were irradiated with increasing fluence Φ of 1 MeV neutrons at TRIGA Reactor in Ljubljana in the range 2x10^{13} cm^{-2} to 8x10^{15} cm^{-2}.

The properties and the electronic levels associated with the defects were analyzed by I(V) characteristics, Deep Level Transient Spectroscopy (DLTS) and Photo-Induced Current Transient Spectroscopy (PICTS) measurements up to 650 K. The detector performance was obtained by the measurement of signals arising from 5.486 MeV α-particles from a ^{241}Am source in vacuum.

I-V and C-V characteristics as well as diode spectroscopy measurements demonstrated that a fluence threshold exists that makes 4H-SiC to dramatically change its transport properties. From I-V characteristics as a function of the fluence it can be inferred that:

a) After irradiation the material becomes more resistive, as indicated by the decrease of the current density both in forward and reverse bias polarity (compensation of 4H-SiC Schottky diodes due to radiation induced defects was reported in [9]);
b) Irradiation with fluences higher than 8 x 10^{14} cm^{-2} gives rise to the same current density in forward and reverse bias polarization (Fig. 6-1).

Reverse current was also measured in the temperature range from 294 to 560 K in order to estimate the thermal activation energy E_t of defect centers. Two approximate grouping of curves were identified which refer to diodes irradiated at fluences below 2x10^{14} cm^{-2} and higher than 3x10^{15} cm^{-2}, respectively. The remarkable CCE degradation observed in the most irradiated samples has to be ascribed to the induced deepest levels at $E_t \geq 1.04$ eV. The main findings of CCE vs. Φ data (Figs. 6-2 and 6-3) are as follows:

a) CCE decreases towards an asymptotic value when increasing the neutron fluence;
b) Even at Φ of 8x10^{15} cm^{-2}, the detector keeps still operative, although the CCE decreases to about 20%.

DLTS and PICTS measurements were carried out before and after each irradiation step. DLTS gives information on majority carrier traps, while PICTS is applied to highly resistive samples and gives information on both majority and minority carriers. Both methods can determine level enthalpy E_t and capture cross section σ. However, λ-corrected DLTS measurements do give an accurate determination of the trap density N_t whilst by PICTS it is possible to estimate only the order of N_t.

Fig. 6-4 shows typical DLTS spectra of un-irradiated and irradiated diodes. The density of deep levels (DLs) SN5 and SN6 is too low (in the order of 10^{12} cm^{-3}) in un-irradiated sample and cannot affect the CCE after irradiation, in agreement with the data of Fig. 6-2. Two main findings can be evidenced from the DLTS results after irradiation at 2x10^{13} and 6x10^{13} cm^{-2}:

a) a new electron trap, labeled SN7, with $E_t = E_c$ - 1.50 eV appears;
b) N_t of SN5, SN6 and SN7 increases with the fluence Φ. Their maximum value, however, keeps always lower than $7x10^{13}$ cm^{-3}, that explains the good CCE even after irradiation at the above mentioned fluences.

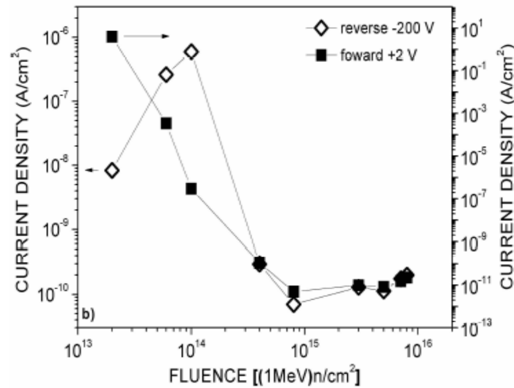

Fig. 6-1. Forward and reverse current density as a function of the fluence Φ, measured at +2 V and –200 V, respectively.

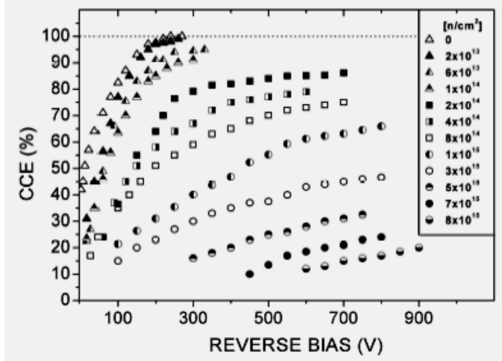

Fig. 6-2. Charge collection efficiency vs. applied voltage bias at different fluences.

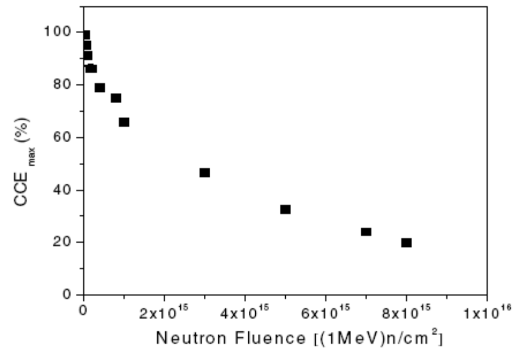

Fig. 6-3. CCE values at the highest applied voltages (CCE_{max}), as a function of the neutron fluence.

Due to compensation of free carriers by the deep levels at $\Phi>1x10^{14}$ cm^{-2}, PICTS was applied for estimation of defect parameters. A typical PICTS spectrum is shown in Fig. 6-5 relevant to a diode irradiated with a fluence of $8x10^{14}$ cm^{-2}. The highest peaks are observed between 400 and 650 K (excluded SN1) and correspond to DLs SN5, SN6 and SN7, the characteristics of which are reported in Table 6-1. A few of these levels correspond to the electronic levels detected by DLTS in the lower fluence irradiated samples, but they exhibit different features. As the fluence raises above10^{15} cm^{-2}, the PICTS normalized signal of these levels and, consequently, their density N_t increase. N_t values evaluated for the most irradiated samples (Φ = (7-8)$x10^{15}$ cm^{-2}) are reported in Table 6-1 together with E_t and σ, determined by an Arrhenius plot. The deepest levels SN6 and SN7 become dominant at the highest fluence, meaning that their trapping times are comparable to or lower than the charge carrier transit time in the detector [1]. According to [10-12], these defects can be identified as a defect complex involving carbon-vacancy-, carbon- and silicon-vacancy-defects. From the available data it is not possible to quantitatively assess the dependence of N_t on Φ for the level SN7 when Φ goes up higher than 3 x 10^{15} cm^{-2}. For this purpose, measurements by Current-DLTS are underway.

Conclusion

a) Even after an irradiation at fluence of $8x10^{15}$ cm^{-2}, the diodes are still able to detect α-particles with a CCE of ≈ 20% at the highest reverse bias applied.

b) The detectors continue to operate with a high CCE (≈ 80%) until fluences of some 10^{14} cm^{-2}. After irradiation with fluences of the order of 10^{15} cm^{-2}, CCE decreases to an asymptotic value.

c) A resistivity increase was observed with quite similar I(V) response in forward and reverse bias when the irradiation fluence approaches 10^{15} cm^{-2}.

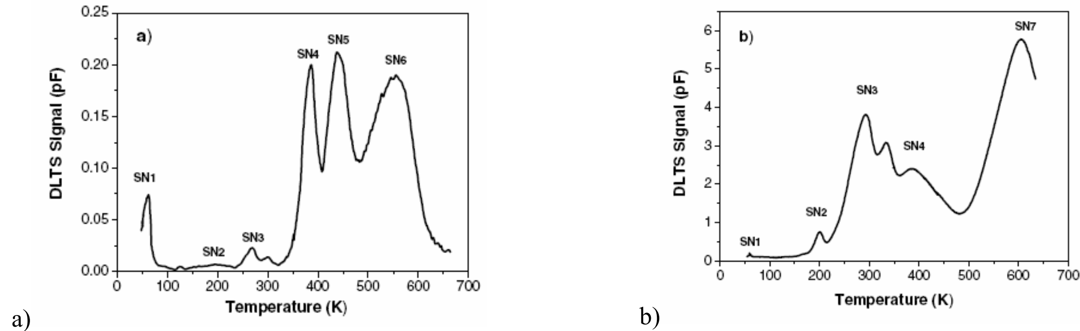

a) b)

Fig. 6-4. Typical DLTS spectra of a) un-irradiated diodes, and b) diode irradiated with fluence of 6 x 10^{13} cm^{-2} obtained with bias voltage -10V and fill 10 V, pulse width 10 ms, emission rate 11.6 s^{-1}.

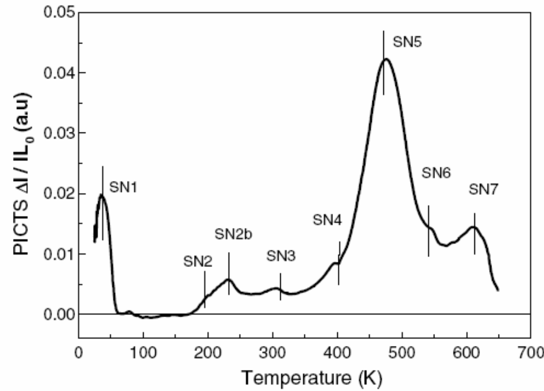

Fig. 6-5. PICTS spectrum of a diode irradiated with fluence $\Phi_n = 8 \times 10^{14}$ cm^{-2}. The emission rate was e_n = 25.6 s^{-1}, the filling pulse 100 ms. The sample was excited by an UV source with a wavelength equal to 372 nm and biased at –5 V.

Table 6-1

Enthalpy E_t, concentration N_t and capture cross section σ of the levels observed in 4H-SiC diodes irradiated up to 1 MeV neutron equivalent fluence Φ = 7 - 8 x 10^{15} cm^{-2}

Trap label	Et (eV)	Nt (cm^{-3})	$\sigma(cm^2)$	Label
SN1	0.05	10^{14}	8.8 x 10^{-20}	N_{hs} [a]
SN2	0.41	10^{14}	3.7 x 10^{-15}	EH1 [b], $Z_2^{0/+}$ [c]
SN2b	0.49	10^{13}	4.0 x 10^{-15}	RD5, ID_8 [d], $Z_1^{0/+}$ [c]
SN3	0.68	10^{13}	7.0 x 10^{-15}	Z1/Z2 [e] [c]
SN4	0.68	-	6.0 x 10^{-16}	M2 [f], EH3 [h]
SN5	0.82	10^{15}	2.0 x 10^{-16}	$RD_{1/2}$ [d], SI5 [g]
SN6	1.16	10^{15}	2.8 x 10^{-15}	EH5 [b], $IL_{4/5}$ [h]
SN7	1.50	10^{16}	3.0 x 10^{-14}	EH6/EH7 [b] [i]

d) Trapping centers that play the key role in the CCE decrease are related to the DLs with Et > 1.04 eV. The defects SN6 and SN7, the concentration of which is in the

order of 1015-1016 cm-3 for the mostly irradiated samples, have been identified as the trapping centers that mainly determine the detector degradation.

6.1.2 Recovery of characteristics of SiC neutron irradiated diodes via annealing

The diode structure, made at CNR-IMM (Bologna, Italy) [13], is based on a p^+ emitter, ion implanted in a thick (55 μm) very lightly doped (2×10^{14} cm^{-3}) *n-type* epilayer. A multiple Al^+ implantation process was carried out at 305°C, in order to obtain plateau and depth values of 4×10^{19} cm^{-3} and 0.4 μm, respectively. Diode area was between 0.0013 and 0.0154 cm^2. Most of the diodes featured a 200 μm wide, 0.6 μm deep, p^- junction terminal extensions with a doping $N_A = 5\times10^{17}$ cm^{-3}. The samples were irradiated with increasing fluence of 1 MeV neutrons at TRIGA Reactor by 6 different fluence values F logarithmically distributed in the range 1×10^{14} cm^{-2} to 1×10^{16} cm^{-2}. Diodes have been fully characterized before and after irradiations, and the results have been presented in [13-15].

After irradiation the devices became intrinsic. The I-V curves were measured in the range 0-950 V. The current of irradiated devices is always lower than in unirradiated diodes. The compensation of the free charge carriers due to the deep levels generated by irradiation is responsible for the increased resistivity and the decreased current density at constant voltage. The noise due to the current is very low even at RT and it is not necessary to cool the device even after very high fluences.

In spite of the fact that after irradiation the p^+n junction disappeared due to compensation, the generated charges were separated by the high electric field and collected at the electrodes. After a fluence of 1×10^{14} n/cm^2, the charge collection at the highest voltage of 950 V (Fig. 6-6) is reduced from 3100 e^- to 2800 e^-, due to traps introduced by neutrons, and seems very much degraded beyond $\sim10^{15}$ n/cm^2. The asymptotic CC is near 800 e^-. Over F $\sim3\times10^{15}$ n/cm^2 the collection is very low. After a fluence of 10^{16} (1 MeV) n/cm^2 the estimated CCs are of the order of 100 e^-. As described previously in [13, 16-18], neutron, proton and electron irradiations introduce deep levels in the band-gap of SiC, producing free-charge-carrier compensation. Low temperature annealing [16, 19] causes some levels to disappear or rearrange. The task of this study is analyzing if this effect produces damage recovery in terms of collected charges and leakage current.

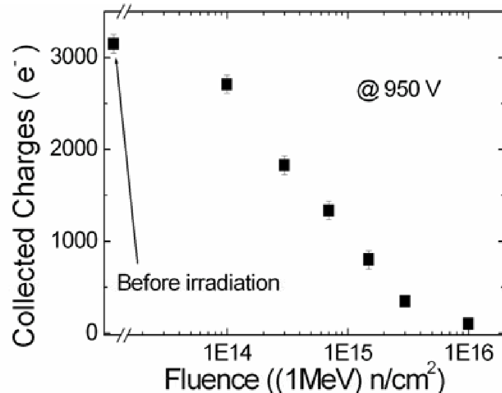

Fig. 6-6. Collected charges as a function of the fluence. The diode diameter is 1 mm and the diode is not annealed. CC measured at 950 V.

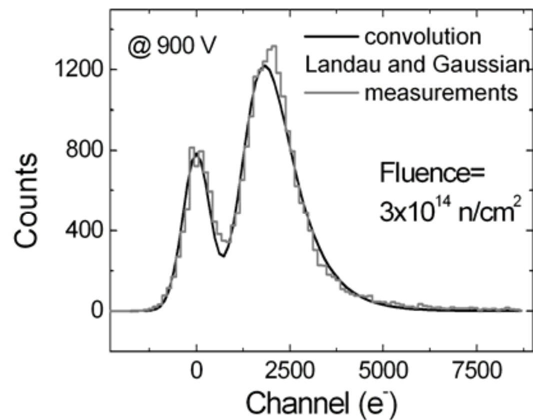

Fig. 6-7. Convolution of the signal and the pedestal at 900 V after an irradiation of 3×10^{14} n/cm^2 and an annealing at 200°C for 30 minutes. Diode diameter is 1 mm.

The annealing at 80°C is the typical thermal process for Si, which compresses the time-scale for expected long-term effects during real operation scenario. In our case 80°C is the maximal T we could use in-situ during CCE measurements. The evolution of the reverse current as a function of the annealing time at 80°C showed that the current density decreased after 30 min to a very low value (15 nA/cm^2 at 7×10^{14} n/cm^2, and then remained almost constant even after many hours of annealing

(~170 h). CCE measurements have been repeated after every thermal cycle at 80°C. After many hours of annealing, a slight increase of the collected charge was observed, but in the range of the experimental error. Considering these results we conclude that the damage is not recovering after annealing at 80°C.

Further electrical characterizations after annealing at 200°C and 400°C have been carried out. After 30 minutes at 200°C a partial recovery of the damage occurred. Fig. 6-7 shows the convolution of the signal and the pedestal at 900 V after an irradiation of 3×10^{14} n/cm^2 and an annealing at 200°C for 30 minutes. The pedestal (noise) and the signal peaks are well separated. The most probable value of the Landau distribution is 2200±50 e^-. Before annealing CC was 1800 e^-, i.e. CC increase of 400 e^- is observed. The current density at 900 V decreases from 23 nA/cm^2 measured before annealing, to 15 nA/cm^2 after 200°C for 30 min.

After 30 min at 400°C the reverse current density for the device irradiated at 7×10^{14} n/cm^2 further decreases (Fig. 6-8,a). In fact at 900 V we measured a value of 8.5 nA/cm^2. Moreover the CC at 900 V increases up to 1900 e^- with respect to 1400 e^- before annealing (Fig. 6-8,b). After an annealing at 400°C we have a further, still partial recovery of the damage.

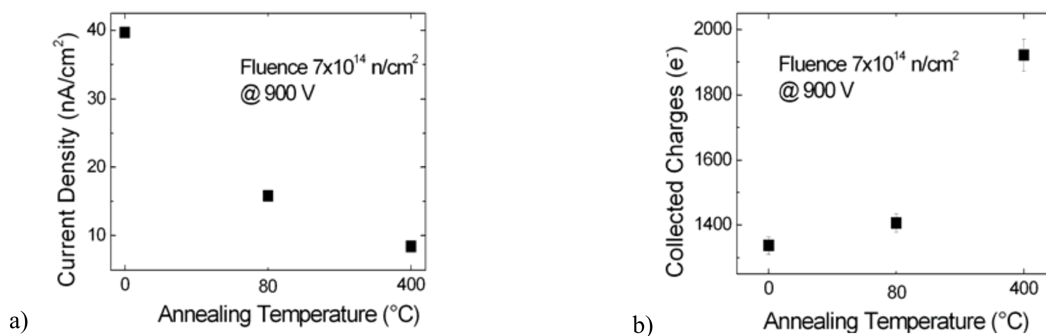

Fig. 6-8. Current density (a) and collected charge (b) as a function of the annealing temperature for the device irradiated with a fluence of 7×10^{14} n/cm^2. The samples were heated for 30 minutes at the indicated temperature (isochronal annealing).

Conclusion

Annealing effects on SiC p^+n diodes used as MIP detectors after very high 1 MeV neutron fluences have been analyzed. At 80°C, a decrease of the reverse current after 30 min annealing occurred while further annealing did not produce any effect. Also, after a number of thermal cycles at 80°C we could only observe the CC increase within the experimental error. After an annealing at 200°C the collected charge, for a diode irradiated with a fluence of 3×10^{14} n/cm^2, increased from 1800 e^- to 2200 e^-, showing a partial recovery of the damage. After 30 min at 400°C the leakage current further decreased while the collected charges increase was of 40%. In these cases we probably obtain a decrease of the concentration of the deepest levels, but additional spectroscopic analysis as a function of the annealing temperature is planned to confirm this hypothesis.

6.1.3 Radiation hardness of SiC diodes to high fluences of 8 MeV protons

The aim of this study was investigation of radiation hardness of low doped 4H-SiC epilayers (IKZ, Berlin) with respect to 8 MeV proton irradiation. 4H-SiC films with (50-55) μm nominal thickness and donor doping $\{N_D - N_A = (2\text{-}5)\times10^{14}\ \text{cm}^{-3}\}$ were used for processing the diode structure:

1. Schottky diode (wafer # N31-41, Alenia processing);
2. p+-n diodes, chip Die M6 (designed by the INFN-Gruppo V and University of Perugia).

Samples were irradiated by protons 8 MeV in the fluence range 5.0×10^{13} cm^{-2} up to 3.0×10^{14} cm^{-2} (Table 6-2). According to the theoretical NIEL calculations for silicon [20, 21] the damage factor for 8 MeV protons is 10 with respect to to 23 GeV protons. The charge collection efficiency of SiC detectors was investigated using nuclear spectroscopy technique with 5.4 MeV α-particles (range ~ 20 μm).

All samples demonstrated the same behavior of CCE vs. bias U dependences. The CCE of non-irradiated detectors reached a constant value of ~ 100 % already at 100 V for Schottky detectors and at 30–40 V for p^+-n diodes (Fig. 6-9). The linear increase of the signal was approximated by a function of the diffusion and drift components of the CCE:

Table 6-2
The charge collection efficiency (%) of SiC-detectors after irradiation by 8 MeV protons

samples	before irradiation*	8 MeV proton fluence (10^{14} cm^{-2})			
		0.5	0.75	1	3
Schottky	100	80	65	53	
p^+-n	100			75	37

*Spectroscopy with 3.5 MeV α-particles was used.

$$(CCE)\times E_\alpha = \left(\frac{dE_\alpha}{dx}\right)L_D + \left(\frac{dE_\alpha}{dx}\right)W \quad (6\text{-}1)$$

Here E_α is the energy of an α-particle; (dE_α/dx) the specific energy loss in the initial part of the Bragg curve; L_D the diffusion length, $W \propto (U+V_{bi})^{1/2}$ is the space charge region width; V_{bi} the built-in potential. In this way, L_D ~ 7 μm for Schottky detectors and L_D ~ 14 μm for p^+-n diodes were obtained.

A simple model of signal formation was proposed in [22]. The model allows differentiating the contributions of the electrons and holes to CCE. The normalized amplitude of a signal (q/q_0 = CCE) as a function of a bias (U) is expressed in a simple form:

$$\frac{q}{q_0} = \frac{q_e + q_h}{q_0} = P_1 U\left[1-\exp\left(-\frac{2R}{3dP_1U}\right)\right] + P_2 U\left[1-\exp\left(-\frac{1-\frac{2R}{3d}}{P_2 U}\right)\right] \quad (6\text{-}2)$$

Here two parameters $P_1 = (\mu\tau)_e /d^2$, $P_2 = (\mu\tau)_h /d^2$; μ is the mobility, τ is the lifetime before the trapping to the energy level for electrons and holes accordingly; d – detector thickness; $q = q_e + q_h$ – a total charge and q_0 the charge generated by α-particles with a range R. The main condition of Eq. (6-1) derivation is the electric field constancy. In order to obtain a more uniform distribution of the electric field along the detector thickness it was proposed to use forward bias mode, in which carrier injection is possible. The structure operates as a resistor with a high resistivity. The values of $\mu\tau$ for both bias modes were found to be about 10^{-8} cm^2/V (Table 6-3). Quantitatively, the values obtained at a mobility of ~10^2 cm^2/(Vs) correspond to the carrier lifetimes of ~ 0.1 ns.

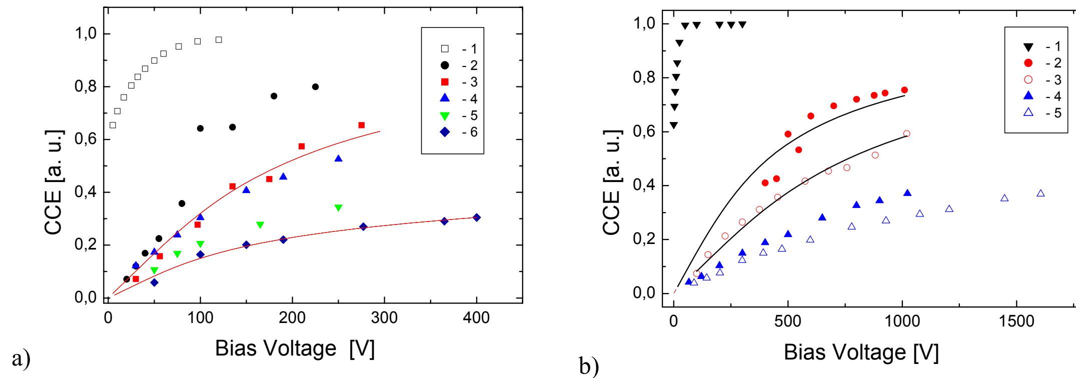

Fig. 6-9. Charge collection efficiency, a) Alenia group samples as a function of the reverse (1,2,3,4) and forward (5,6) bias before (1) and after irradiation at a fluence: 2,5 – 5×10^{13} cm^{-2}, 3 – 7.5×10^{13} cm^{-2} and 4,6 – 10^{14} cm^{-2}; b) Perugia group samples as a function of the reverse (1,2,4) and forward (3,5) bias before (1) and after irradiation at a fluence: 2,3 – 10^{14} cm^{-2} and 4,5 – 3×10^{14} cm^{-2}.

An illustrative factor for the comparison of the detector operation modes is the behavior of its resolution, FWHM of the amplitude spectrum. Fig. 6-10 shows the FWHM as a function of bias for the two modes. After the first irradiation (F of 1.0×10^{14} cm^{-2}), a significant difference in amplitude variations can be clearly seen. After the second irradiation of the detectors of Perugia group at a fluence of 2×10^{14} cm^{-2}, the basic characteristics worsened by no more that a factor of 2 (CCE = 0.37; FWHM ≤ 20 %) as compared to the fluence of 1×10^{14} cm^{-2} (Table 6-3, Figs. 6-9,b and 6-10) [23]. By

contrast, the $\mu\tau$ values decrease super linearly. The main decrease is observed for the carriers that drift through the detector volume: for holes at forward bias (by a factor of 4.1), and for electrons at reverse bias (factor of 5.1).

Table 6-3

μτ values [cm^2/V] in p+-n samples after irradiation at a fluence of 1.0×10^{14} cm^{-2}

sample	$(\mu\tau)_e \times 10^8$		$(\mu\tau)_h \times 10^8$	
	reverse bias	forward bias	reverse bias	forward bias
D4a	3.06	1.8	1.5	1.1
D4c	3.1	1.5	3.4	1.5
D5c	1.7	0.48	0.88	0.97

We believe that, at fluences of 3 × 10^{14} cm^{-2}, the carrier transport cannot be adequately described in terms of a two-parameter model [22]. In addition, temporal instability of the basic detector characteristics (signal amplitude, energy resolution) and specific features of signal formation were revealed [24].

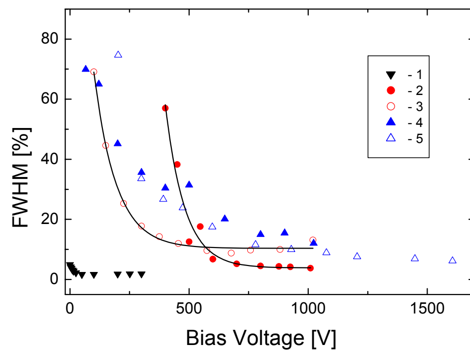

Fig. 6-10. Energy resolution for Perugia samples as a function of the reverse (1,2,4) and forward (3,5) bias before (1) and after irradiation at a fluence of 10^{14} cm^{-2} (2,3) and 3×10^{14} cm^{-2} (4,5)

In addition, the study of the mechanism of defect formation in SiC subjected to heavy ions irradiation was carried out. The structural and optical characteristics of 4H-SiC epitaxial layers (26 μm thick, ACREO, Sweden) irradiated by 710 MeV Bi ions in the fluence range 1.4×10^9–1×10^{13} cm^{-2} were investigated [25]. For the first time it was shown that the distribution of structural damage fits the calculation based on elastic collision. The important practical observation is that the defects induced by this more severe damage, as compared to that introduced by neutrons and protons, may be partially annealed at the prospective working temperature of SiC devices of 500°C.

Conclusion

1) Application of forward bias mode in which the electric field is distributed uniformly allowed separating the contribution of electrons and holes to the CCE of detectors irradiated at F≤1×10^{14} cm^{-2}. Beyond this fluence $\mu\tau$ should be regarded as effective values.
2) At fluence of 3×10^{14} cm^{-2} polarization is revealed at any polarity of the voltage. This polarization is due to carrier trapping to the deep levels of radiation induced defects. The degradation of the signal in time caused by polarization restricts the detector application in the spectroscopy mode while operation in the counting mode remains possible.

The future plan includes search for recovery of detector characteristics after the fluence of relativistic radiation via low temperature annealing, and the analysis of long term stability of detectors parameters.

6.2 GaN detectors

During 2006 tests of radiation hardness were performed on series of GaN material from Lumilog, Ltd., France, irradiated in 2005, and also new series that were delivered from Nitride, Ltd., Japan. Also a new type of material, GaN grown on Si substrate [26], was received from Berlin Technical University. The samples were processed at Glasgow University. 12 and 2.5 μm thick GaN detectors (series 36 and 45) were irradiated with protons (CERN) and neutrons (Ljubljana) to fluences ranging from 1x10^{14} cm^{-2} to 1x10^{16} cm^{-2}. The investigation of sample properties was carried out in three aspects:

1) technological processing,

2) material study,
3) measurements of detector characteristics.
The listing of the samples and summary of the results are presented in Table 6-4.

6.2.1 Technological processing

Ohmic and Schottky contacts on the 12 GaN, 36 GaN and 45 GaN materials were fabricated at the Glasgow University. For contact control deposition of 100x100 μm^2, 200x200 μm^2 and 300x300 μm^2 squares were made on all 3 materials. The square separation distances were in the range 2 to 50 µm. The metallization scheme used was 20/60/40/50 nm of Ti/Au/Pd/Au and then detectors were annealed at 850°C for 30 s. This procedure reveals defect structure at the surface, i.e. fast diffusion of impurities via defect region occurs that explains the problems related to the contacts.

Table 6-4
Summary on GaN samples studied in 2006

series	thickness (µm)	structure	material study	CCE		
					F = $1\cdot10^{16}$ cm^{-2}	
				non-irrad.	protons	neutrons
GaN on Si		GaN on Si	CPC: τ_{as}=22 ms			
		GaN-(AlN) on Si	PL: defects, trapping			
GaN bulk			CPC: τ_{as}=5 ms			
36GaN	2.5	SI GaN-n*GaN-sapphire	defect structure at surface	70	$2\cdot10^{15}$ cm^{-2}: 10	$2\cdot10^{15}$ cm^{-2}: 20
45GaN	2.5	-“-		97	20	40
12GaN	12	-“-	CPC: τ_{as}=6 ms	53	23	17
ICP 45GaN	12		C-V data!	100		

Inductively Coupled Plasma (ICP) etching was made on 45 GaN series to get contact to the n*GaN buffer layer. The aim of this structure is a better definition of the electric field lines (Fig. 6-11). It allowed receiving for the first time reliable C-V measurements.

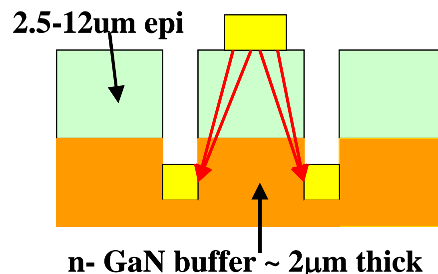

Fig. 6-11. Inductively Coupled Plasma etched sample 45 GaN

6.2.2 Material study

The investigation of GaN-on-Si material showed that the technology of compensation of the Si and GaN lattices misfit at room and at growth temperature by introducing AlN layers was not successful. The change of defect structure is demonstrated in the luminescence spectra (Fig. 6-12) as an increase of 2.2 eV defect related band and less pronounced exciton band, and as a long decay of photoconductivity signal due to the trapping carriers in the barriers (Fig. 6-13). Contact

photoconductivity (CPC), TSC and PL measurements were performed for both proton and neutron irradiated 36 GaN and 45 GaN detectors, and five neutron irradiated 12 GaN detectors were studied using CPC and PL measurements [27]. The study showed that substrate related defects play the most important role. Radiation introduces numerous defects with continuously changing activation energy in the wide band.

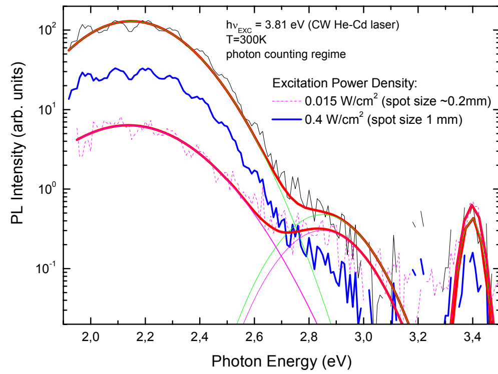

Fig. 6-12. Photoluminescence spectra of GaN-on-Si

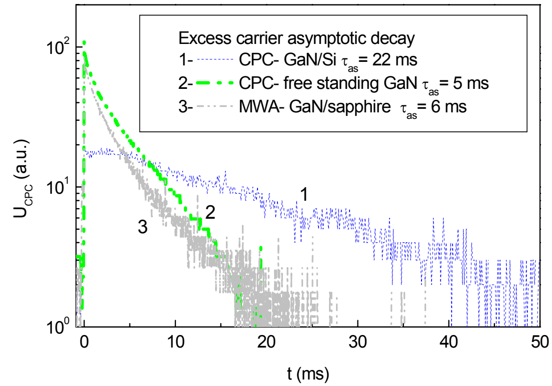

Fig.6-13. Comparison of photoconductivity decay in GaN-on-Si, GaN bulk (free standing) and GaN-on-sapphire

6.2.3 Detector characteristics

Evaluation of detectors included I-V and CCE measurements of non-irradiated, proton irradiated and neutron irradiated 12 GaN, 36 GaN and 45 GaN samples [28]. The new result is that I-V, C-V and CCE data were also obtained for a ICP etched 45 GaN detector. CCE measurements were carried out using 5.48 MeV α- particles from an ^{241}Am source. I-V characteristics of irradiated samples demonstrated non-monotonous current change with accumulated fluence. Detectors irradiated to fluences beyond $5\text{x}10^{15}$ cm^{-2} show the leakage current that at a bias of -100V is lower than that in a non-irradiated sample. As an example, I-V and CCE curves of sample 45 GaN irradiated by neutrons are presented in Fig. 6-14. In addition to the results described in a review [29], the investigations of this year demonstrated that radiation hardness of new series of samples based on the material grown in Nitride, Ltd., is better (Fig. 6-15).

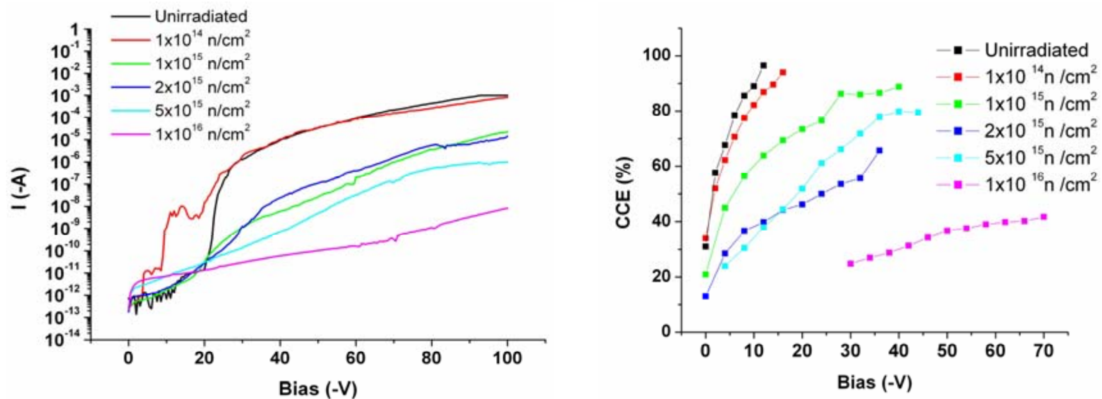

Fig. 6-14. I-V (a) and CCE (b) dependences for sample 45 GaN irradiated by neutrons

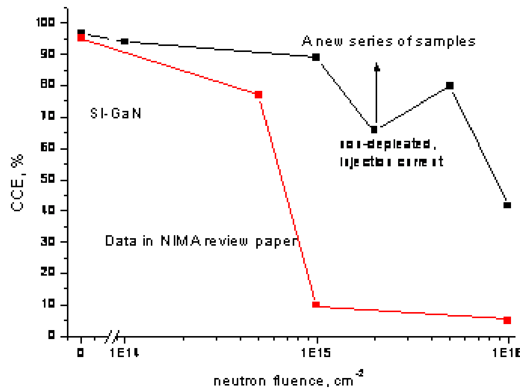

Fig. 6-15. A summary of the best CCE data in SI-GaN for 2004-2006 years

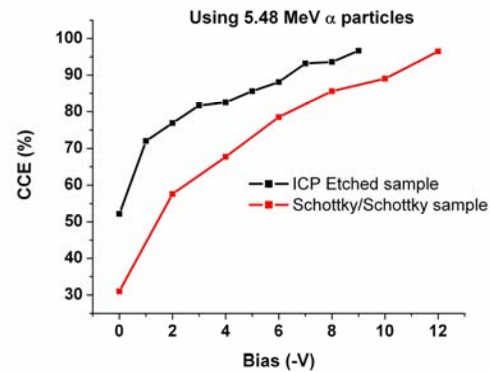

Fig. 6-16. Comparison of CCE vs. V data for samples 45GaN

Measurements on ICP 45 GaN sample showed an increased leakage current as compared to that of Schottky-Schottky diodes, while CCE was higher (Fig. 6-16) that is an optimistic result for the future development and study.

The detailed results on the investigation of GaN samples are also presented in [30-33].

Conclusion

It was shown that the substrate related defects play an important role and the detector properties were improved by increasing the epi-layer thickness. The maximal CCE in the samples with a larger GaN layer thickness is ~ 23% after 10^{16} p/cm^2 and 17% after 10^{16} n/cm^2.

The nearest tasks for future are an irradiation and study of advanced ICP GaN samples and the growth of SI-GaN on GaN substrate (suggested by Bremen University).

6.3 References for Chapter 6

[1] F. Nava et al. Nucl. Instrum. Meth. A505, 645, (2003).
[2] E. Kalinina et al. Mater. Sci. Forum , 483-485, 377,(2005).
[3] A. Castaldini, A. Cavallini, L. Rigutti and F. Nava. Mater.Sci.Forum 483-485, 359, (2005).
[4] J.Grant et al. (6 Int. Workshop Rad. Imag. Detectors IWORID-2004, July 25-29, Glasgow/Scotland)
[5] F.Lemeilleur, G.Linstrom, S.Watts. M.Moll, ROSE-RD48, (2002).
[6] G.Lindstrom,M.Moll,E.Fretwurst, Nucl. Instrum. Meth. A466, 308, (2001).
[7] F.Nava et al. IEEE Trans.Nucl. Sci. NS-53, 238, (2004).
[8] S.Sciortino et al. Nucl. Instrum. Meth. A552, 138. (2005).
[9] A.Castaldini, A.Cavallini, L.Rigutti. Appl. Phys. Lett. 85, 3780, (2004).
[10] L.Storasta, J.P.Bergman, E.Janzèn, A. Henry and J.Lu. J. Appl. Phys. 96, 9, 4909, (2004).
[11] St.G. Muller et al. Mat. Science Forum 433-436, 39, (2003).
[12] Y.Negoro, T.Kimoto and H.Matsunami. Appl. Phys. Lett. 85, 10, , 1716, (2004).
[13] F. Moscatelli et al. IEEE Trans. Nucl. Sci., vol. 53 n. 3, pp. 1557-1563, 2006.
[14] F. Moscatelli et al. Nucl. Sci. Symp. Conf. Record, 2005 IEEE Vol. 1, Oct 23 - 29, 2005, pp. 490 – 494.
[15] F. Moscatelli et al. Mater. Sci. Forum Vols. 527-529 (2006) pp. 1469-1472
[16] A. Castaldini, A. Cavallini, L. Rigutti and F. Nava. Appl. Phys. Lett., vol. 85 pp. 3780-3782, 2004.
[17] A. Castaldini et al. J. Appl. Phys. Vol. 98, n. 053706, 2005.
[18] A. A. Lebedev et al. J. Appl. Phys. 88 (11), pp 6265-6271, 2000.
[19] X.D. Chen et al. J. Appl. Phys. Vol. 94 (5), pp. 3004-3010, 2003.
[20] D. Bechevet et al. Nucl. Instr. and Meth. A 479 (2002) p. 487-497.
[21] M. Huhtinen. Nucl. Instr. and Meth. A 491, (2002) p. 194-215.
[22] N.B. Strokan, A.M. Ivanov, A.A. Lebedev. Transport of the charge carriers in SiC-detector structures after extreme radiation fluences, Nucl. Instr. and Meth. (in press, NIM A 45773) 569/3 pp. 758-763.

[23] A.M. Ivanov, N.B. Strokan, A.A. Lebedev, V.V. Kozlovski. The Influence of the extreme Fluences of 8 MeV Protons on Characteristics of SiC Nuclear Detectors produced by Al Implantation, pres. VI European Conf. on Silicon Carbide and Related Materials, Sept 3-7, 2006, Newcastle, UK.
[24] A.M. Ivanov, A.A. Lebedev, N.B. Strokan. Semiconductors 40 (2006) 1227-1231.
[25] E.V. Kalinina et al. Structural peculiarities of 4H-SiC irradiated by Bi ions, pres. 8th Intern. Workshop on Beam Injection Assessment of Microstructures in Semiconductors (BIAMS 2006), June 11-14, 2006, St.-Petersburg, Russia.
[26] A.Dadgar et al. Phys. stat. sol. (c) 0(6), 1583.1606 (2003).
[27] J. Vaitkus et al. Properties of irradiated semi-insulating GaN; pres. 8 RD50 Workshop, June 24-26, 2006, Prague; www.cern.ch/rd50.
[28] J. Grant et al. I-V & CCE results of neutron irradiated GaN Schottky Detectors; pres. 8 RD50 Workshop, June 24-26, 2006, Prague; www.cern.ch/rd50.
[29] P.J.Sellin,and J.Vaitkus. Nucl. Instr. and Meth. A 557 (2006) 479.
[30] J. Vaitkus et al. CERN Large Hadron Collider projects to improve the radiation hardness of ionizing radiation detectors: The role and control of defects in Si and potential of GaN. Lithuanian J.Physics - Lietuvos fizikos žurnalas Vol. 45 (2005) 437-444.
[31] V. Kazukauskas, V. Kalendra, J.-V. Vaitkus. Nucl. Instr. and Meth. A 568 (2006) 421–426.
[32] E. Gaubas et al. Recombination characteristics of the proton and neutron irradiated semi-insulating GaN structures; pres. RESMDD’6, Oct 10-13, 2006, Florence (Nucl. Instr. and Meth. A, in press).
[33] J. Vaitkus et al. Semi-Insulating GaN – radiation hard semiconductor for ionizing radiation detectors; pres. 33th Internat.Conf. on High Energy Physics (Moscow ICHEP-2006).

7 New Structures

7.1 Introduction

The past year of 2006 has been a successful year for the new structures working group of RD50. The thin detectors sub-section reports encouraging device fabrication and irradiation tests performed on 50µm p-i-n diodes. The main progress in 3D detectors has been the full characterization of the 3D devices fabricated by IRST/CNM in 2005, including characterization of short strip detectors with ATLAS readout electronics, as well as the design and start of the fabrication of 3D devices at CNM and a commercial supplier IceMOS Technology. The work on semi-3D detectors has progressed at BNL but will be reported in the next status report when more detailed data will be available.

7.2 Thin detectors

Thin 50µm thick n^- float zone, FZ, silicon detectors of various resistivities (3 kΩcm to 150 Ωcm) have been fabricated at MIP Munich and tested by the MPI and Hamburg groups. The process steps of the thin detectors are illustrated in figure 2-1. The top wafer, which becomes the thin detector, is back side processed. The handle wafer, which is the supporting wafer, and the top wafer are then bonded together using a commercial wafer bonding technique. The wafer bonding requires surface oxidation of the two wafers and a high temperature (>1000°C) annealing process to bond the wafers together. The top wafer is lapped and polished to the required thickness and processed in a standard fashion. The back side is then etched, with the silicon oxide layer at the bonded wafer-wafer interface acting as the etch stop, and finally metallised as required.

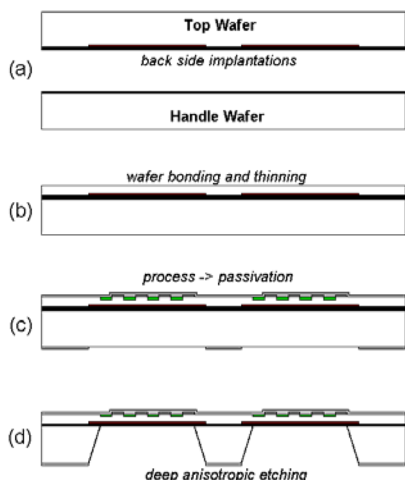

Fig. 2-1. The process sequence for production of thin silicon sensors with electrically active back side implantation starts with the oxidation of the top and handle wafer and the back side implantation for the sensor devices (a). After direct wafer bonding, the top wafer is thinned and polished to the desired thickness (b). The processing of the devices on the top side of the wafer stack is done on conventional equipment; the openings in the back side passivation define the areas where the bulk of the handle wafer will be removed (c). The bulk of the handle wafer is removed by deep anisotropic wet etching. The etch process stops at the silicon oxide interface between the two wafers (d).

7.2.1 Prototyping

Two designs, (Type I and II), of thin diode were fabricated as detailed in figure 2-2. The difference between the two devices is the side of the patterned p^+ implant with respect to the handling wafer as shown in figure 2-2. Type I devices have been fabricated to $10mm^2$, while type II devices have been made with sensitive areas as large as $6.5cm^2$.

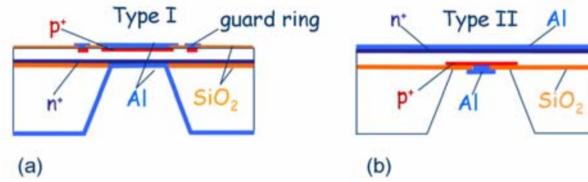

Fig. 2-2. Cross-sections of the two different types of p-i-n diodes on FZ n$^-$-substrate. Type I has a large-area area ohmic contact at the bond interface with pn-junctions and guard rings at the top wafer surface (a), Type II is vice versa with a structured p$^+$-implant at the bond interface and a large-area ohmic contact at the top wafer surface (b).

7.2.2 Irradiation results

Type I high resistivity diodes (3 kΩcm) were irradiated with 23 GeV protons for a fluence from 4×10^{13} cm^{-2} to 8.6×10^{15} cm^{-2}. In order to investigate the radiation induced changes to their short- and long - term operation, after irradiation all samples underwent an isothermal annealing procedure at 80°C with cumulative steps up to 45000 minutes (≈31 days). After each annealing step the devices were characterized at 20°C by C-V and I-V measurements. After the full annealing cycle of 31 days charge collection measurements were performed with ^{244}Cm 5.8 MeV α-particles.

The development of the devices full depletion voltage, V_{fd}, extracted from C-V measurements after annealing at 80°C as function of fluence is shown in figure 2-3. The annealing time used corresponded to that at which the annealing curve of V_{fd} (or ΔN_{eff}) reached its minimal value (see figure 2-4). According to the standard parameterization of $N_{eff}(\Phi)$, taking only donor removal and acceptor creation into account (solid line in figure 2-3), a β value of 3.6x10^{-3} cm^{-1} was derived from the slope at high fluences. This β-value is in the same order as obtained for oxygen enriched FZ (DOFZ) silicon (see [1]) although these devices were not subjected to any deliberate oxygenation procedure. Possibly the high temperature treatments during the bonding and the device processing lead to an in-diffusion of oxygen from the oxide surface layers, which may have increased the oxygen concentration throughout the 50 µm thin bulk beyond the initial level of the untreated material.

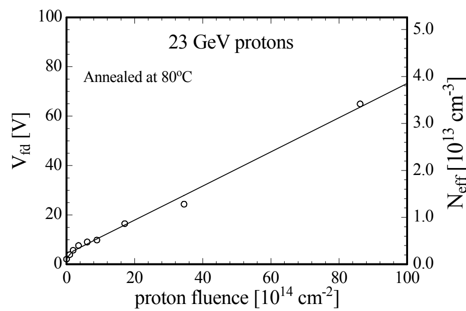

Fig. 2-3 Development of full depletion voltage V_{fd} as function of fluence after annealing at 80 °C for specific durations (8 min up to 1.7×10^{15} cm^{-2}, 30 min at 3.5×10^{15} cm^{-2}, 60 min at 8.6×10^{15} cm^{-2}).

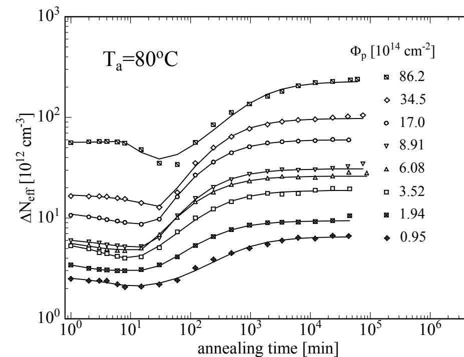

Fig. 2-4 Change of effective doping concentration as function of cumulated annealing time at T_a = 80ºC after irradiation with different fluences.

In figure 2-4 the annealing of ΔN_{eff} for the full set of fluences is shown. The solid lines are the result of fits according to the functional dependencies as described by the Hamburg model [1]. From these plots it becomes obvious that the minimum of the annealing curves shifts to longer annealing times for the last two high fluence values. This shift corresponds with an increase of the short term annealing time constant and in particular a strong delay in the reverse annealing as function of fluence. A similar dependence has also been reported for DOFZ-detectors but at lower fluences [1].

For the reverse current per unit volume, taken at full depletion and after an annealing of 8 min at 80°C, a linear increase with accumulated fluence is observed. The extracted slope representing the

current related damage parameter is $\alpha(T_a=80°C, t=8\ min) = 2.4\times10^{-17}$ A/cm which is in agreement with results of numerous studies on various silicon materials [2].

In figure 2-5 the measured charge collection efficiency, CCE, is plotted as function of fluence. For all devices the CCE was obtained at a detector bias of 190 V, which was always above their full depletion voltage. The solid line in figure 2-5 is a fit to the experimental data according to: $CCE = 1-\beta_c\times\Phi$. For the parameter β_c a value of 3.4×10^{-17} cm^2 is derived which leads to an extrapolated CCE value of 66% at $\Phi = 10^{16}$ cm^{-2}. This is comparable to charge collection measurements on proton irradiated 50 µm epitaxial devices performed with a ^{90}Sr β source were a value of 60% at 10^{16} cm^{-2} is reported [3]. This indicates that for thin detectors charge collection measurements with α-particles result in similar CCE values as achieved with mips. Further, these observations point to a universal behaviour of charge carrier trapping in highly proton irradiated silicon devices being independent on the silicon material type and the impurity content. More details on this work can be found in [4].

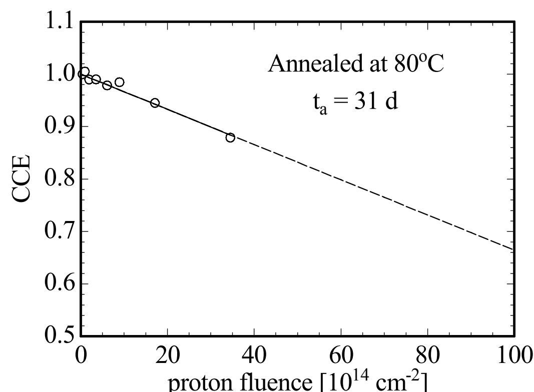

Fig. 2-5 Decrease of CCE with fluence after full annealing cycle at 80°C. Measurements performed at 20°C.

7.2.3 Future Work

Future work is aimed at further device fabrication to understand the ability to make structured sensors that can be used in full detector tests. Simulation results from RD50 collaborators will be compared to the experimental results.

7.3 3D detectors

The past year has been very successful with the development of 3D detectors and their characterization. Results are reported on the modelling and characterization of single column 3D detectors fabricated at ITC-IRST, Trento. Further to devices fabricated by the Trento group, devices have been designed and are under fabrication at CNM, Spain. The New Mexico group has joined RD50 and their work on 3D detectors fabricated at Stanford is reported.

7.3.1 Testing and simulation of single column type 3D detectors

The single column type 3D detectors, (3D-stc), reported in last year's status report have been further investigated by several university groups. The IV and CV characteristics of simple pad devices made from an array of 3D-stc devices have been measured at IRST, Glasgow University. The results obtained are compared to simulations performed at each institute with ISE-TCAD. Charge collection measurements of pad devices and strip devices have been performed by the Glasgow, Freiburg, Florence and Santa Cruz groups. The Ljubjana group has performed the first position sensitive TCT measurements on small strip 3D-stc devices to illustrate the dependence of the charge collection efficiency on the charge deposition position inside the device.

7.3.2 Measured and simulated IV and CV characteristics

As reported in last years status report 3D-stc detectors have been fabricated and tested [5], [6]. The basic unit cell of the 3D detector have been connected together to form pad detectors and strip detectors with either 10 or 250 columns per strip. The devices are all n+ doped columns inside a lightly doped p-type substrate with a uniform n+ doped back contact. Several different isolation techniques on the front side around the n+ doped columns were fabricated and tested. The IV and CV curves have been measured at all the institutes noted above, while the simulations reported below were performed at Glasgow and IRST.

The detector was simulated using ISE-TCAD. In order to keep the size of the simulated mesh as small as possible the device's symmetry was exploited and only a section of the device with ¼ of an n+ column with silicon of thickness of ½ of the column pitch was simulated as shown in figure 3-1. The simulated device has n+ columnar electrodes implanted on a p-type silicon substrate. For simplicity, the columns are not hollow but made of silicon doped with phosphorous with a concentration of 10^{19}cm^{-3}. The column depth was 150µm, the diameter was 10µm, the pitch was 80µm and the wafer thickness was 500µm. The substrate resistivity was 5k·cm, which corresponds to a boron doping concentration of 2.6x10^{12} cm^{-3}. There was an oxide layer with a positive charge of 10^{11} cm^{-2} on the top surface, although no isolation structures (p-stop or p-spray) were defined for simplicity of the mesh [7].

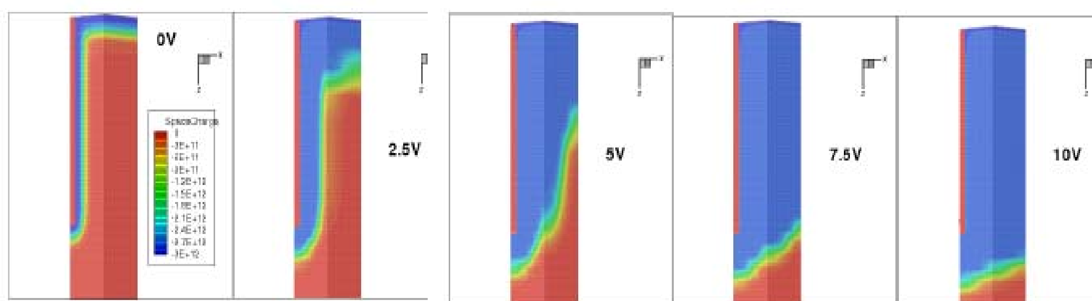

Fig. 3-1 Simulation of the depletion behaviour of a STC-3D detector. The colour red indicates zero and positive space charge, and the spectrum up to blue indicates increasing negative charge. The side of the figure is 40µm, half the distance between two adjacent electrodes. The back p+ contact is not shown.

Figure 3-1 shows the depletion of the simulated device as the voltage difference between the columnar and back plane electrodes is increased. It takes place in two stages: first, the depleted region grows laterally from the n+ electrodes until at 7.5 V the region between the columns is fully depleted, and then progresses like in a planar device towards the back contact. The detector volume is fully depleted at an approximate voltage of 300 V, compared to 500 V for the equivalent planar detector. Naturally, the depletion voltage will vary with doping concentration and substrate thickness.

The measured current-voltage and capacitance-voltage curves from devices similar to those in the above simulation are shown in figures 3-2 and 3-3. Five different designs in the detail of the p-stop ring around the n+ column were fabricated and results from all these are given in the figures. A planar diode was fabricated on the same wafer as the 3D detectors and the results from these devices are shown on the same plots. The IV curves show good behaviour and a similar order of magnitude in leakage current density as to that obtained for the planar device. The CV curve shows two noteworthy points. The first is the higher capacitance for a given bias voltage of the 3D detector with respect to the planar device, which is to be expected. This will lead to a higher noise for a given front-end amplifier. The second point is that there is a distinct kink in the CV curve at 7V, which is also seen in the simulated CV dependence, shown on the same figure. The reason for this change in capacitance is due to the full lateral depletion of the material between columns at this bias voltage.

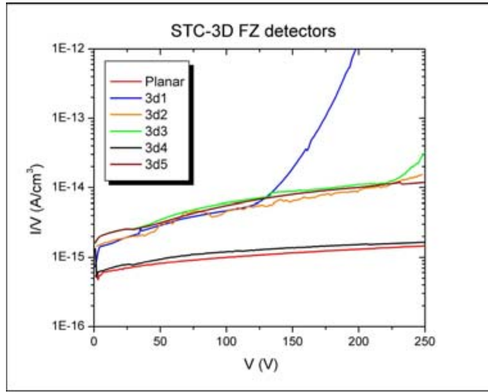

Fig. 3-2 Current-voltage curves of the Float Zone bulk silicon 3D pad detectors. The characteristic of a planar diode fabricated on the same wafer is also shown for reference

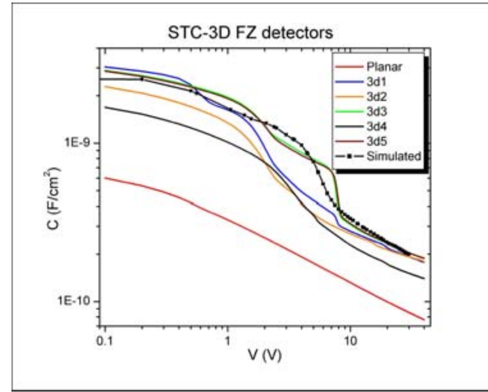

Fig. 3-3 Capacitance-voltage curves of the 3D detectors. The characteristics of a planar diode and of the simulated device are also shown for reference.

7.3.3 Charge collection

Charge collection in the pad devices was also simulated in Glasgow and shown to be relatively slow due to the zero field regions in the centre of four columns where the charge carriers move only by diffusion. According to simulation results, the peak of the pulse produced by an incident particle in this region will arrive to the readout electrode in 2.5 ns, although the complete collection of charge takes 10 ns.

The charge collection efficiency measurements were performed with beta particles from a ^{90}Sr source on a pad 3D-stc device by both the Glasgow (with a shaping time of 500ns) and Florence (with a shaping time of 2.5µs) groups. Figure 3-4 shows the CCE curve for a detector fabricated in MCZ silicon, measured at Glasgow University. The charge collected is normalized to the value expected by an ideal detector 300µm thick, 3.5 fC. Three different stages can be clearly distinguished. At low bias voltages the efficiency increases very rapidly with the applied voltage, due to the fast depletion of the region between columns. The change on the slope of the CCE curve at about 8 V indicates that the volume between the electrodes became completely depleted. This is followed by a second stage where the charge collected increases more slowly with the voltage as the depletion progresses towards the backplane. All the charge generated by the incoming particle is collected for voltages higher than 25 V, which indicates that all the detector volume has reached full depletion. Another interesting feature of these devices is that there is non-zero charge collection at 0V, due to the depleted region already present around the columns in the unbiased device, as can be seen in figure 3-1.

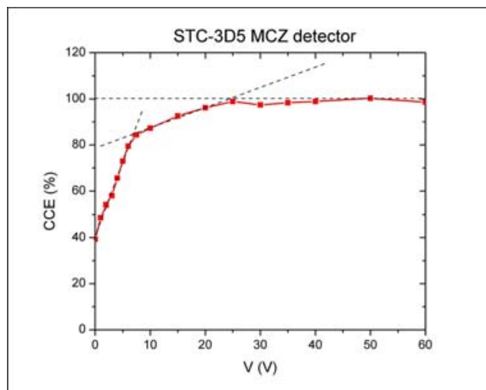

Fig. 3-4 Charge collection efficiency of a 3D-stc pad detector. The substrate is MCZ silicon with a thickness of 300µm.

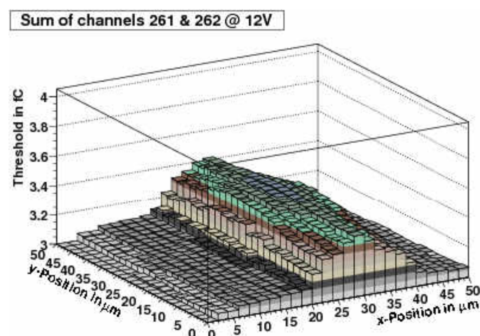

Fig. 3-5 Charge collection measured by the ABCD SCT chip as a function of illumination position. A high threshold corresponds to a low charge collection.

Charge collection measurements, as a response to 2ns duration 982nm wavelength, pulsed laser illumination of short strip 3D-stc detectors has been performed. The detectors were readout with ATLAS SCT binary readout electronics at Freiburg University [8]. The device was assembled into a module using spare ATLAS SCT components from the ATLAS forward SCT construction. To provide good cooling, which is essential for highly irradiated sensors, the sensor was glued into machined slots in the thermo–conducting graphite material used as the thermo-mechanical support of the module. The graphite material is glued to an ATLAS SCT hybrid [9]. For data collection the SCTDAQ software and standard SCT hardware was used. The sensor was connected, via a fan–in, to a binary ABCD3T ASIC [10]. The shaping time of the pre–amplifier is 20 ns and the readout can run with 40MHz. The 3D-stc sensor collects electrons and therefore gives negative signals. The ABCD3T is not fully bipolar and was designed for positive signals as the discriminator only works for positive signals, while the rest of the amplifier front-end is bipolar. Adjusting the ASIC for negative signals is possible by employing the trimming circuit to shift the discriminator offset to its maximal value of around 4fC. The laser was scanned across the device in a direction perpendicular to the strip length. The charge collected on each strip was obtained from threshold scans of the ABCD's discriminator. The signal was negative, as expected, for illumination close to the collecting strip. As the laser illumination point moved to beyond half way between the strips the signal on the collecting strip swapped sign. The signal should be bipolar with an integral equally to zero, but as reported below, the negative component is very slow and therefore not measured by the ABCD electronics. The sum of the charge on the two neighbouring strips should be constant as the laser was scanned from one to the other. However, as can be seen in figure 3-5, the position–resolved IR–Laser measurements indicated low–field regions of approximately 15µm between strips. Significant charge–loss in the vicinity of the p–stop surface isolation scheme was also observed. This could be attributed to the low–field regions and a different surface reflectivity under the p-stops around the holes. Further measurements with different p–stops have to be done and absolute charge collection efficiency measurements with a beta source set–up are planned.

The Santa Cruz group also measured AC-coupled strip sensors with binary readout electronics [11]. The strip devices that they used were the longer 250 column, 2cm long detectors, fabricated on float zone material. The readout electronics had a longer shaping time that the ABCD, equal to 100ns compared to 25ns. The strip detectors response to beta particles was measured, rather than a laser illumination, and a trigger was obtained from a scintillator mounted behind the detector. Both the detection efficiency and the pulse height were measured. The median pulse height corresponds to the 50% efficiency point, and the most probable pulse height is the maximum in the pulse height spectrum constructed by differentiating the efficiency spectrum as a function of discriminator threshold voltage. The detection efficiency is defined as the ratio of the number of in-time coincidences of triggers and strip hits and the number of triggers and is shown in figure 3-6 as a function of bias voltage. As expected, the detection efficiency varies only below approximately 7V where the area between columns is only partially depleted. Note at even at zero bias, the efficiency is not zero, indicating that the region between the columns is partially depleted, as shown in the simulations reported above. For a bias voltage greater than 7 V, the efficiency approaches a value close to 100 %, that is the area between columns is full depleted and the small inefficiency is due to the finite width of the columns.

The collected charge is shown in figure 3-7, which again shows an increase with the bias. Good agreement is found between the median and most probable pulse height of the binary strip measurement. The agreement between the bias dependence of the charge collected on the strips with ~100ns and on the pad with 2.4µs shaping time is good which shows that the change in collected charge above 7V is due to the depletion in the volume under the columns in a planar-diode fashion.

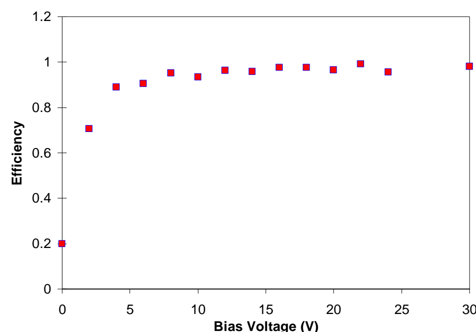

Fig. 3-6 Efficiency measured on a 3D-stc strip detector as a function of bias voltage

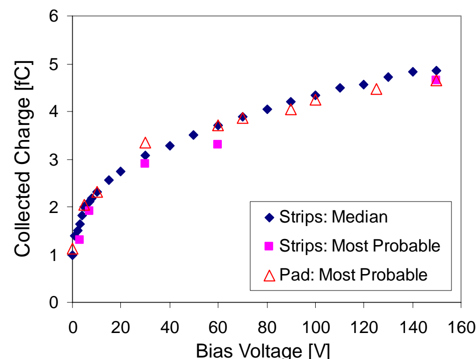

Fig. 3-7 Collected charge as a function of bias voltage for 3D-stc detectors. The strip detector was measured with a shaping time of 100ns and the pad detector with 2.5μs.

7.3.4 Position sensitive TCT measurements

The single column type 3D detectors have area of low electric field as shown above. To understand the effect of the electric field on the charge collection efficiency and collection time a position sensitive TCT experiment was performed on a 3D-stc strip detector. The device is a DC coupled small strip detector fabricated from holes of 10μm in diameter at an 80μm pitch. Each strip consists of 10 columns, and therefore has a length of 800μm. There are 64 strips in the detector. Each hole is phosphorus doped to form an n+ junction in a near intrinsic p-type substrate. To isolate each strip from surface charges, each hole is surrounded on the top surface by a p-type ring. The entire strip detector is surrounded by a guard ring formed from holes connected together. The charge collection in the device is therefore electrons towards the p+ columns on the front side of the device and holes to the uniform back side of the device.

Three adjacent strips were connected to independent fast current amplifiers with a bandwidth of 2GHz. The detector was illuminated by an IR laser with a focused diameter of FWHM of 7mm. The device was mounted in the focal plane of the laser on a xyz stage for focusing and scanning of the detector. The laser was pulsed with duration of 1ns with repetition rate of 100Hz. The detector was biased to beyond the full lateral depletion voltage to 16V. The laser was scanned across the three strip detectors and the signal shape and total charge collected was measured.

Many plots were obtained of the current signals for different illumination positions. The most interesting result is shown in figure 3-8, The induced current has a very fast signal due to the rapid collection of the electron signal on the readout columns. The very much slower component of the signal is due to the slow collection of holes on the back contact of the device. When the beam position is close to the neighbouring strip the signal on the collecting (central) electrode is bipolar as expected from Ramo's theorem. However, due to the very slow hole charge collection, as a result of the shape of the electric field inside the device, the signal has a very large positive fast component and a slow negative component. If LHC speed electronics are used, with shaping time of 25ns, a net positive signal will be observed when a particle deposits charge close to a neighbouring strip.

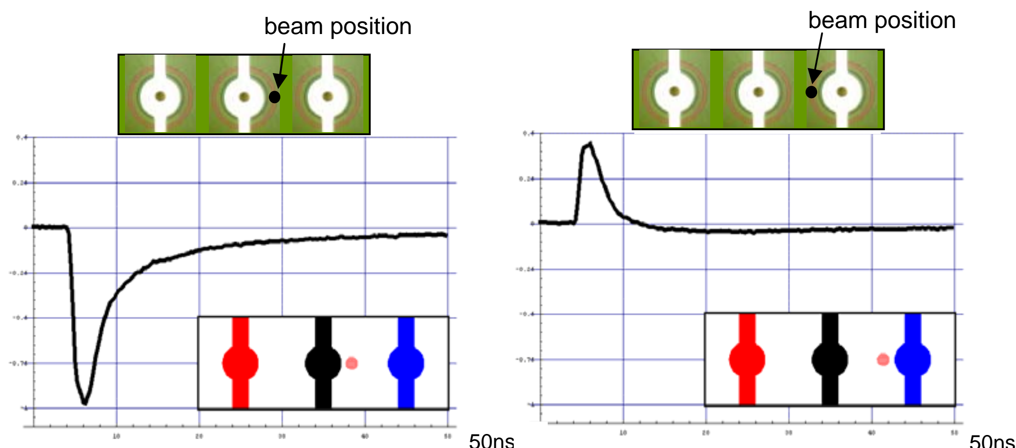

Fig. 3-8. Current signal induced on the central strip as a function of time for two illumination positions: left – close to the collecting electrode; right – close to the neighbouring electrode

7.3.5 Future Work

The measurement of charge collection efficiency and speed of 3D-stc devices after irradiation will be performed. This year the IRST group will fabricate further 3D devices. These 3D detectors will have column types of both n- and p-type to over come the problems on the low field regions. The design will be similar to that under production at CNM which is described below.

7.3.6 Detector design and fabrication at CNM

The first batches of devices fabricated at IRST used holes etched at CNM Barcelona. However, the CNM group also has all the fabrication technologies to make full 3D devices; except wafer bonding which is required for the Stanford technique[12]. The group has proposed a fabrication technique that has columns of both n- and p-type, as expected in a full 3D detector [13]. However, the holes of a given type are etched from one side of the wafer, and those for the other type from the other side of the wafer. Neither set of columns pass through the full thickness of the silicon substrate, as shown in figure 3-9. This structure has a simpler fabrication process, than the Stanford process, because the difficulty of doping the two different kinds of holes on the same side is avoided. In standard 3D detectors very thick layers of polysilicon must be deposited and doped on the same side of the substrate in order to create the p-n junction. By etching the holes on the two sides the photolithographic steps needed to define the readout electrode contacts is only necessary on the top surface. This simplifies the process and avoids thick layers of poly on the surface which can make it difficult to use bump bonding to connect the electrodes to the pixel readout chips. Furthermore, the dead area due to the holes is reduced because, as simulation has shown, there is still a high electric field in the volume on the top or the bottom of the holes. Another advantage of this configuration is that it is not necessary to bond the wafer to a "carrier" to avoid wafer breaking.

The electrical performance of the proposed devices has been simulated with ISE-TCAD at Glasgow University to aid in the design of the device before fabrication started.

A mask set has been designed in collaboration with Glasgow University, for the fabrication of 3D detectors with different geometries which includes: test structures; pad diodes; pixel detectors to be coupled to different readout electronics (Medipix2, Atlas and Pilatus chips); and short and long strip detectors. The strip detectors will be wire-bonded to LHC readout electronics and tested with radioactive sources to demonstrate the functionality of the 3D strip detector at LHC speeds. All the devices will be tested by measuring their electrical characteristics and charge collection efficiency before and after irradiation with protons and neutrons up to fluences of 10^{16} cm^{-2} 1 MeV neutron equivalent.

7.3.7 Fabrication

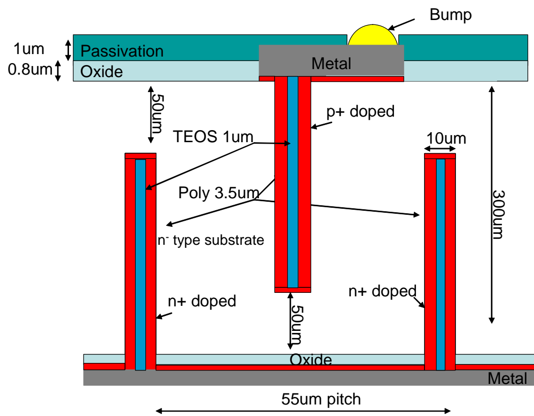

Fig. 3-9 Design of the 3D detectors being fabricated at CNM

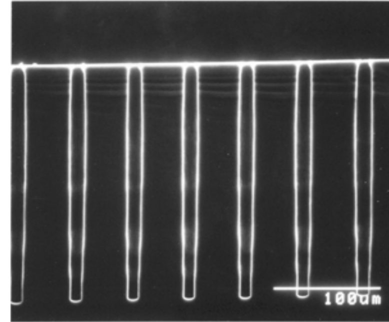

Fig. 3-10 High aspect holes etched in a silicon substrate, the diameter is 10µm and the depth is 250µm.

The processing stages to fabricate the 3D detectors have been investigated and mastered. The etching of cylindrical holes with small diameter, (order 10µm), and large depth (250µm) has been achieved, results from test structures are given below. The holes are partially filled with polysilicon, which is then highly doped to realize the p- or n-type junctions with the near intrinsic substrate material, described below. Finally the surface is passivated with oxide and processed to enable electrical contact to readout electronics.

The holes were etched with an Inductively Coupled Plasma (ICP) in an Alcatel 601-E machine at CNM-IMB. Figure 3-10 shows an example of the high aspect ratio holes fabricated in the silicon substrate. Various hole diameters and thickness have been investigated.

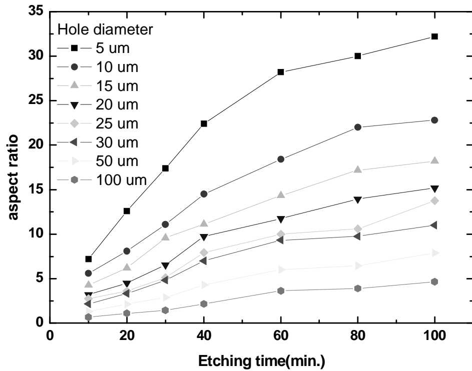

Fig. 3-11 Aspect ratio for different holes diameters as a function of the etching time

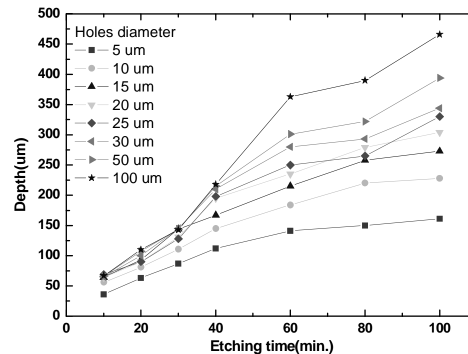

Fig. 3-12 Depth obtained for different hole diameters at different etching times

Figures 3-11 and 3-12 show the different hole aspect ratio and hole depth obtainable for a given hole diameter as a function of etching time. The final diameter chosen for the detectors fabricated is 10µm since a depth of 250µm was achieved after 100 minutes etching. The smallest diameter with the highest depth should be used in order to insure the smallest dead area (or low detection efficiency area as it has been recently demonstrated [14]) and the highest signal-to-noise ratio. The 5µm diameter hole would be a good choice but the hole depth saturates after 80 minutes at 150µm, which is insufficient. The deeper the hole is etched the more difficult it is for the etchant to etch the bottom of the hole. This effect becomes stronger and stronger until the etching of the bottom of holes stops and sidewalls are etched enlarging the diameter.

The electrodes within the dry etched holes were formed by partially filling the hole with a thick polysilicon layer and doping it with boron and phosphorus to create p-i-n diodes. The final doping profiles of boron and phosphorus were simulated using ISE-TCAD software package. Figure 3-13 shows a comparison of the simulated and measured boron profile at the end of the fabrication process.

The profile was measured on the top surface of a test wafer with a doping concentration of 10^{15} cm^{-3} while the simulation was performed using an high resistivity wafer which will be used for the real devices. The graph shows that the concentration of boron in the polysilicon layer is almost saturated insuring a low resistivity contact and that the junction is formed at a distance of about 2μm into the silicon substrate.

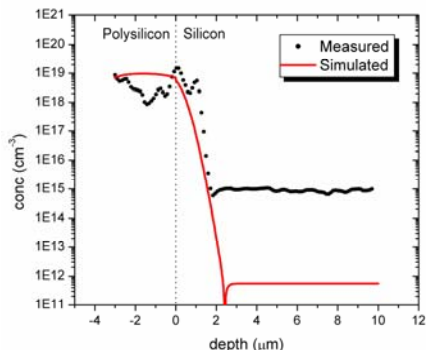

Fig. 3-13 Simulated and measured boron profile of the p+ electrodes. The substrate used for the measurement of the doping profile was low resistivity.

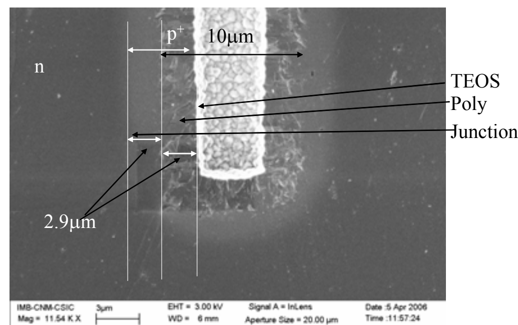

Fig. 3-14 SEM image of the doped polysilicon deposited in a bottom of a 10μm diameter, 250μm deep hole. The white material deposited on the surface of the polysilicon layer is a 200 nm layer of TEOS.

The concentration of the boron dopant was indirectly measured inside the holes by Scanning Electron Microscope (SEM) imaging. Figure 3-14 shows the bottom part of a 10μm diameter hole 250μm deep doped with boron through a 3μm thick layer of polysilicon and passivated with TEOS. The image shows the fine grain of the polysilicon layer and the halo of the boron diffusion into a high resistivity n-type silicon substrate. The junction is formed at about 2.9μm from the polysilicon/silicon interface in good agreement with the simulated result. Therefore it can be assumed that the doping profile is uniform along the hole depth. Another important aspect of the doping profile is that diffusion smoothes the corner of the column at the bottom part of the hole, which reduces the risk of early breakdown in real devices.

The polysilicon layer deposited on the surface of the detector was removed by patterning the substrate surface with a thick photo-resist layer and then was etched by using the same dry etching process used for the formation of the holes into the silicon substrate. The surface of the wafer was passivated with a thin layer of SiO_2 for protection from diffusion.

The contacts are formed by depositing an Al layer on the doped polysilicon layer and different bump bonding techniques will be used to connect the various detector configurations to the corresponding read out chips.

7.3.8 Simulation

The proposed devices have been fabricated using the simulation package ISE-TCAD to simulate the electrical characteristics and the technological properties of the 3D detectors in order to find the optimum parameters for the definition of the detector geometry and the fabrication parameters [15]. In order to keep the size of the simulated mesh as small as possible the device's symmetry was exploited, as discussed above, as shown in figure 3-15. The p+ column has a pitch of 55μm on a square pitch with the n+ hole at the centre; the substrate used was p-type since this is of more interest for radiation hard devices.

The simulated capacitance of the column falls rapidly with increasing voltage as the device depletes. The capacitance saturates at about 8 V to a value of 55 fC per column. The coaxial cable approximation, which regards the column as being a coaxial cable with radius equal to the distance between n+ and p+ electrodes, predicts a value of between 65 fC and 81 fC (as the "cable length" can either be considered as the 250μm column length or the 200μm overlap region).

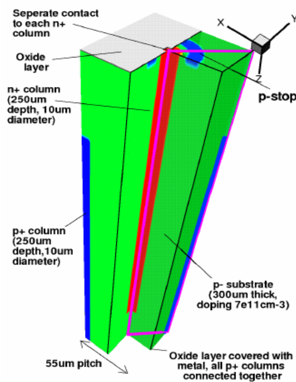

Fig. 3-15 Layout of the simulated device using ISE-TCAD software package.

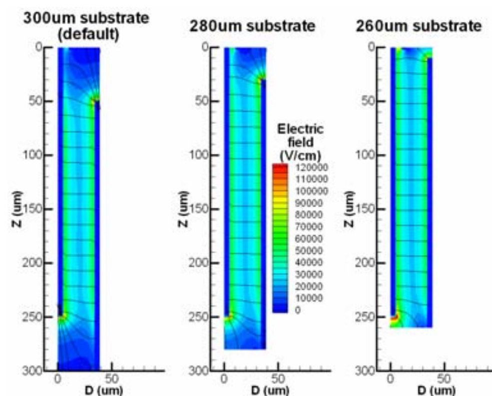

Fig. 3-16 Electric field distribution in double sided 3D detectors with different substrate thicknesses.

In order to understand the electric field distribution in the detectors three simulations were made using 300µm, 280µm and 260µm thick substrates. The column length in each of these simulations was 250µm. Figure 3-16 shows the electric field at a bias of 100 V. In the 300µm device, a region that has a field strength about 5 times smaller than the minimum value in the region between the columns, (5 kV/cm compared to 20 kV/cm), extends about 20µm from the surface at the top and bottom of the device. When the substrate thickness is reduced to 260µm, the low-field region disappears and the detector behaves as a standard 3D detector.

7.3.9 Future Work

Future work will concentrate on the finishing of the fabrication of these devices. The wafers will be diced, bump-bonded as required, and distributed to RD50 collaborator for electrical and charge collection characterization with discrete amplifiers and ASICs, including LHC speed devices.

7.3.10 Work done at New Mexico University on devices from Stanford

New Mexico joined RD50 recently. They are an active part of the new structures group presenting their work on 3D detectors fabricated at Stanford University by S. Parker et al.[12]. The devices tested to date are early full 3D detectors with electrodes of diameter of 17µm, and length of 121µm. The array consists of n-type columns arranged rectangularly; with a pitch of 200µm in one direction and 100µm in the other. A p-type column is situated at the centre of the n-type columns. This basic structure is repeated to form an array. Most of the same type columns are connected together in columns to facilitate biasing. Some electrodes are left isolated to allow individual connection, via a probe station, for testing. The devices have been tested electrically with the use of a pico-probe. Devices have been tested before irradiation and after $1x10^{14}$, $2x10^{14}$ and $1x10^{15}$ 55-MeV protons/cm^2.

The device full depletion voltage has been determined from CV measurements and charge collection measurements from IR laser illumination, shown in figure 3-17. The full depletion voltage increased from 15V before irradiation to 130V after full irradiation. The electrode capacitance, as a function of irradiation, has been measured to be approximately 90fF for the p-type electrode, figure 3-18 illustrates the capacitance as a function of bias voltage for a p-type electrode. This has been shown to be a function of temperature, and measurement frequency after irradiation, as expected. The rise time of the signal measured as a response to illumination from an IR laser, with duration of 0.3ns, was only 2ns before irradiation, which reduced to 1.5ns after $1x10^{15}$ 55-MeV protons/cm^2.

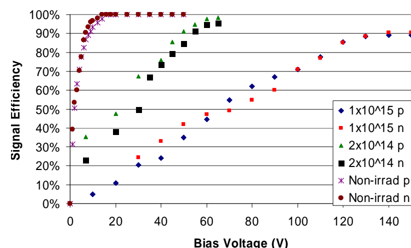

Fig. 3-17 The array depletion measured from signal efficiency (pulse height relative to the maximum for the non-irradiated device), for charge collected at either the n- or p-type electrode, as a function of bias voltage, for three 55-MeV proton fluences.

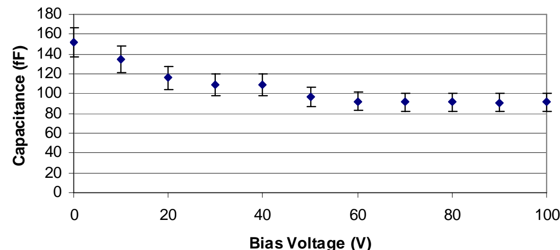

Fig. 3-18 The capacitance of a p-type electrode after an irradiation to fluence of $2x10^{14}$ 55-MeV p/cm^2.

TCAD simulations of the devices are being developed by the New Mexico group to explain the measurements. Future work will concentrate on further charge collection measurements to map the charge collection efficiency and speed as a function of charge generation for non- and irradiated devices as well as the development of their TCAD simulations.

7.3.11 Commercial development of 3D devices at IceMOS technology

A commercial development has begun with the semiconductor fabrication company IceMOS Technology, based in Northern Ireland. The company has a demonstrated expertise in all the necessary steps to fabricate 3D silicon detectors. The University of Glasgow group and Diamond have entered into a commercial development programme with IceMos Technology to make full 3D detectors. The masks have been designed and written at Glasgow University in close collaboration with the company. The company has produced the first set of test structures of 3D holes ready for doping and filling with polysilicon. The first full test structures are expected by the end of Q1 07. These will be tested electrically and as a detector at Glasgow University. The wafer design for the second phase with pixel and strip detectors is near completion and will be ready for fabrication to start as soon as the tests on the first trails are complete.

7.4 References

[1] G. Lindström et al., Nucl. Instr. and Meth. A 466 (2001) 308-326
[2] M. Moll et al., Nucl. Instr. and Meth. B 186 (2002) 100-110
[3] G. Kramberger. et al., Nucl. Instr. and Meth. A 554 (2005) 212-219
[4] E. Fretwurst et al., Nucl. Instr. and Meth. A 552 (2005) 124-130
[5] C. Piemonte et al., Nucl. Instr. Meth. A 541 (2005) 441
[6] S. Ronchin et al., “Fabrication of 3D detectors with columnar electrodes of the same doping type” presented at PSD 07 Liverpool September 2005, to appear in Nucl. Instr. Meth. A
[7] C. Fleta et al., “Simulation and test of 3D silicon radiation detectors” presented at 6th Hiroshima conference November 2006, to appear in Nucl. Inst. Meth. A.
[8] U. Parzefall et al., “Characterisation of a 3D-stc p-type prototype module read out with ATLAS SCT electronics” to be presented at the 11th Vienna conference on instrumentation, Feb 2007, to be published in Nucl. Instr. Meth. A
[9] A. Abdesselam et al., ATL-INDET-PUB-2006-007, 2006
[10] F. Campabadal et al., Nucl. Instr. and Meth. A 552 (2005) 292.
[11] M. Scaringella et al., “Charge Collection Measurements in single-type column 3D Sensors”, presented at 6th Hiroshima conference November 2006, to appear in Nucl. Inst. Meth. A.
[12] C. Kenney, S. Parker, “Silicon detectors with 3D electrode arrays: fabrication and initial test result”, IEEE Trans. Nucl. Sci. NS-46(4) (1999) 1224.
[13] G. Pellegrini et al., “Double Sided 3D Detector Technologies at CNM-IMB” presented at the 2006 NSS-MIC Oct 2006, to be published in IEEE Trans. Nucl. Sci.

[14] C. DaVia et al. “Radiation hardness properties of 3D active edge silicon detectors” to be published in Nuclear Instruments and Methods in Physics Research A.
[15] D. Pennicard et al., “Simulation Results from Double Sided 3D Detectors”, presented at the 2006 NSS-MIC Oct 2006, to be published in IEEE Trans. Nucl. Sci.

8 Full detector systems

8.1 Non inverting silicon materials

It is now well accepted [1-5] that reading-out finely segmented silicon detectors from the side were the high electric field is located after irradiation gives the major contribution to radiation hardness. This is due to the fact that charge trapping is the main cause of charge collection deficit, because it reduces the lifetime of charge carriers and therefore their collection distance. The typical trapping time (τ_{tr}) is inversely proportional to the irradiation fluence [6]. The signal is reduced, in a first approximation, by a factor $\exp(\tau_{tr}/t_c)$, where t_c is the collection time. Short collection times are required to maximize the charge collection. Traditional p-in-n detectors suffer from the migration of the junction to the backplane after irradiation (the space charge type inversion), with the high electric field being located on the non-segmented side of the device. The development and test of non-inverting silicon materials, where the high electric field is always located on the segmented side of the detector, has been the main subject of the FDS project during the last year. The candidates as non-inverting silicon materials are p-type substrates (both FZ and MCZ) and n-type MCZ, although this latter has been shown to invert after high dose of neutron irradiation [7].

8.1.1 Charge collection efficiency measurements with p-type microstrip detectors in diode configuration

In order to evaluate the radiation damage four microstrip detectors have been irradiated with neutrons at the TRIGA Mark II reactor in Ljubljana to different fluences: 10^{14}, 10^{15}, $2x10^{15}$ and 10^{16} n/cm^2. The connections to the strips for the signal acquisition and the ground are made by wire bonding. The bias voltage is supplied through the back-plane while the strips are grounded. In our setup, all strips are shorted together.

Figure 8-1 [8] shows the charge collection versus voltage plots for 4 irradiated detectors. The sensor signal is averaged over a large number of triggers and the charge is computed as the integral of the average waveform of the signal. For the detector irradiated to 10^{14} neutrons/cm^2 the plot exhibits a plateau, with a kink in the curve at ~400V. On the contrary after greater fluences the curves do not show any plateau and the signal keeps growing with the bias voltage. The absolute values of the signal depend on environmental factors, laser focusing, incidence angle and reflections in the aluminium of the strips.

Figure 8-2 [9] shows a compilation of various measurements made with a similar set of irradiated detectors and characterised using a β^- source (^{90}Sr source) and an infrared laser. The laser has been used to extend the measurements at various bias voltages, and the absolute scaling of the collected charge was performed by interpolation with the measurements with mip particles.

It can be noticed that even after the highest dose, corresponding to the anticipated dose for the innermost pixel layer at SLHC, the collected charge exceeds 4000e$^-$ at 1000V bias voltage.

8.2 Electrical characterization of test structures and miniature microstrip detectors before and after gamma irradiation

When n-side read-out is used on segmented detectors, as for example in n-in-p or n-in-n geometries, a method for interstrip isolation has to be used. Possible interstrip isolation methods are p-spray , p-stops or a combination of the two (moderated p-spray). It is important to study the effects of these techniques on electrical properties of the silicon detectors, like the interstrip capacitance (ISC), the interstrip isolation, measured as inter-strip resistance (ISR), the break-down voltage (V_{BD}) and the leakage current.

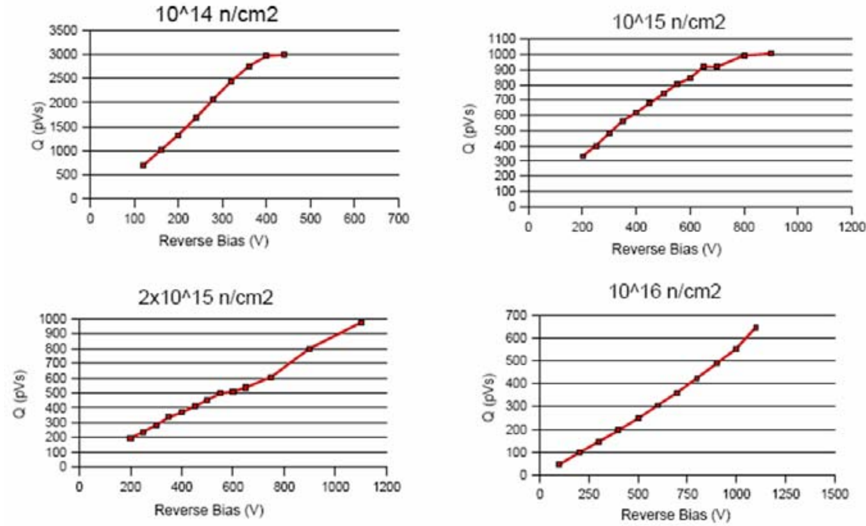

Fig. 4-1 Collected Charge-Voltage plots of n-in-p microstrip detectors irradiated with neutrons for different fluences [8]. The read-out strips were all bonded to a common metal line (diode configuration) and read out with a large bandwidth single channel current amplifier.

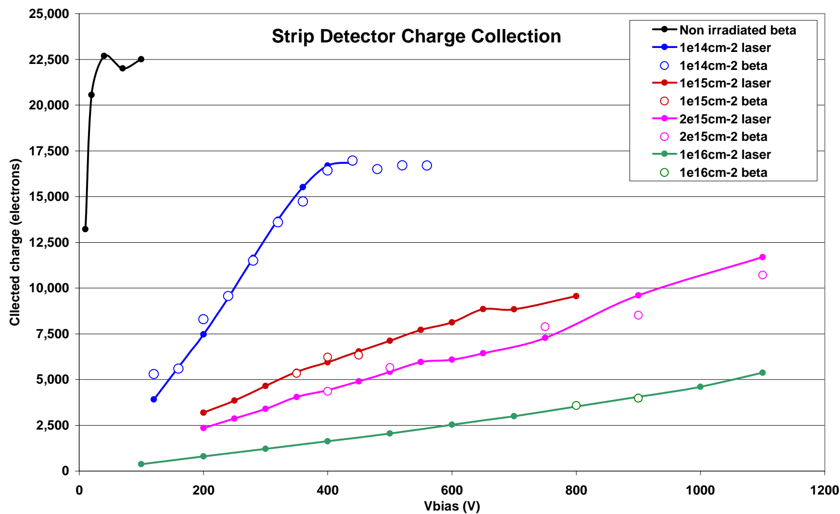

Fig.8-2. Collected Charge-Voltage plots of n-in-p microstrip detectors irradiated with neutrons for different fluences [9]. Signal induced by fast electrons (^{90}Sr) and laser [6]. Measurements performed in diode configuration.

A set of test structures for this type of characterization before and after irradiation has been implemented in the SMART [10] mask. These structures include short strip detectors of varying strip width and pitch, circular MOS capacitors with aluminum top electrode, and capacitance test structures.

The test structures for ISC (Inter Strip Capacitance) measurements are comprised of 9 AC coupled strips, of which the inner-most three allow the measurement of the interstrip capacitance from the central strip to its pair of next neighbors, and the outer three strips on each side are connected together to allow bonded connections to a shield (the bias ring can be used to this purpose).

Similar measurements (ISC, ISR, V_{BD}) have also been performed on miniature (4.45 cm long) microstrip detectors processed on the same mask set.

This study [11] was target to the changes of the electrical properties due to oxide damage after irradiation. The irradiations were performed in the UC Santa Cruz ^{60}Co source in steps of

approximately 70 krad, corresponding to one day irradiation at a dose rate of 3.15 kRad/hr. The parts were irradiated with their electrical terminals floating. After irradiation the devices were stored at room temperature and the time between irradiations and measurement could vary by a few days. The annealing is shown in the graphs as double-valued parameters for the same dose. A more thorough annealing was performed at the end of the irradiation, lasting for one week at room temperature and two weeks at 60°C.

8.2.1 Capacitance vs voltage (C-V) and ISC measurements

Frequency dependent C-V characterizations using an HP 8241 LCR meter were performed before the irradiation, and within a few days after each step. At the end, the capacitance-voltage (C-V) data at 10kHz were analyzed for the MOS capacitors, while the interstrip capacitances (Cint-V) were analyzed at the highest frequency, e.g. 800 kHz or 1 MHz.

The bias dependence of currents and ISC could be determined before irradiation only in a restricted interval of applied bias voltage because of breakdown which occurred in some cases before depletion. In fact, before irradiation, detectors with high-dose p-spray isolation had a breakdown voltage in the 50-150V range, depending on the width/pitch value. A considerable increase in breakdown voltage after irradiation can be observed (see below).

The ISR was determined with a 2 probe measurement using an HP 4145 Semiconductor Analyzer. One SMU biased the detector to 50V, the bias ring was set to ground, the current I_1 on one strip was determined by measuring the potential across the biasing resistor of 600kΩ and the voltage on its two next neighbors V_2 was swept with a second SMU from -5 to +5V. The interstrip resistance is then $R_{int} = 2*\Delta V_2/\Delta I_1$.

The results from capacitance measurements on test structures show a saturation trend similar to the MOS capacitors (Figs. 8-3 and 8-4). The irradiation drastically reduces the ISC for p-type detectors, and the interstrip capaciatance geometrical value is approached as the voltage is increased. This result is in good agreement with simulation predictions, and is due to the depletion region widening inside the p-spray at the surface [12]. Saturation is reached at a dose between 70 and 150 kRad. The wafer with low-dose p-spray isolation reaches the saturation already with 70 kRad, with very little residual voltage dependence of the interstrip capacitance. The n-type test structures (processed on Si with <111> orientation) show increased interstrip capacitance with increased dose, while the p-type test structures (processed on <100> wafers) exhibit reduced interstrip capacitance. There is no dependence of wafer type, i.e. MCz and FZ behave exactly the same, separately for high and low p-spray dose, respectively. The amount of annealing is very limited.

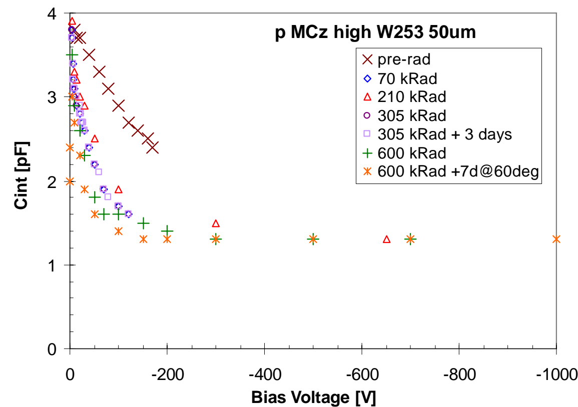

Fig. 8-3 Interstrip capacitance of the 50 µm pitch test structures as a function of the total dose for p-type MCz high-dose wafers. The remaining p-type test structures behave the same way, including the absence of strong annealing effects [11].

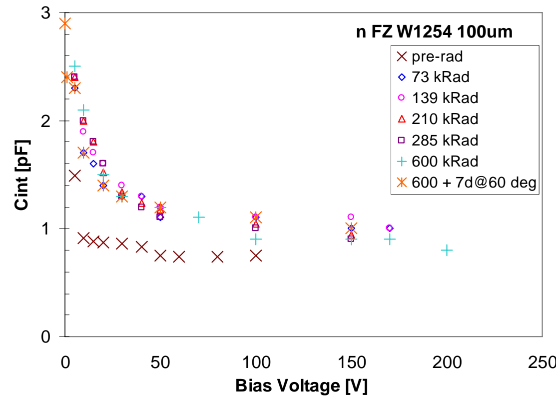

Fig. 8-4 Interstrip capacitance of the 100 µm pitch test structures as a function of the total dose for the n-type FZ wafer. Saturation is seen at about 100 kRad, and annealing is limited [11].

The same trends are seen with the mini silicon detectors (with 4.45 cm strip length). Figure 8-5 compares the interstrip capacitance vs. bias voltage for two p-type wafer types (MCz and FZ) and two p-spray doses. There is no difference between MCz and FZ, but large differences due to the surface treatment, i.e. between low- and high-dose p-spray.

The interstrip resistance was measured before irradiation (pre-rad) and after radiation and annealing. A value in excess of $10^{10}\Omega$ was measured pre-rad and post-rad for the 1.15 cm long test structures, for all wafers and surface treatments.

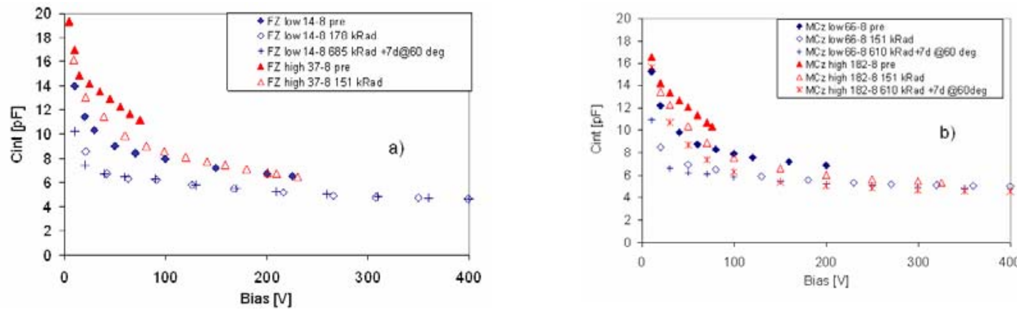

Fig. 8-5 Comparison of the interstrip capacitance of the 100 µm pitch mini-SSDs, pre-rad and after saturation a) FZ (wafers 14 and 37), b) MCz (wafers 66 and 182) [11]. There is a small difference between different wafers, but a large dependence on the p-spray dose. Saturation below 150 kRad and only limited annealing are observed.

8.2.2 Oxide charge build-up

The effect of irradiation to the oxide charge, namely the build-up of a radiation induced fixed positive charge, was evaluated from flat-band voltage measurements on the MOS capacitors.

The results are shown in Figure 8-6. Saturation is observed after about 150 kRad for all measured devices regardless of the bulk material. The charged trapped in the oxide reaches similar value for all p-type devices (~1.5 10^{12} cm^{-2}) while an higher value has been observed for Fz n-type (~2 10^{12} cm^{-2}). This difference is expected since the Fz n-type wafers were oriented <111> while the p-type wafers were <100>. Annealing reduces the effect during the irradiation process and after the elevated temperature annealing. Saturation is visible after the third annealing step. Such a strong annealing effect has been observed before on MOS structures processed at ITC-irst and irradiated with X-rays [13].

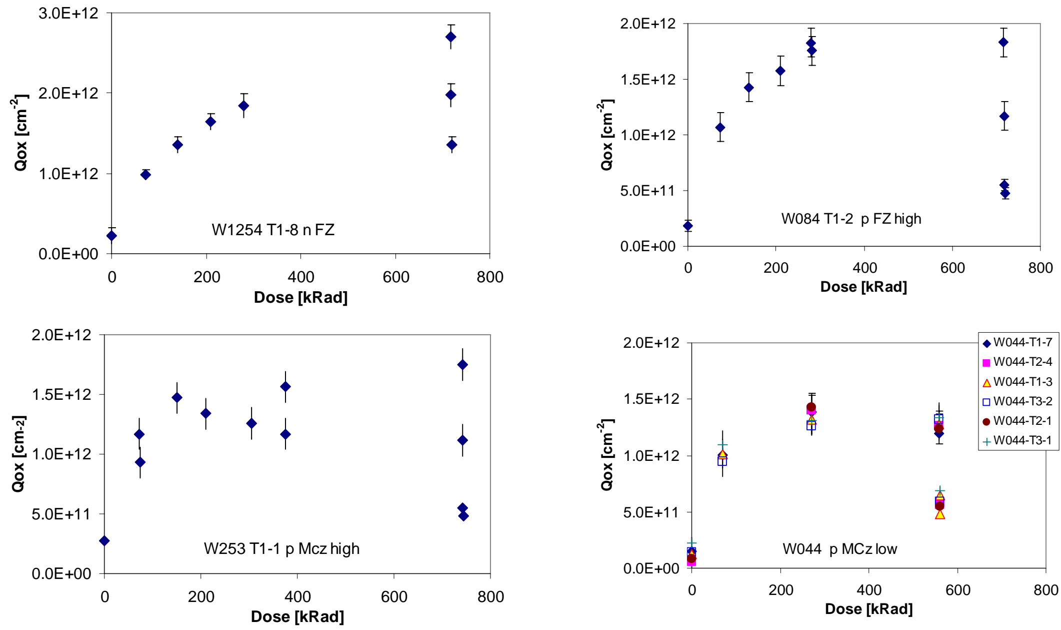

Fig. 8-6 Effect of the total dose on the oxide charge for four different wafers: a) n-type FZ b) p-type FZ high-dose, c) p-type MCz high-dose, d) p-type MCz low-dose [11]. Data at the same dose indicate annealing. For the largest dose point, the highest value is right after irradiation, the second highest right after one week of room temperature annealing and the third and fourth highest each after an additional one week annealing at 60 ^{o}C, respectively.

8.2.3 Reverse current vs voltage (I-V) measurements

The current – voltage (I-V) curves at different doses shown in Fig. 8-7 reveal an improved performance in breakdown voltage after irradiation. In fact, before irradiation, detectors with high-dose p-spray isolation had a breakdown voltage in the 50-150V range, depending on the width/pitch value. After a dose of 210 kRad a much larger reverse bias, up to 500 V, can be applied without the risk of breakdown for all the devices regardless of the strip geometry. Large annealing effects lower the breakdown voltage again at intermediate irradiation steps and at the post-radiation elevated annealing step. Table 8.1 shows the breakdown voltage at several steps in the irradiation campaign. Wafers were implant isolation has been done with high p-spray implantation dose seem to exhibit worse annealing of the breakdown performance.

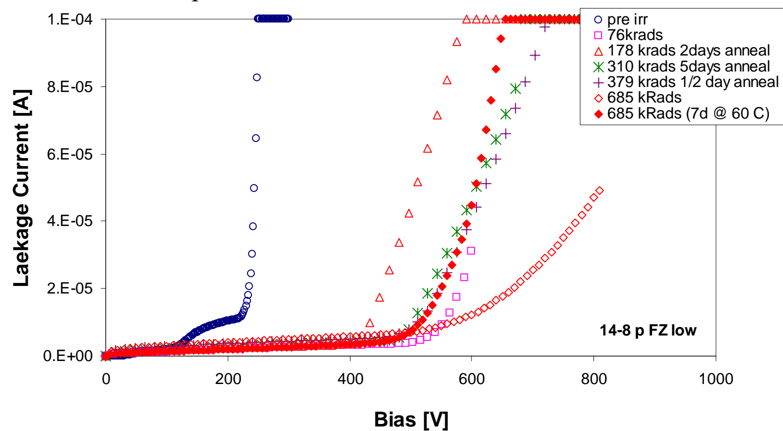

Fig.8-7. Leakage current – voltage (I-V) curves for several irradiation steps. The breakdown voltage is increased considerably with increased dose.

Table 8.1: Breakdown voltage

Device	Breakdown Voltage [V]				
	pre-rad	75 kRad	300 kRad	~650 kRad	~650 kRad +7d @60 °C
66-8 p MCz low	250	550	900		
182-8 p MCz high	70	>200	350	>1000	500
14-8 p FZ low	240	600	600	700	600
37-8 p FZ high	70	200	300		

8.2.4 Conclusions

The investigation of surface effects showed no dependence on the p-type wafer type (FZ vs. MCz), but large dependence on the surface treatment (high vs, low p-spray dose).

Saturation was observed for the interstrip capacitance at about 100 kRad, with very little annealing.

The flatband voltage and the oxide charge showed also saturation at about 150 kRad, but in addition a very large annealing by a factor 3.

The breakdown voltage was increased by the gamma irradiation, but also showed very strong annealing. The strips showed good isolation before and after irradiation and annealing.

8.3 P-spray isolation studies in CNM-Barcelona

8.3.1 Blanket p-spray

The blanket p-spray consists of a uniform p-type implant performed on the silicon surface as shown in Figure 8-8. The p-pray dose needs to be optimised for best performances in term of strip insulation, low reverse currents and high breakdown voltages. The optimal technological options for the p-spray implant were found for the fabrication of n-in-p detectors by using a simulation software package and dedicated calibration runs [14,15]. Test structures were also processed together with the detectors in order to measure the inter-strip resistance and capacitance. MOS capacitors were used to estimate the surface oxide charge density introduced during the fabrication process and after irradiation. The detectors were irradiated with gamma particles to a dose of 50 Mrad which is the total dose expected in the middle region of the future upgrade of the Atlas CERN experiment.

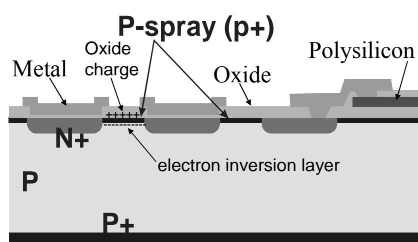

Fig.8-8. Cross section of a microstrip AC biased n-on-p detector with p-spray insulation.

The optimum p-spray dose is the minimum dose that ensures a good insulation among the strips before and after irradiation. Lower p-spray doses allow in fact achieving higher breakdown voltages. Figure 8-9 shows the simulated breakdown voltage of a p-type strip detector versus the total charge implanted with the p-spray into the silicon bulk. The simulation covers the range of implantation energy from 25 to 150 keV and the total doses from 10^{12} to 8×10^{12} cm^{-2}. The breakdown voltage is a function of the total implanted charge, which depends on both the energy and dose, but not from the depth of the profile, at least in the range of energy and doses simulated. It is possible to observe the drastic reduction in the V_{BD} as the density of the p-spray implanted total charge increases. At a fixed polarisation bias the electric filed is higher when the gradient of the doping concentration at the interface between the strip and the p-spray increases, leading to an early breakdown of the devices.

The parameters of the p-spray implantations were: ion energy 45 keV with doses of 10^{12} and $5\text{x}10^{12}$ cm^{-2}, and ion energy 150 keV with a dose of 10^{12} cm^{-2}. The minimum doses available at the ion

implanter at the CNM facilities which insure a uniform implantation on the wafer surface is $1x10^{12}$ cm^{-2}. According to simulation, all three implant profiles are able to compensate the electron inversion layer induced at the silicon surface. Figure 8-10 shows the p-spray profiles obtained with the fabrication and measured by the spreading resistance method. The results are compared to the expected profiles simulated with the ISE-TCAD software package. In all cases the total implanted dose is lower than the predicted by the simulations.

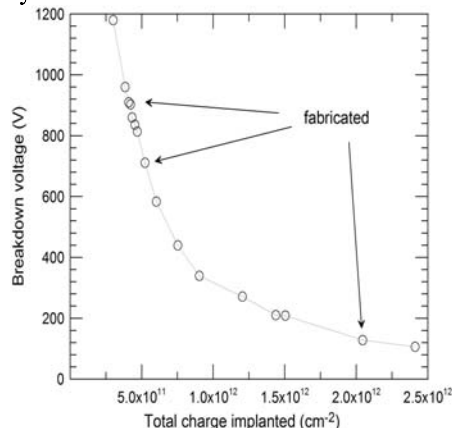

Fig.8-9. Variation of the breakdown voltage as a function of the total implanted charge for the definition of the p-spray insulation in no-irradiated detectors.

The fabricated detectors were characterized by reverse current and capacitance measurements. The average full depletion voltage was V_{FD} = 41±3 V, while the leakage current density for the microstrip devices at V_{FD}+20V was 50 nA/cm^2.

The current-voltage characteristics of the p-type pad detectors fabricated with the three different p-spray implants before irradiation show that the breakdown voltage (V_{BD}) decreases with the increasing of the total implanted dose as predicted by simulation, as can be seen in Table 8.2, which shows the average V_{BD} for simple diodes fabricated with the three technologies. It must be noticed that in some case the experimental value of V_{BD} is higher because the total dose implanted is lower than the dose expected by simulation.

The average leakage current of the strips and the guard rings measured at V_{FD}+20 V are reported in Table 8.3. The leakage current of the guard ring of the detectors with the p-spray doses of $10^{12}cm^{-2}$ are few order of magnitude higher that the central active area, which means that the insulation between the surface and the backplane is not adequate, there is a conductor electron channel between the guard ring and the back contact trough the detector rim. The characteristic of the detector with the highest p-spray implanted dose (ion energy 10^{12} keV and dose $5x10^{12}$ cm^{-2}) show a guard ring leakage current lower than the central active area. This indicates that the strips are properly insulated and the corresponding V_{BD} is lower enough to full deplete the detectors before irradiation.

Table 8.2: Breakdown Voltages

Technology	V_{BD}(V)	Std. error (V)
p-stop	400	± 15
p-spray	460	± 30
Moderate (228 nm)	370	± 40
Moderate (260 nm)	530	± 10
Moderate (290 nm)	310	± 10

Table 8.3: Reverse current at full depletion voltage +20 V of the strip detectors fabricated with the different p-spray insulations. The currents are measured at 20ºC.

p-spray		Current at V_{FD}+20 V	
Energy (keV)	Dose (cm^{-2})	Strips	Ring
45	10^{12}	50 ± 30 nA	2 ± 1 mA
150	10^{12}	90 ± 40 nA	150 ± 40 µA
45	5×10^{12}	1.4 ± 1.1 µA	300 ± 30 nA

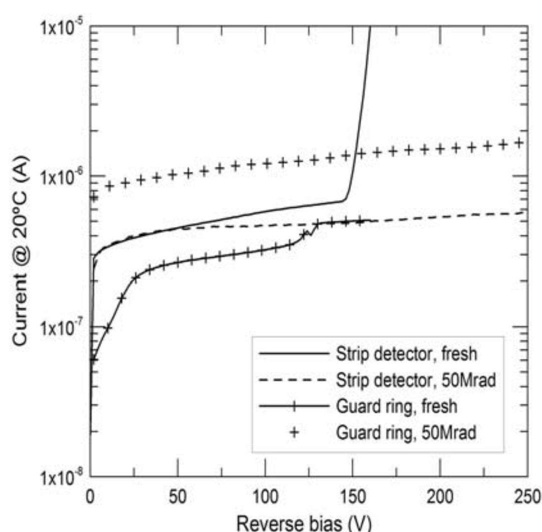

Fig.8-10. Comparison of the current-voltage characteristics of irradiated and not-irradiated n-in-p strip detectors fabricated with the p-spray implant energy of 45 keV and dose of $5x10^{12}$ cm^{-2}.

In order to prove the effectiveness of the p-spray insulation between the strips, some detectors were irradiated with gamma ray from a ^{60}Co source to a dose of 50 Mrad (50kGy). Figure 8-10 shows the current-voltage characteristic of the detector fabricated with the highest dose ($5x10^{12}cm^{-2}$) and irradiated with gamma particles. As expected the effect of the radiation is to increase the leakage current that flues through the guard ring due to the increasing of the electron layer at the silicon/oxide interface. However, it must be noticed that the current of the strips does not change significantly which indicates that the p-spray is still adequate to guarantee a proper insulation even at the saturation of the oxide charge density. Furthermore, the reverse current measurement shows that the breakdown voltage of the p-spray implant with the highest dose improves after the irradiation. This can be explained because the maximum electric field decreases with the increasing of oxide charge density due to compensation of the acceptor dopants by the oxide charge. The characteristics of the detectors with the lower implants are not reported because they have very high levels of leakage currents.

8.3.2 Moderated p-spray: simulation and results at CNM

The moderated p-spray technique is potentially the best option among the other possible interstrip isolation methods, namely p-stop and blanket p-spray techniques. The challenge is the optimization of

the isolation method keeping high breakdown voltages, high microdischarge voltage threshold and maintaining good strip isolation. The moderated p-spray combines the p-stop and p-spray together in one single implantation through an oxide layer with different thicknesses. The region implanted trough the thinner oxide is referred as the p-stop which insures a good isolation between the active area and the guard ring (and/or between neighboring strips) while the rest of the wafer is implanted at the same time trough a thicker oxide layer (referred as p-spray region). The p-spray is necessary to reduce the electric field at the edge of the p-stop, thus decreasing the probability of microdischarges. The moderated p-spray as originally proposed ([16]) uses a silicon nitride layer deposited on the top of an oxide layer. The method proposed in this study simplifies the original idea by using only one oxide layer but with different thicknesses (Fig. 8-11). The initial technological simulation was done to optimize the process and to find the optimum profile to fabricate a working n-on-p radiation detector. Both the technological and electrical simulation was performed using the ISE-TCAD v9 software package. Detectors were fabricated and characterized before and after a gamma irradiation of 50 Mrad.

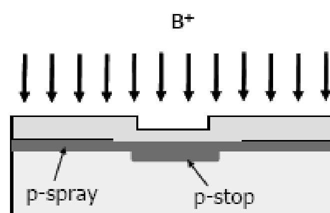

Fig.8-11. Schematic of the moderate p-spray implant trough the two different oxide thicknesses.

Various silicon wafers were processed in order to confirm the results obtained by simulation. Three moderate p-spray profiles (228, 260 and 290 nm) were selected for fabrication, corresponding to the three simulated oxide thickness. It must be noticed that the detector with the lowest thickness of oxide have the higher concentration of boron in the p-spray area. All the three configurations have the same p-stop profile. For comparison a wafer with only p-stop and another with only p-spray isolation were processed at the same time.

The mask set used for the fabrication was designed by CNM and contains pads detector and test structure to measure the interstrip resistance, MOS capacitor to measure the oxide charge densities and test structures for spreading resistance measurements. The pad detectors are 0.5×0.5 cm2 with a biased guard ring 100 μm wide surrounded by a multi-guard rings structure with field plates. The wafers were <100> FZ p-type from Siltronic, with a thickness of 300 ± 15 μm and nominal resistivity of 20-30 kΩ×cm. The full depletion voltage over a whole wafer is 34 ± 8 V, in agreement with the declared resistivity. The Current-Voltage characteristics for the pads detectors isolated with the five different technologies are shown in Figure 8-12 and compared with simulation. The surface damage due to the p-spray blanket usually leads to higher leakage currents before irradiation for the samples with only p-spray or moderate p-spray as the simulation shown in the same figure.

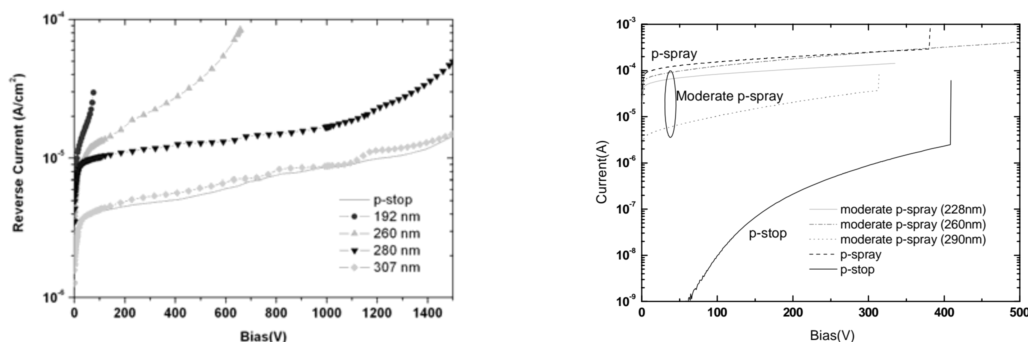

Fig.8-12. Current voltage characteristics for the different technologies: simulation (left) and measurement (right).

The average measured breakdown voltages, reported in Table 8.2, are lower than the predicted by the simulation, but all the devices can be fully depleted and thus their operation as radiation detectors is possible.

Dedicated test structures were designed to measure the interstrip resistance before and after gamma irradiation in order to prove the reliability of the isolation techniques of the n-on-p detectors. The average interstrip resistances are reported in figure 8-13. These values were measured at room temperature and at zero bias, so they are a conservative estimation of the value that would have a depleted detector, and ensures an adequate insulation of the microstrips at least for non irradiated devices.

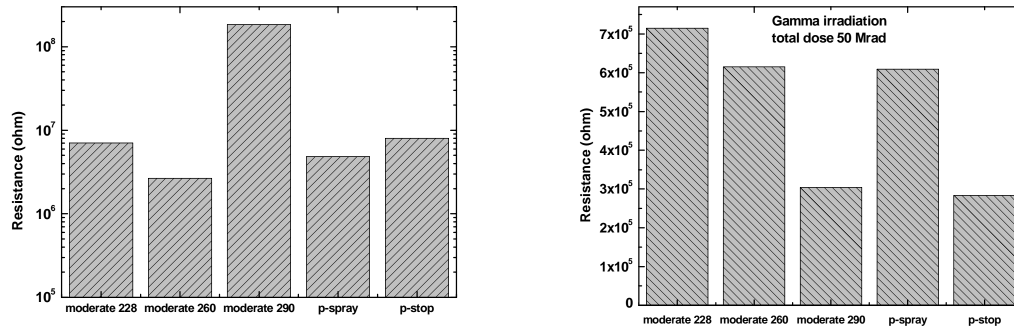

Fig.8-13. Interstrip resistance of test structures: non-irradiated (left) and irradiated (right).

In order to prove the effectiveness of the three isolation technologies, the test structures were irradiated with gamma rays from a ^{60}Co source to a total silicon absorbed dose of 50 Mrad (500 kGy), which is an estimation of the total dose expected in the middle region of the future upgrade of the Atlas detector at Super-LHC [17]. The fast build-up of damage in the oxide layer reaches a saturation value of about 2-3×10^{12} cm-2 at about 100-200 krad (few LHC weeks). Therefore, the oxide charge will be saturated well before the bulk damage will start to affect the operation of the detectors. This oxide charge increases the inversion layer, canceling the effect of insulation and thus shorting the strips. The interstrip resistance for the different technologies is on the order of Mohm also after irradiation. This value is enough to insure a good isolation between the strips since the polisilicon bias resistor has a resistance on the order of Mohm in standard strip detectors. This resistance is in parallel with the resistance between the strips and therefore the read out electronic will see the smaller of the two. Figure 8-13 also shows that the moderate p-spray with the smaller oxide thickness (and therefore with the highest profile in the p-spray are) has the highest resistance while the one with the thicker oxide has the smallest, comparable with the structure isolated only by the p-stop implant.

8.4 Upgrade of laser test systems (Prague)

Systematic analysis of three basic testing methods: test beam, beta tests and laser test was done and presented at the RESMDD06 conference. Applicability limits and systematic errors of the methods were evaluated [18]

One of the drawbacks of the laser measurement is lack of absolute collected charge determination. To overcome this problem a dedicated optical head was designed and produced (see schematics and photo in Fig. 8-14). It enables online monitoring of incoming and reflected laser pulse and further correction of DUT measurement. From the first tests linearity of response and very good sensitivity for low signals (~4 fC) was found (see Fig.8-15).

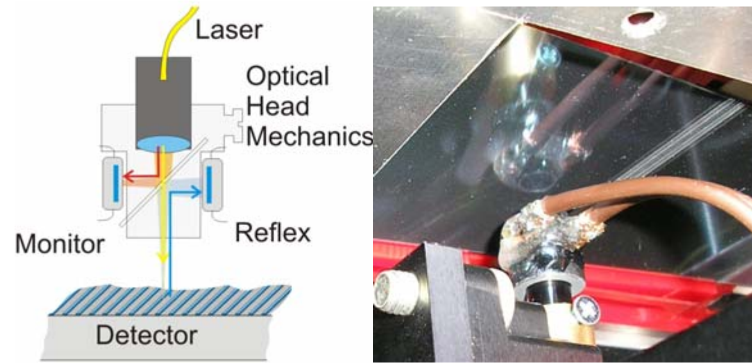

Fig 8-14: Schematics and photo of the optical head.

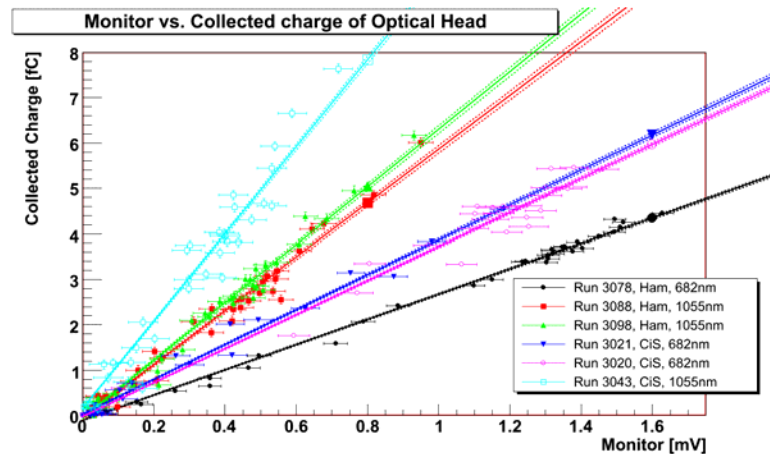

Fig. 8-15: DUT response vs. laser intensity monitor from the optical head for various detectors and wavelengths

The evaluation of newly developed detectors for LHC upgrade lacks electronics capable of measuring negative charge pulses from p-type detectors at the LHC timing. The ABC-next planned for ATLAS upgrade will not be available soon. Therefore existing and widely available SCT readout electronics based on ABCD3T chips was modified for negative charge and is now available for such measurements [19].

8.5 Progress in the development of the gaseous pixel detectors

Although the work on gaseous detectors is out of the main focus of the RD50 collaboration, a close link to these developments is kept to understand the recent developments in non-solid state tracking detector developments. The RD50 – Nikhef group is deeply involved in the gas detector developments and has reported on recent developments of the Gossip detectors.

In the gaseous pixel detector Gossip a pixel chip is equipped with the gas amplification grid Micromegas and a 1 mm thick drift volume. In this way a gas ionization detector is created with a comparable geometry as planar solid state pixel detectors. Most striking advantages of Gossip are the expected excellent radiation tolerance exceeding 10^{16} n_{eq}/cm^2 and a big reduction of the material budget of the cooling circuit.

After a successful production of the preamp/discriminator chip Gossipo1 featuring 40 ns shaping time, 60 electrons noise and 2 μW electrical power in 130 nm technology, the Gossipo2 chip was submitted in November containing a 16 x 16 cell pixel detector at 55 x 55 μm pitch. In addition each cell is also equipped with electronics for drift time measurement.

The production of the amplification grid InGrid that is made by wafer postprocessing, has been evolved to a reliable small scale industrial process. Also prototypes have been made accumulating double and triple grid layers.

The charge amplitude spectrum has been measured using β rays from a strontium source. From the spectrum the cluster density of several gases and gas mixtures was calculated. For di-methyl-ether a much lower value was found than was known from literature.

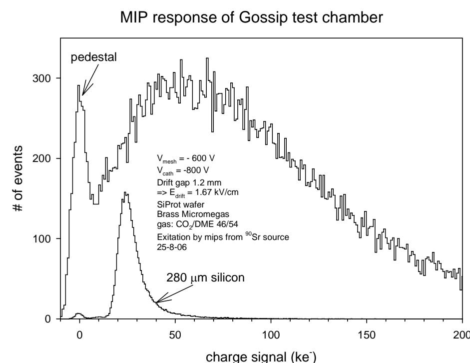

Fig. 8-16: Charge amplitude spectrum of Gossip. As a reference the spectrum from a planar silicon sensor (ATLAS SCT baby sensor) is plotted as well.

8.6 References in Chapter 8

[1] LHCb Vertex Locator: Technical Design Report, CERN-LHCC-2001-011

[2] ATLAS Inner Detector Technical Design Report, CERN/LHCC/97-16 and CERN/LHCC/97-17, 1997.

[3] CMS TDR, 1998, CERN/LHCC 98-6 CMS TDR.

[4] G. Casse et al. , *Nucl. Inst and Meth. A,* vol 518, pp.340-342, 2004

[5] S. Martì i Garcia et al., Nucl. Instr. and Methods. A473 (2001) p128-135

[6] G. Kramberger et al., Nucl. Instr. and Methods AVolume 481, Issues 1-3 , 1 April 2002, Pages 297-305

[7] M.Bruzzi, et al., Nucl. Instr. and Meth. A 541 (2005) 189-201.

[8] M. Miñano et al., Non-inverting detectors for Super-LHC, presented at the 6th International Conference on Radiation Effects on Semiconductor Materials, Detectors and Devices, Florence, Italy, October 10- 13, 2006.

[9] M. Lozano (CNM-Barcelona) – Private communication.

[10] Messineo et al., "Development of radiation hard silicon detectors: the SMART project", presented at the 9th ICATPP Conference, submitted for publication on Nucl. Instr. and Meth. A.

[11] H. F.-W. Sadrozinski et al., Total Dose Dependence of Oxide Charge, Interstrip Capacitance and Breakdown Behavior of sLHC Prototype Silicon Strip Detectors and Test Structures of the SMART Collaboration

[12] C. Piemonte, IEEE Trans. Nucl. Sci., vol. 53, no. 3, pp. 1694-1705, June 2006.

[13] A. Scarpa et al, Solid-Stae Electronics Vol. 41, no 7, pp 935-938, 1997.

[14] G. Pellegrini et al. "Technology development of p-type microstrip detectors with radiation hard p-spray isolation", Nucl. Instr. and Meth A Volume 566, Issue 2 , 15 October 2006, Pages 360-365.

[15] C. Fleta et al., "P-spray implant optimization for the fabrication of n-in-p microstrip detectors", submitted for publication in Nuclear Instruments and Methods A 2006.

[16] J. Kemmer et al., "Strip Detector", United States Patent No. US 6,184,562 B1, Feb 2001.

[17] G. Darbo, et al. "Outline of R&D activities for Atlas at an upgraded LHC", CERN document COM-GEN-2005-002, Jan. 2005.

[18] Bazant et al.: Performance tests of semiconductor detectors, talk at the RESMDD06 Florence, submitted to NIM

[19] Kodys et al.: Negative charge readout with SCT electronics, http://www-ucjf.troja.mff.cuni.cz/kodys/works/laser_test/ATLASHyb_NegativeChargeMeasurement/index.html

9 Resources

All participating institutes organize their own resources required for the research activities in their home laboratories. Integration in a CERN approved R&D project allows them to apply for national funding in terms of financial and manpower resources. The collaboration comprises several institutes, which have access to irradiation sources (reactors and accelerators, see [1]), as well as clean room and sensor processing facilities. A very wide range of highly specialized equipment for characterization of sensors and materials is also available (see [2]).

9.1 Common Fund

RD50 has a Common Fund to which each institute contributes every year a certain amount. The Common Fund is used for project related investments, like processing of common test structures or purchasing of special material and equipment. Furthermore it is used to cover the organization of collaboration workshops, common irradiation runs, or other specific activities of common interest.

9.2 Lab space at CERN

The RD50 collaboration was temporarily using existing infrastructure and equipment at CERN in 2006 and requests to continue to do so in 2007. As a member of the collaboration, the section PH-DT2/SD can provide access to available lab space in building 14 (characterization of irradiated detectors), in building 28 (lab space for general work) and in the PH Departmental Silicon Facility (hall 186, clean space). The collaboration would like to keep the RD50 visitor office in barrack 591 and use the CERN infrastructure to organize one workshop at CERN in 2007.

9.3 Technical support at CERN

A low level of support from PH-DT2/SD (wire bonding and sensor mounting) may be profitable. The expected work volume for 2007 is estimated to be very limited.

[1] An extensive list of irradiation facilities open to RD50 can be found on the RD50 web page: http://www.cern.ch/rd50/
[2] R&D Proposal - DEVELOPMENT OF RADIATION HARD SEMICONDUCTORDEVICES FOR VERY HIGH LUMINOSITY COLLIDERS, LHCC 2002-003 / P6, 15.2.2002.